Chapter 5

Theory

This chapter details the theory relevant to the data analysis techniques described in Chapter 6 and the results presented in Chapter 7. Firstly, the fundamental operation of an atmospheric radar system is described. This explanation covers the scattering mechanisms responsible for signal returns in atmospheric radar systems as well as the transmission and reception theory that enables information to be extracted from these echoes. Secondly, the fundamental physical theory of meteor phenomena is then briefly outlined and specific background to their observation using radio waves is detailed. Various techniques to extract common meteoric parameters from radar data are then discussed with a view to application to the data collected.

5.1 Fundamental radar theory

The targets and scattering mechanisms that reflect radiation vary depending on the particular application of the radar system. For instance radar systems may be optimised as surveillance radars (land vehicles, ships, aircraft etc.), terrestrial environment radars (atmospheric studies, terrain-mapping, ocean waves) or extra-terrestrial radars (planetary, satellite, asteroids). Within these classes of radar differing scattering mechanisms are often responsible for the radar echo that is later analysed. The radar scattering mechanisms that provide targets for atmospheric, MST or similar radars are

outlined in the following section. In order to interpret these echoes it is necessary to derive some fundamental parameters from them. The fundamental transmission and reception techniques of an atmospheric sensing radar system are also described.

5.1.1 Radar scattering mechanisms

While the process of directing electromagnetic radiation toward a target and receiving a portion of the scattered energy is straightforward, the actual level of received radiation is largely dependent on the wavelength of the radiation and the scattering properties of the target. This results in the radar equation assuming a disparate form to accurately describe individual targets [*Sato*, 1989]. One primary consequence of this is that the level of the returned signal strength varies with distinct targets.

Radar systems are generally purpose built to illuminate a particular target or emphasise a scattering mechanism. As such they operate at a specific frequency or over a limited frequency range (e.g. within bands of the electromagnetic (EM) spectrum, see Appendix I) and direct this radiation into a specific environment or region of interest (e.g. upper atmosphere, land or sea surface). The radars used for study of the atmospheric region from near surface level to the upper atmosphere include MST, ST, over-the-horizon (OTH), ionosonde and incoherent scatter radar (ISR) types and encompass a wide range of frequencies of operation.

The propagation of both radio and light waves through the atmosphere is strongly influenced by its refractivity structure (laminar and turbulent) [*Gage & Balsley*, 1978]. This refractivity structure is exploited as a target in many atmospheric radars. Specifically, some atmospheric radars probe the optically clear neutral atmosphere and ionosphere and are optimised to scatter radiation from irregularities in the radio refractive index [*Gage & Balsley*, 1978]. Aside from radiation reflected by this structure in the propagation medium it is often returned by more traditional distinct targets such as meteors, hydrometeors, sea-surface or aircraft for instance. In the following section we will focus on and discuss the scattering mechanisms involved in the medium.

The occurrence of echoes from the clear atmosphere requires structure in the

medium at the scale of half the wavelength of the probing wave [*Gage*, 1983]. The structure and scattering property of the atmospheric medium is determined in its simplest form by the refractive index n

$$n = \frac{c}{v} \tag{5.1}$$

where c is the speed of light in free space and v is the velocity of the radio-wave in air. In general all atmospheric radar echoes arise from the $\lambda/2$ selected variations in the background refractive index (n). This background atmospheric refractive index for HF to UHF bands is given as [*Gage & Balsley*, 1980];

$$n - 1 = \frac{3.73 \times 10^{-1} e}{T^2} + \frac{7.76 \times 10^{-5} P}{T} - \frac{N_e}{2N_c} \tag{5.2}$$

where P (mb) is the atmospheric pressure, e is the partial pressure of water vapour, T (°K) is the absolute temperature, N_e (m^{-3}) is the number density of electrons and N_c (m^{-3}) is the critical plasma density. The three terms on the right hand side of the equation represent the contributions to the refractive index by water vapour, dry air and the presence of free electrons respectively [*Sato*, 1989]. The influence of each term on the refractive index varies as altitude increases and this is illustrated in Figure 5.1

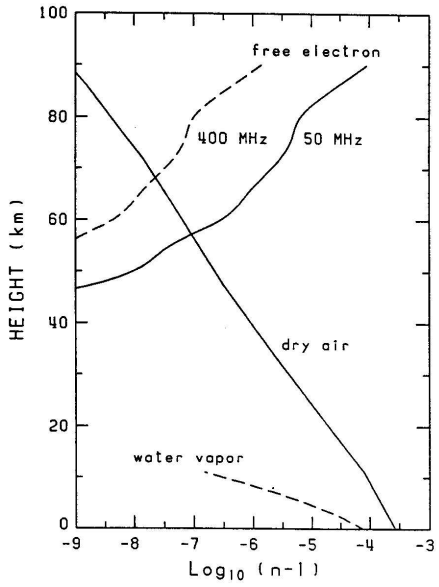

Figure 5.1: Typical height profiles of water-vapour, dry air and free-electron contributions to the radio refractive index (from *Sato* [1989]).

Four main mechanisms have been identified as being responsible for echoes detected by atmospheric or MST radars and they are **Bragg scatter**, **Fresnel (partial) reflection**, **Fresnel scatter** and **Thermal scatter**. Features of the first three mechanisms are distilled in the Table 5.1 and all are discussed in the following paragraphs.

Mechanism	Angular Spectrum	Coherence Time	Reflectivity Structure
BRAGG SCATTER			random turbulence
(a) isotropic	constant	short	(a) isotropic
(b) anisotropic	wide	short	(b) anisotropic
FRESNEL(partial) REFLECTION			one dominating lamina in stable environment
(a) specular	narrow	long	(a) very smooth
(b) diffuse	very narrow	very long	(b) corrugated (rough)
FRESNEL SCATTER			multiple laminae in stable environment
(a) stratified	narrow	intermediate	(a) horizontally stratified
(b) spread	wide	intermediate	(b) range, angle spread

Table 5.1: Scatter and reflection mechanisms of MST radar signals (from *Röttger* [1989*b*]).

The **Bragg scattering** mechanism has also been termed turbulent scatter or Pekeris scatter by various authors. Essentially, spatial variations in the refractive index occur as a consequence of a turbulent process and the resulting radar backscatter arises from the selection of components with scales of the order of half the radar wavelength in the direction of propagation [*Lesicar & Hocking*, 1992]. This type of scatter can exhibit isotropic or anisotropic properties depending on the generating source of the turbulence. *Röttger* [1989*b*] points out that if the turbulent irregularities of refractive index are homogeneously random and statistically similar in all directions (e.g. correlation distance is similar), then isotropic Bragg scatter results exhibiting no aspect sensitivity. Alternatively, anisotropic Bragg scatter (and thus aspect sensitivity) will result if the statistical properties are dependent on direction. The temporal variations of this form of scatter will be similar for either the isotropic or anisotropic case due to the random fluctuations source generating them.

A second type of scattering mechanism encountered is that of **Fresnel or partial reflection**. The term Fresnel reflection is appropriate because of the horizontal spatial scale from which the scattering is generated, while the term *partial reflection* is an indication of the weak scattering by this mechanism [*Röttger*, 1989*b*] as compared to the process of *total reflection* that typically occurs at higher altitudes [*Gage & Balsley*, 1980]. Fresnel reflection results from a *single* refractive index irregularity or discontinuity in the radar range gate. This type of scattering typically occurs in horizontally stratified and stable regions of the atmosphere [*Gage & Balsley*, 1980; *Lesicar & Hocking*, 1992]. As stipulated by *Reid* [1990], Fresnel reflection occurs strictly at vertical incidence from an irregularity with horizontal extent greater than one Fresnel zone as given by $(\lambda z)^{1/2}$, where λ is wavelength and z the height of the irregularity, and further that the vertical extent of the irregularity must be less than $\lambda/4$. However, he goes on to state that the minimum horizontal extent need only be greater than that of the radar beam.

Variations such as layer roughness, horizontal extent, multiplicity and tilting have been noted in the scattering layer [*Gage & Balsley*, 1980]. In terms of the degree of layer roughness, *specular* reflection is said to have resulted from an essentially smooth layer or refractive index discontinuity of this type and this term often is used interchangeably with Fresnel or partial reflection. An alternative to this type of scattering mechanism is the *diffuse* case where the discontinuity exhibits notable surface roughness or corrugations compared to the probing wavelength [*Gage*, 1983]. A possible source of this rough or corrugated layer has been attributed to the action of internal gravity waves on the initially smooth irregularity (e.g. *Vincent* [1972]; *Hocking* [1989]). Generally, both types of Fresnel reflection have notable aspect sensitivity [*Röttger*, 1989*b*] and exhibit long coherence times[1] primarily due to the stability of the region in which the refractive discontinuity exists.

Fresnel scattering is said to occur when a number of distinct refractive index irregularities exist in the one radar range gate. More specifically it arises when the

[1] i.e. the time-scale over which there is a negligible phase change.

scattering medium is coherent in the two dimensions transverse to the probing wave and random in the dimension parallel to the wave direction [*Gage & Balsley*, 1980; *Reid*, 1990]. This transverse coherence can extend from a few wavelengths to well over a Fresnel zone [*Gage & Balsley*, 1980]. This type of scattering mechanism has much in common with Fresnel reflection and can be thought of as the incoherent sum of partial reflections from many thin layers [*Gage*, 1983] of slightly differing refractive indices [*Hocking*, 1989]. Again, stability in the regions where the irregularities develop can contribute to their enduring presence. This type of scattering mechanism displays aspect sensitive characteristics, although because the discontinuities are statistically independent the temporal characteristics are said to be similar to those of Bragg scatter [*Röttger*, 1989*b*]. It is apparent that the size of the range gate has an effect on whether Fresnel scatter of Fresnel reflection is viewed by a radar; a coarse height resolution implies that Fresnel scatter is most likely to be observed [*Röttger*, 1989*b*].

The three forms of scattering discussed above are summarised in Figure 5.2.

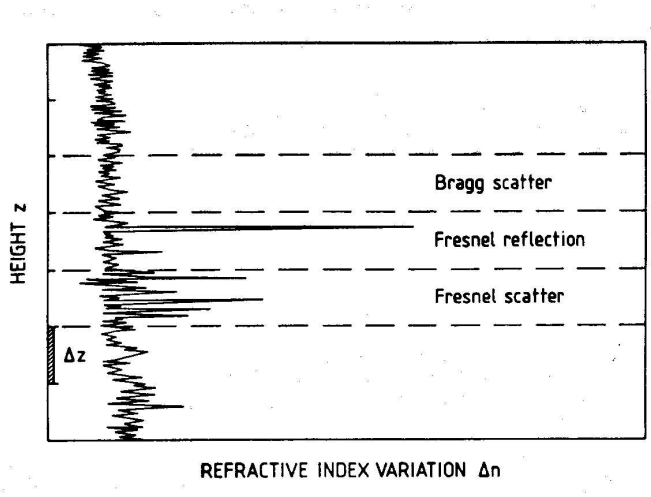

Figure 5.2: Illustrates possible scattering and reflection mechanisms responsible for radar echo. The spatial variations (Δn) of the refractive index (n) with height (z) is displayed. The different processes of Bragg scatter, Fresnel (partial) reflection and Fresnel scatter will result depending on the structure present in range gate Δz (from *Röttger* [1989*b*]).

Another form of scattering mechanism is that of Thomson or **Thermal scatter**. As indicated by Figure 5.1, the contribution to the refractive index by free electrons increases at higher altitudes and becomes dominant above 60 km. In this region the

statistical fluctuations in the electron density (and hence refractive index) caused by the random thermal motions of the electrons and ions can be sufficiently significant to cause scattering of the incident radiation [*Evans*, 1969; *Mathews*, 1986]. Since the scattering from individual electrons is random in phase, they will add *incoherently*, and the term *incoherent scatter* is also often ascribed to this form of scattering mechanism. The returned power depends on the number of electrons illuminated by the radar beam. To achieve an adequate signal-to-noise ratio requires high transmitter powers, typically exceeding 2 MW [*Evans*, 1969]. Because the required transmitter powers are well above those used in the current MF radar, incoherent scatter does not contribute to the results presented in this work.

As mentioned in section 1.1 and illustrated in Figure 1.1 on page 4, the upper atmosphere consists of ionospheric layers which can also greatly influence radio wave propagation. The important factor here is the value of the radar frequency in relation to the critical frequency of the ionospheric plasma defined by

$$f_{crit} = \sqrt{80.6\, N_{max}} \tag{5.3}$$

where f_{crit} is the critical frequency (Hz) and N_{max} is the peak electron density of the layer (electrons/m^3) [*Rishbeth & Garriott*, 1969; *Richmond*, 1987]. A vertically transmitted radio wave will be reflected or refracted from a layer if it is below the critical frequency defined by this relation. From Figure 1.1, typical day and night time peak electron densities of the E-region are 1.25×10^{11} and 1.0×10^{9} e/m^3 and thus give a critical frequency of 4.5 and 0.3 MHz respectively. This result clearly indicates why radar meteor data at a transmitted frequency of 2 MHz from meteors occuring at E-region heights is only possible during night time.

5.1.1.1 Electromagnetic scatter from meteor trails

While scattering from individual electrons is random in phase, if the electrons are aligned in space the scattering can be strongly *coherent* [*Sato*, 1989] and it is the highly linear column of ions and electrons generated by an ablating meteor that allows

a significant *specular* radar echo to be detected using relatively low power atmospheric or MST type radars. Thus the scattering mechanism for meteors exhibits similarities to Fresnel reflection but is particularly influenced by the spatial density of electrons, to the point where some meteor trail scattering mechanisms (e.g. the later mentioned overdense case) can be described as having originated from a small scale ionosphere type structure [*McKinley*, 1961; *Thomas, Whitham & Elford*, 1988].

The electromagnetic scattering from meteor trails has been surveyed in concert with other areas of meteor physics by a number of workers (see e.g. *Eshleman* [1960]; *McKinley* [1961]; *Ceplecha et al.* [1998]). A meteoroid impinging on the atmosphere ablates and initially produces a highly linear and narrow column of partly ionised ablation products, due in large part to the high initial speed at which the meteoroid traverses the atmosphere. From simultaneous multi-frequency radar studies it has been deduced that the trail has an initial radius (r_0) in metres given by

$$\log_{10} r_0 = 0.019\, h - 1.92 + \log_{10}(V/40) \tag{5.4}$$

where V is meteor velocity (km s^{-1}) and h is altitude (km) [*Baggaley*, 1980; *Baggaley*, 1981; *Thomas, Whitham & Elford*, 1988]. For a meteoroid of velocity 40 km s^{-1}, the initial trail radius is 0.4 m at 80 km altitude and 2.3 m at 120 km. These initial trail radii are much less than the wavelength of a probing MF radio wave and thus facilitate the trail's detection by such radars. However, VHF meteor radars have an instrumental height ceiling typically of 110 km (see *McKinley* [1961]). The height ceiling effect is further discussed at the end of this section.

This initial trail is formed almost instantaneously because the ablated meteor atoms, upon colliding with the local air molecules, retain much of their initial speed and for meteoroid speeds >10 km s^{-1} the energies involved in the collision process are significantly in excess of the ionisation potentials of most metal atoms in stony meteoroids, so as many as ten collisons are required to slow the atoms down to thermal velocities, though less than a millisecond is needed to complete the process [*McKinley*, 1961; *Jones*, 1997].

In terms of the ionisation produced, the mass of the positive ions preclude them from oscillating significantly in the presence of the transmitted radiation of the radar and it is the behaviour of the electrons that determines the signal detected by radio means. Following this, a primary characteristic of a trail in terms of scattering is the trail's line density (the total number of electrons per metre of length along the trail), as opposed to the volume density (the number of electrons per cubic metre) [*Eshleman*, 1960]. From this viewpoint, two scattering regimes for a meteor echo are usually delineated, the underdense and overdense trail. The *underdense* case occurs when radio scattering from trail line densities of $<10^{13}$ electrons per metre, while the *overdense* case is applicable when densities exceed $\sim 10^{15}$ electrons per metre. It should be noted that the transition between the two trail types is not sharply defined [*McKinley*, 1961].

In physical terms, the lower spatial density of electrons in the *underdense* case allows the incident radiation to penetrate the trail and each free electron acts as an independent scatterer. Secondary radiative effects are negligible and absorptive effects can be neglected. The signal received is the sum of individual scattered electric fields and has a strong coherence because the linearity of the trail and the initial radius of the trail being $<< \lambda$. Such trails are highly aspect sensitive. In general, the scattered signal can be considered as coming from a region of the trail of the order of one Fresnel zone about the specular point on the trail.

In contrast to the underdense case, if a meteoroid leaves a column of ionisation with a line density greater than $\sim 10^{15}$ electrons per metre secondary scattering between electrons becomes significant and the incident wave becomes evanescent within the electron column. This situation is often described as similar to the reflection from the surface within which the dielectric constant is negative and this can be approximated as a metallic cylinder [*Greenhow*, 1952; *Poulter & Baggaley*, 1978; *Ceplecha et al.*, 1998]. After the formation of the overdense trail, diffusion effects first cause the critical radius of the effective scattering cylinder to increase until the dielectric constant of the region reaches zero when the critical radius collapses to the axis and individual

electron scattering occurs as the transmitted wave now penetrates the column, i.e. the trail becomes underdense [*Poulter & Baggaley*, 1978].

While the two meteor scattering regimes described above account for a large majority of radar observable echoes, a third scatter mechanism has long been identified as responsible for some echoes which appear to come from a cloud of ionisation at the head of the meteor train. These are often recorded by high power radars with broad beam antennas [*Jones et al.*, 1988; *Thomas & Netherway*, 1989], but have also been observed by lower-powered narrow-beam systems [*Taylor, Cervera, Elford & Steel*, 1996]. The term *head echo* is conveniently used to describe this phenomenon. These echoes have been discussed by many authors in the last forty years. Following recent simultaneous multi-frequency observations of such echoes using the narrow beam ARPA Long-range Tracking And Instrumentation Radar (ALTAIR) radar and other radars on Kwajalein Atoll it is now generally accepted that these echoes are from overdense ionisation surrounding a meteoroid at the head of a trail. A rough physical picture is a reflecting hemisphere of radius comparable to the initial radius discussed earlier; the scattering is essentially isotropic. Similar types of echoes are also observed with the high power, very narrow beam Arecibo radar, but the question of whether these echoes can also be explained by the "overdense head" model is currently an area of debate [*Elford*, 2003*c*, private communication].

In the case of underdense and overdense meteor events, the trails typically extend over a height range of 10 to 15 km [*Thomas, Whitham & Elford*, 1988] and a condition for the detection of such trails is that an orthogonal from the radar site to the meteoroid path should intersect the trail. As mentioned above the echo typically originates via the specular reflection from a region of the trail of the order of one Fresnel zone about this orthogonal or t_0 point [*Taylor & Elford*, 1998] (see Figure 5.6 on page 250). The Fresnel zone length is given as $\sqrt{2\lambda R_0}$ where λ is the radio wavelength and R_0 is the slant range. For a trail at a slant range of 100 km detected via a 2 MHz radar this Fresnel zone length is 5.47 km. For VHF radars the central Fresnel zone is ~ 1 km.

After the formative stages of the trail have ended, the trail is increasingly influenced

by the established processes in its surrounding environment. Dominating the trail behaviour in the few seconds after initial trail formation is the ambipolar diffusion process, whose action reduces the amplitude and duration of the echo. Wind shears, recombination and attachment are also experienced. In particular the action of the local wind may produce secondary reflection regions along the trail that better adhere to the specular reflection condition necessary for detection than is obtained during the formative stages of a trail [*Jones et al.*, 1988]. Turbulence dominates those trails lasting more than thirty seconds [*Thomas, Whitham & Elford*, 1988].

As touched upon previously, most radars used for meteor trail detection are subject to a height ceiling effect [*McKinley*, 1961]. This effect limits a radars ability to detect trails above a certain height based primarily on a radar's probing wavelength as well the trail radius, meteoroid velocity and local atmospheric diffusion. In physical terms this height detection limit arises when the width of underdense trail approaches an order of the radio wavelength such that the backscattered radiation from an electron in the near and far parts of the train destructively interfere due to the difference in phase [*Olsson-Steel & Elford*, 1987]. In this situation the echo is severely attenuated. Also serving to attenuate the echo power received is the trail radius, as given by Equation 5.4. This initial radius increases with increasing height and meteoroid velocity leading to echo attenuation as it approaches the applied radio wavelength. Similarly, after trail formation the trail diffuses in accordance with the local atmospheric conditions and trail radii can quickly attain sizes comparable to radar wavelength. At MF this echo ceiling height is above 140 km [*Olsson-Steel & Elford*, 1987] which facilitates a more complete observation of the total meteoroid flux.

5.1.2 Radar transmission and reception theory

While the basic intensity of a received signal from a specific target is obtained from the formulation of a radar equation, which is discussed in later sections for the case of a meteor target, other important radar parameters must be also be determined such as range, etc. Techniques to obtain these parameters vary for the different type of radar

systems (see e.g. *Skolnik* [1970]). Atmospheric radars mostly use a pulsed operation where electromagnetic radiation is broadcast as short duration pulses in the direction of a target and the resulting scatter is received.

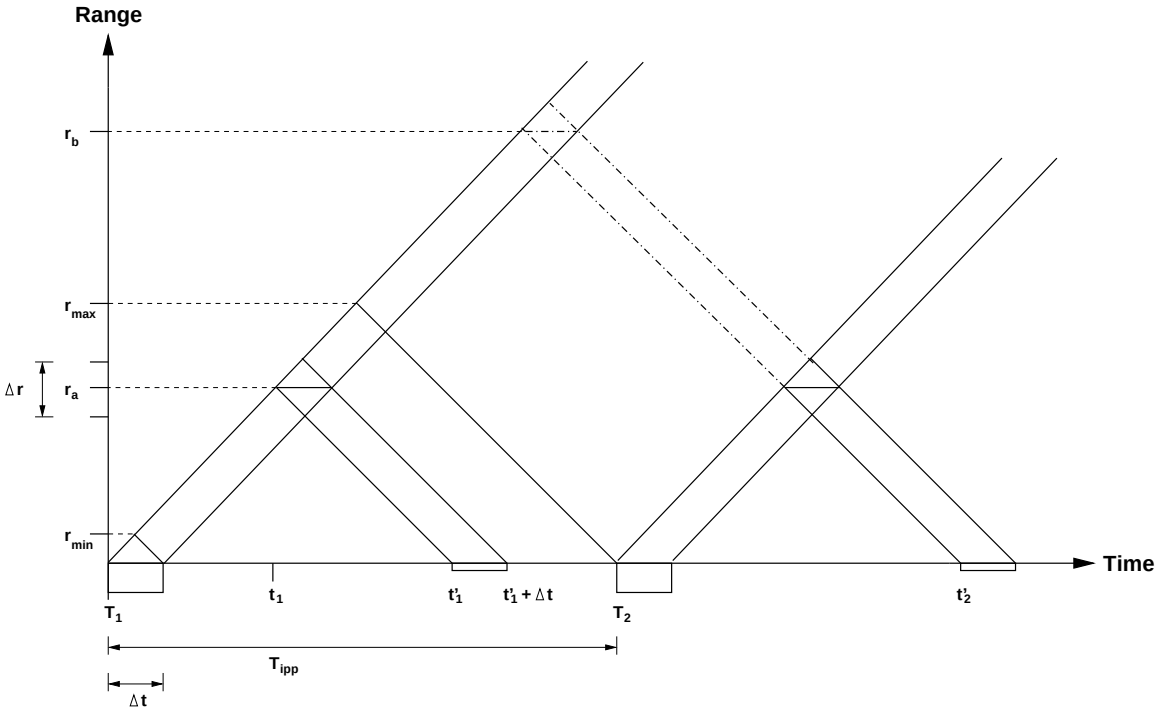

Figure 5.3: Range-time diagram describing fundamental pulsed radar operation for a volume target (adapted from *Röttger* [1989*a*]).

Fundamental radar relations such as those described in the following paragraphs are well documented (e.g. *Skolnik* [1970]; *Barton* [1976]; *Hovanessian* [1988]; *Röttger* [1989*a*]; *Sato* [1989]; *Tsuda* [1989]). Figure 5.3 summarises the operation of a pulsed radar. If an electromagnetic pulse of rectangular shape and duration Δt is transmitted at time T_1, it will propagate in a non-dispersive medium at the speed of light c toward the desired target. If a target that reflects electromagnetic radiation is positioned at a range r_a from the radar, the time taken to this position is $t_1 = r_a/c$. Some portion of this transmitted energy is reflected back toward the transmitter and is received at a time $t'_1 = 2t_1 = 2r_a/c$. Thus the *range* of any target is determined by the round trip time via the basic radar relation

$$r = ct/2 \tag{5.5}$$

This would be the case for a pulse directed toward a point-like target or the leading edge of a pulse when directed at an extended target such as a thin reflecting layer. If we consider the target as the latter and as such possessing some significant horizontal extent and noting that the transmitted pulse has a finite duration, the trailing edge of the pulse will be detected by the receiver at a time $2t_1 + \Delta t = t_1' + \Delta t$.

Alternatively, as is often the case in atmospheric radar sensing, many scatterers may be present. Assuming there are scatterers at immediately adjacent ranges above and below $(r_a \pm \Delta r/2)$ (i.e. a target with significant vertical extent), these will contribute to the reception of echoes. Thus the echoes from the ranges between $r_a - \Delta r/2$ and r_a are detected at the receiver simultaneously at t_1'. Similarly, echoes from $r_a + \Delta r/2$ are received at $t_1' + \Delta t$. From this it can be seen that a finite duration pulse illuminates a volume at range r_a extending over a range $\Delta r = c\Delta t/2$, where Δr is termed the *range resolution*. This situation results in the range weighting function of the single range gate at r_a being a triangle as most power is returned from r_a, with less significant components returned from $r_a \pm \Delta r/2$.

This illustrates the fact that the nominal range resolution of a radar (Δr) is determined by the transmitted pulse width (Δt) providing the receiver bandwidth is matched to this pulse width. This range resolution can be interpreted as the distance beyond which two reflectors must be separated so that their echoes are seen as distinct [*Lewis et al.*, 1986][2]. An effective sampling regime of the echo may be achieved by sampling the received signal at an interval of $\sim\Delta t$. A sampling of less than Δt produces overlapping regions between the samples (oversampling), while a sparse sampling (undersampling) results in missing regions [*Sato*, 1989].

In most radar applications the pulse width has the greatest bearing on the minimum detection distance r_{min}. Effectively, the time to launch a pulse obscures the equivalent distance immediately adjacent to the radar. In actuality this minimum range is further affected by the transmit/receive hardware's response times (e.g. *Röttger* [1989*a*]).

[2]Range resolution is equivalent to the term *discrimination* used in the time domain reflectometry technique of Chapter 3.

As defined in the Figure 5.3, the interpulse period (T_{ipp}) specifies the period between consecutively transmitted pulses. The pulse repetition frequency (PRF) is defined as $f_{prf} = 1/T_{ipp}$ and most atmospheric radars operate with a given fixed PRF [*Tsuda*, 1989]. The pulse repetition frequency also establishes the maximum unambiguous range (r_{max}) of the radar. As mentioned, pulsed radars rely on interpreting the immediate return from a transmitted pulse to establish range. Ideally, this assumes that the period immediately following the transmitted pulse and before the next subsequent transmitted pulse is the only time period available for the reception of echoes. And from the diagram it can be seen that the maximum range $r_{max} = c/2f_{prf} = cT_{ipp}/2$. However, as is also evident in the Figure 5.3, if a target exists at range r_b, echoes excited from the initial pulse (T_1) can be received over the period of the consecutive pulses (T_2, T_3, ...). So targets at ranges greater than R_{max} can produce echoes that return to the radar after one or more interpulse periods but appear to have ranges between R_{min} and R_{max} [*Lewis et al.*, 1986]. In effect the echo from r_b is *folded back* into the expected range region $r_{min} \leq r_b \leq r_{max}$, with its true range obscured. This situation is termed *range aliasing*. To limit this situation the interpulse period is increased to encompass the echo received from the target with the largest expected range (r_b).

This determination of maximum unambiguous range assumes that the radar is operated with unlimited power in an environment that allows unimpeded radiowave propagation and is free from noise. However it is these considerations that also have an affect on an individual radar's maximum range. In such an enviroment the effective maximum range is often more precisely determined by establishing the minimum echo power received from a distant target that can be discerned from noise (e.g. *Reintjes & Coate* [1952]).

In terms of the radar wavelength used in these studies and the environment probed (i.e. a multi-layered ionosphere) there is often the prospect of range aliasing, where echoes from ionospheric layers or other structure at heights in excess of 100 km are folded into lower ranges. These range aliased echoes are often characterisied by their

lower power and broader spectral distribution [*Tsuda*, 1989]. Range aliasing may be acceptable if there is other information that excludes the echo, for example, it is known that the physical characteristics of the target limit the maximum or minimum range.

In what follows the relevant radar scattering mechanisms and fundamental radar relations are applied to the case of a meteor trail and the theory specific to this situation is now discussed.

5.2 Fundamental theory of meteors

This section is divided into two parts; physical and radio meteor theory, and outlines the theory upon which later discussions are based. The first section has a brief review of the sources of radar observable meteors and then discusses the physical processes that occur as a meteoroid collides with the Earth's atmosphere. This is followed by a development of the radio theory describing a radar's interpretation of the meteor phenomenon.

5.2.1 Physical theory

Numerous reviews of meteor phenomena have been made (e.g. *Ceplecha et al.* [1998]; *Hughes* [1978]; *Kresák & Millman* [1968]; *Hawkins* [1964]; *McKinley* [1961]; *Öpik* [1958]; *Kaiser* [1955]) and some incorporate discussions of their observation by radar. The meteoroids that give rise to the trails detected by radar extend over a wide mass range depending on their atmospheric entry speed and height. It is the commonly observable radar meteors that we will concentrate our discussion on here.

5.2.1.1 Sources

The origins or sources of meteoroids deduced to the present time are constrained by the fact that the Earth's trajectory in its orbit must intersect with the meteoroids. The celestial distribution of sporadic sources have been well established [*Taylor & Elford*, 1998]. While the sporadic component dominates all meteors, the meteor showers

contribute short bursts of activity, occasionally quite intense as in the case of the Leonids in recent years.

Shower events, lasting from orders of hours to days or weeks, are the result of the atmosphere's intersection with a region of a meteoroid stream created by the sublimation and then ejection of particles from the nucleus of a cometary body during its passage near the Sun or more rarely, the ejection of particles from an asteroid or inner planet [*Hughes*, 1993] as a result of a (body-to-body) collision. The orbits of meteoroids in a stream are perturbed by various influences, particularly radiation pressure and the gravitational effects of planets. Thus meteor streams disperse as they age and this is reflected in the duration and intensity of the associated showers observed on the Earth. The geographic position of the observer also affects the meteor rate as the shower only displays its full activity when its radiant passes near the zenith [*Ceplecha et al.*, 1998].

A significantly greater influx of meteoroids occur as sporadic meteors. No specifc shower membership can be attributed to this component; however, one source is expected to be that of very dispersed minor showers [*Ceplecha et al.*, 1998][3]. More generally, studies of the sporadic meteor radiant distributions using numerous individual photographic or radar surveys [*Taylor & Elford*, 1998; *Jones & Brown*, 1993; *Jones & Brown*, 1994] have confirmed a six-source model, isolating the Helion (H), anti-Helion (AH), north toroidal (NT), south toroidial (ST), north apex (NA) and south apex (SA) source (see Figure 5.4). These researchers suggest possible formation mechanisms, although it remains unclear whether the origins are mostly asteroidal or cometary in addition to conjecture about the validity of the toroidal source. A small fraction of meteor events have been observed to originate from interstellar sources (e.g. *Taylor et al.* [1994]; *Taylor, Baggaley, & Steel* [1996]; *Baggaley* [2000] and *Baggaley & Galligan* [2001]).

The relative influx levels of these shower and sporadic sources has been defined by *Hughes* [1993] for the mass interval of 10^{-8} kg $< m < 10^{2}$ kg; *Hughes* states that

[3] *Hughes* [1978] discusses various mechanisms of meteor stream decay.

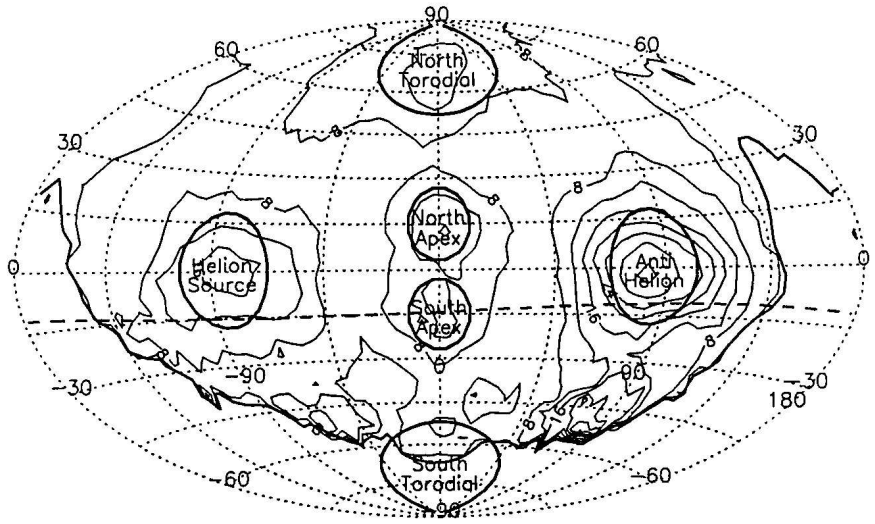

Figure 5.4: Radiant distribution of meteoroids with masses $>10^{-4}$ g encountering the Earth (from *Taylor & Elford* [1998]). The coordinate frame used here places the Earth's Apex at the centre, the solar (Helion) direction at a longitude of $-90°$ and the north ecliptic pole at $+90°$.

for every particle of planetary and satellite ejector, 4.4×10^9 asteroidal fragments and 4×10^{12} particles of cometary dust follow, indicating the dominance of cometary and asteroid sources.

5.2.1.2 Meteoroids in the atmosphere

In terms of the interaction with the atmosphere, there are four possible regimes experienced by a meteoroid. Whether all are experienced by an individual meteor event depends on its initial size and speed. They are pre-heating, ablation, dark flight and impact. For the size of particles contributing to radar meteor observations the impact regime can be neglected. As the meteoroid enters the upper atmosphere collisions with air molecules result[4]. This pre-heating interaction increases the surface temperature of the meteoroid over a period of seconds or less to a level (typically 1850 K) where ablation commences. Meteoroid ablation constitutes mass loss in any form and phase [*Ceplecha et al.*, 1998]. This encompasses loss as solids (fragments), fluids (droplets) or hot gases. Significant fragmentation of a meteoroid, where at least two distinct masses

[4]Note that if the angle to the horizontal is too shallow (i.e. $< 7°$) the meteoroid can skip off the atmosphere [*Love & Brownlee*, 1991].

result from a single ablating meteoroid, is a relatively commonly occuring but complex process (e.g. *Hawkes & Jones* [1975]; *Ceplecha et al.* [1993]). Typically, fragmentation occurs initially at the lower temperatures and proceeds through the processes of melting and then evaporation (at ∼2500 K). Due to its inherent complexity, fragmentation effects are neglected in most meteoroid studies, with meteoroids treated as single ablating bodies or at the most, multiple, identical bodies and this is the approach taken in this study. However, a recent radar fragmentation study [*Elford & Campbell*, 2001] offers the opportunity for this complex process to be more fully described.

These evaporated meteoroid atoms essentially retain the speed of the intact meteoroid and thus have considerable kinetic energy. This energy is utilised as the atoms collide with the surrounding air molecules, and atoms in excited and ionised states are produced. Light is emitted as the atoms in excited states return to their normal state. The luminous energy emitted per second I is given [*McKinley*, 1961; *Hawkins*, 1964];

$$I = -\tau \frac{V^2}{2} \frac{dm}{dt} \tag{5.6}$$

where τ is the luminous efficiency, m is the meteoroid mass and V is the velocity of the meteoroid. This can be further refined if the energy loss due to deceleration is also included [*Ceplecha et al.*, 1998].

The line density (q) or number of electrons produced per metre is [*McKinley*, 1961; *Hawkins*, 1964; *Ceplecha et al.*, 1998]

$$q = -\frac{\beta}{\mu V} \frac{dm}{dt} \tag{5.7}$$

where β is the ionising probability that one meteor atom will produce an electron-ion pair and μ is the average mass of an ablated meteoroid atom ($\mu = 40$ [*Love & Brownlee*, 1991]). The quantity β depends strongly on speed and can be found [*Ceplecha et al.*, 1998] from the relation

$$\beta = \begin{cases} 9.4 \times 10^{-6}(v-10)^2 v^{0.8} & \text{for} \quad V < 35 \quad \text{km s}^{-1} \quad \textit{Jones}\,[1997] \\ 3.02 \times 10^{-17} V^{3.42} & \text{for} \quad V > 35 \quad \text{km s}^{-1} \quad \textit{Bronshten}\,[1983] \end{cases}$$

where v and V is the speed in km s^{-1} and m s^{-1} respectively. *Jones* [1997] notes that for meteoroid speeds less than 35 km s^{-1} this result only applies to faint meteors. For

a meteor of speed 40 km s^{-1}, $\beta = 0.17$, which emphasises that only a small fraction of the interactions produces ionisation and that most of the meteoroid completes its journey as independent neutral atoms.

The commencement height of ablation as a function of meteoroid radius is displayed in Figure 5.5. Meteoroid ablation heights have been discussed previously by *Hughes* [1978] after the work of *Jones & Kaiser* [1966] and *Kaiser & Jones* [1968]. More recently, investigations of *Love & Brownlee* [1991] have been discussed by *Ceplecha et al.* [1998]. In this figure it is assumed that the meteoroid has a trajectory inclined at 45° to the vertical. Various entry velocities are displayed ranging from 11 to 70 km s^{-1}. For particles smaller than the micrometeoroid limit no ablation occurs while for masses larger than this, but smaller than the line given by $M = +15$, the onset of ablation is delayed due to thermal radiation. As the mass increases towards line $M = +10$, a further delay is due to the finite heat capacity of the meteoroid absorbing energy and at still larger masses the meteoroid develops a marked thermal gradient that can be sufficient to initiate particle fragmentation.

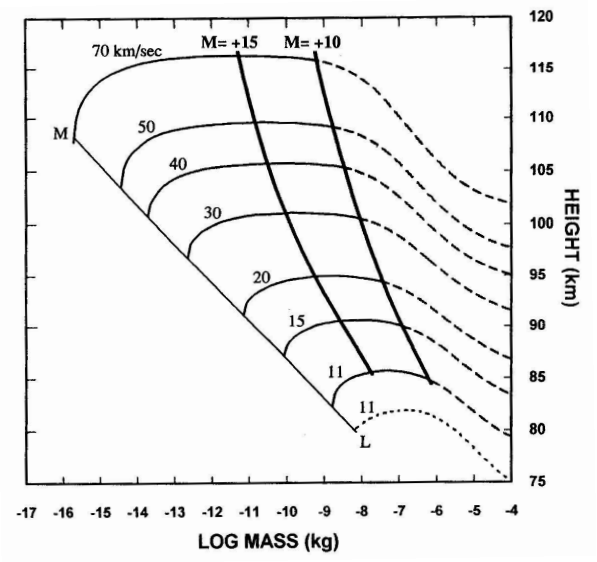

Figure 5.5: Theoretical commencement heights of ablation of a single stony particle entering the atmosphere (zenith angle = 45°) [*Ceplecha et al.*, 1998]. The thickened lines give the mass and velocity of particles that produce trails of maximum line density 10^{10} and 10^{12} electrons per metre (radio magnitudes $\sim +15$ and $+10$). The line ML is the micrometeoroid limit.

Whilst not relevant to the radar meteor observations to be considered later, it is of interest to note that when there is insufficient kinetic energy to maintain evaporation or maintain heating a meteoroid can enter the dark flight phase. The meteoroid is decelerated and rapid cooling of the body takes place with a vertical trajectory or free fall being entered into. The particle behaviour is subject to atmospheric winds and the increasing atmospheric pressure until the final impact regime occurs. For typical masses, if a meteoroid is travelling greater than 30 km s^{-1} mass loss from severe ablation will preclude a meteorite fall or micrometeorite dust deposition from occurring.

5.2.2 Radio theory

Fundamental meteor radio theory is discussed in many publications (e.g. *McKinley* [1961]; *Cervera* [1996]; *Ceplecha et al.* [1998]). The meteoroid entering the atmosphere will form a trail of ionisation that can be illuminated by a radar beam. Typically, this linear plasma of electrons and ions is defined by its line density and characteristic boundaries and gradients that allows a significant echo to be received by the radar.

A simplified trajectory of a meteor trail formed above a radar is shown in Figure 5.6. For the idealized underdense case, an expression for the expected backscattered power

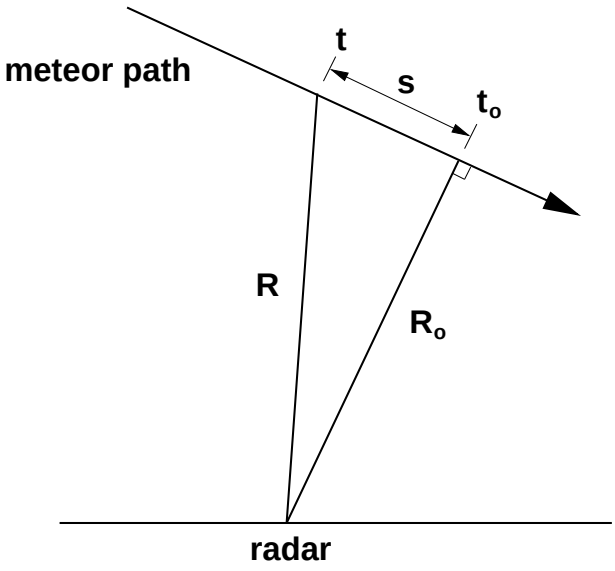

Figure 5.6: Meteor trail trajectory (after *McKinley* [1961]).

can be derived (e.g. *McKinley* [1961]; *Sato* [1989]; *Cervera* [1996]; *Ceplecha et al.* [1998]), as discussed below.

The estimate of back scattered power obtained from a meteor trail essentially comprises three terms relating to the incident radiation, target scattering cross-section and the reflected radiation. The power flux (Φ_i) of the incident wave at a point on the trail a distance R from the radio transmitter is

$$\Phi_i = \frac{P_T G_T}{4\pi R^2} \quad \text{watts m}^{-2} \tag{5.8}$$

where P_T is transmitted power and G_T is the antenna gain directed toward the trail element, relative to an isotropic radiator. The scattering cross section of a free electron is given as $\sigma_e = 4\pi r_e^2 \sin^2\gamma$, where r_e is the classical electron radius (2.817940×10^{-15}m) and γ is the scattering angle ($\gamma = \pi/2$ for backscatter case). Thus the flux of power at the receiving antenna due to a single electron is

$$\Phi_e = \frac{\Phi_i \sigma_e}{4\pi R^2} = \Phi_i (\frac{r_e}{R})^2 \tag{5.9}$$

The assumption that the effective diameter of the trail is less than the probing wavelength allows the trail to be viewed as having all electrons distributed along one line. For a line element ds, all electrons will thus scatter in phase. The electric field rather than the power fluxes are summed to find the resultant field at the receiving antenna by associating an electric field $\boldsymbol{E}_e$ with each power flux of an electron Φ_e. If Z_o is the wave impedance of free space, then the maximum possible amplitude of the field (E_o) returned from the trail segment is;

$$E_o = (2 Z_o \Phi_e)^{1/2} \tag{5.10}$$

An expression for the instantaneous amplitude of the field for trail element ds containing $q\,ds$ electrons is

$$E_{oi} = (2 Z_o \Phi_e)^{1/2} e^{i(\omega t - 2kR)} q\,ds \tag{5.11}$$

The exponential expression takes into account the location of the trail from the radar (distance 2R) and thus the phase delay ($2kR$ radians) of every field vector ($\boldsymbol{E}_e$) and

uses k=$2\pi/\ \lambda$. The amplitude signal from the complete trail at the receiving antenna is thus

$$E_R = (2Z_o\Phi_e)^{1/2} q \int_{-\infty}^{s} e^{i(\omega t - 2kR)}\ ds \tag{5.12}$$

and the electron line density of the trail is assumed to be constant. As *McKinley* [1961] states, this integral is difficult to evaluate in general and can be made more tractable by using the approximation $R \approx R_o + s^2/2R_o$, which is justified as the range R changes very slowly with time near the t_o point. Here, s is the distance along the trail from the orthogonal point to ds, giving

$$E_R = (2Z_o\Phi_e)^{1/2} q \int_{-\infty}^{s} e^{i(\omega t - 2kR_o - \frac{ks^2}{R_o})}\ ds \tag{5.13}$$

To simplify the phase factor the substitution $\frac{\pi x^2}{2} = \frac{ks^2}{R_o}$ is used. Thus E_R becomes

$$E_R = (\frac{R_o\lambda}{4})^{1/2} (2Z_o\Phi_e)^{1/2} e^{i(\omega t - 2kR_o)} q \int_{-\infty}^{x} e^{i(\frac{-\pi x^2}{2})}\ dx \tag{5.14}$$

The final term may be recast using alternate notation for the exponential to give

$$E_R = (\frac{R_o\lambda}{4})^{1/2} (2Z_o\Phi_e)^{1/2} e^{i(\omega t - 2kR_o)} q(C - iS) \tag{5.15}$$

where

$$C = \int_{-\infty}^{x} cos(\frac{\pi x^2}{2})\ dx \qquad \& \quad S = \int_{-\infty}^{x} sin(\frac{\pi x^2}{2})\ dx$$

are the Fresnel integrals of optical diffraction theory. The normalized variable x is often referred to as the Fresnel length [*Cervera*, 1996] or Fresnel parameter [*Baggaley et al.*, 1997]. *N. Herlofson* is credited by *Ellyett & Davies* [1948] with recognizing that as a meteor trail is formed within the beam of a radar the fluctuations in the echo amplitude are the radio analogue of the optical diffraction at a straight edge of a half-plane [*Elford*, 2001*a*]. If the functions C and S are plotted the familiar cornu spiral is the result (see Figure 5.7). This can then be used to describe the behaviour of the radar echo of the meteor trail as it evolves (e.g. see *McKinley* [1961]).

An expression for the amplitude can now be given as

$$E_R = (\frac{R_o\lambda}{4})^{1/2} (2Z_o\Phi_e)^{1/2} q(C^2 + S^2)^{1/2} \tag{5.16}$$

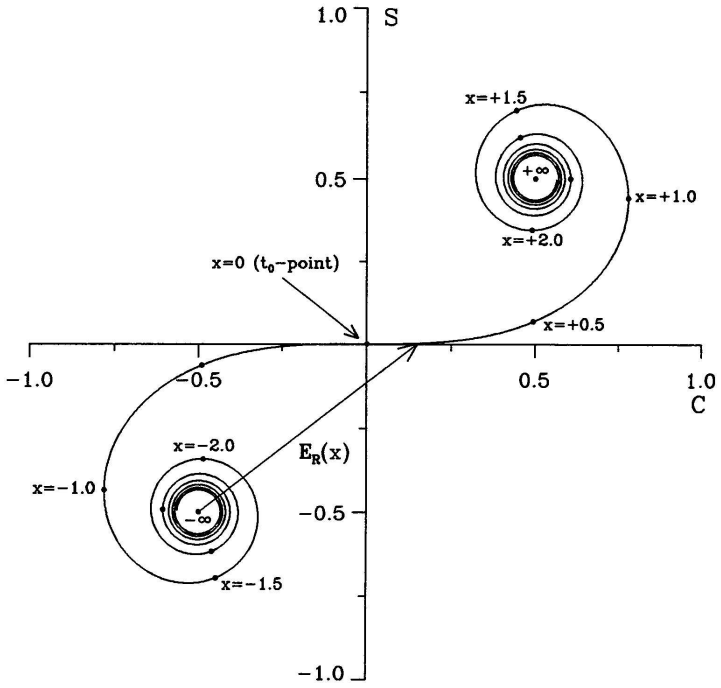

Figure 5.7: Cornu Spiral [*Cervera*, 1996].

The power flux is [*Ceplecha et al.*, 1998]

$$\Phi_R = \frac{(E_R)_o^2}{2Z_o} = \Phi_e(\frac{R_o\lambda}{4})q^2(C^2+S^2) \tag{5.17}$$

When the antenna is matched to the receiver, the effective absorbing area is given by

$$A = \frac{G_R\lambda^2}{4\pi} \tag{5.18}$$

Using $R \sim R_o$ and substituting equation 5.8 and 5.9, the power delivered to the receiver by the scattering from the complete trail is [*Ceplecha et al.*, 1998]

$$\begin{aligned} P_R &= \Phi_R\frac{G_R\lambda^2}{4\pi} && (5.19)\\ &= \Phi_e(\frac{R_o\lambda}{4})q^2(C^2+S^2)\frac{G_R\lambda^2}{4\pi} && (5.20)\\ &= \Phi_i\frac{G_R\lambda^3}{16\pi R_o}q^2r_e^2(C^2+S^2) && (5.21)\\ P_R &= \frac{P_TG_TG_R\lambda^3q^2r_e^2}{64\pi^2R_o^3}(C^2+S^2) && (5.22) \end{aligned}$$

If there are several Fresnel zones either side of the t_0 point, $C^2+S^2 \approx 2$, so we can

write for an underdense trail

$$P_R = 2.51 \times 10^{-32} \frac{P_T G_T G_R \lambda^3 q^2}{R_o^3} \tag{5.23}$$

If it is assumed that $x = 2Vt/(\lambda R_0)^{1/2}$, the intensity and phase for an idealised underdense trail can be determined. In Figure 5.8, curve A represents such a case.

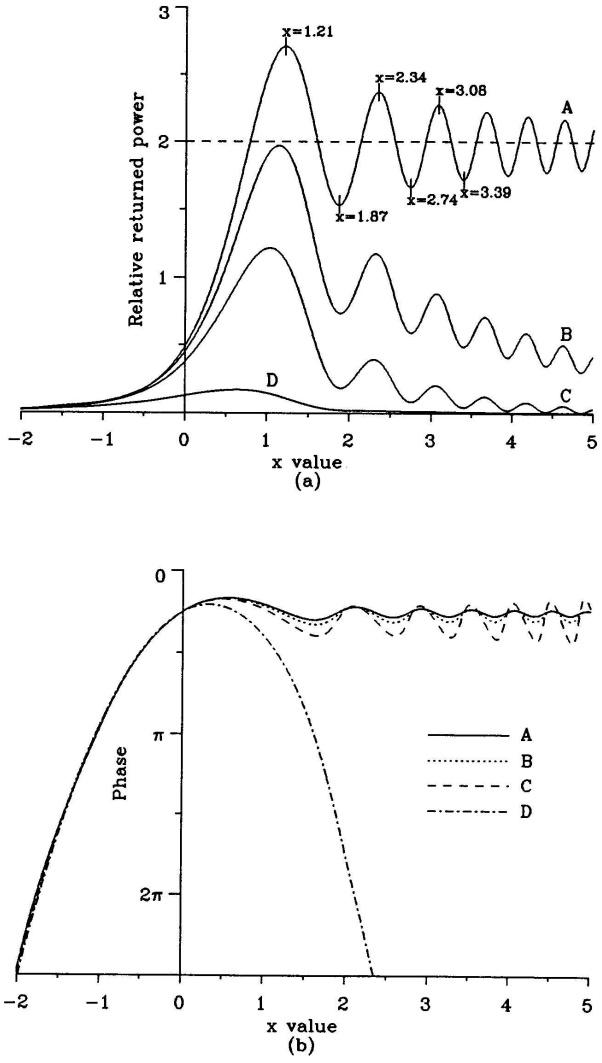

Figure 5.8: Idealised power (upper diagram) and phase (lower) behaviour of a radar meteor echo. Curve A shows the case for no diffusion, Curves B to D show the cases for increasing diffusion [*Cervera*, 1996; *Ceplecha et al.*, 1998].

The full wave treatment of the reflection of radio waves from a meteor trail incorporates the effects of the polarisation of the transmitted radiation [*Poulter & Baggaley*, 1977; *Poulter & Baggaley*, 1978] following previous research in this field [*Herlofson*,

1951; *Greenhow*, 1952; *Manning*, 1953; *Keitel*, 1955; *Brysk & Buchanan*, 1965; *Lebedinets & Sosnova*, 1968; *Jones & Collins*, 1974]. This allows the processes occurring with trails having densities in the transition region of 10^{13} to 10^{15} e/m to be better described by incorporating other facets of actual trails not catered to in the previous cases. Processes such as plasma resonance within the trail which occurs with specific incident polarisation and Gaussian distribution of ionisation are included in this revised theory. The work of *Poulter & Baggaley* calculated reflection coefficients, polarisation ratios and phases from a column of meteoric ionisation using the wave matching technique and compared the results with available experimental data to verify the theory. Their results were calculated for electron line densities over the range of 10^{12} to 10^{16} m^{-1} with densities in the region of 10^{13} signifying the detection limit of many backscatter meteor radars.

Assuming the train is instantaneously formed, neutral, uniform in cross section and infinitely long, the Gaussian radial electron density (n) is given [*Poulter & Baggaley*, 1977; *Poulter & Baggaley*, 1978] as

$$n(r,t) = \frac{\alpha}{\pi a^2} e^{-r^2/a^2} \tag{5.24}$$

where

$$a^2 = r_0^2 + 4D_a t \tag{5.25}$$

and α is the electron line density, r_0 is the initial train radius, D_a is the ambipolar diffusion coefficient and a is a measure of the column radius at time t. *Poulter & Baggaley* note that the effect of the geomagnetic field is ignored as the electron gyro frequency is much less than the radio frequencies typically used. Also omitted from the theory is the radiation damping of individual electrons. This treatment is appropriate for meteors observed at VHF but needs to be modified for the case at MF. At these lower frequencies the assumption that the electron gyro frequency is much less than the radio frequency is not applicable. This results in a modification of the general reflection coefficient treatment presented below. The modified theory is left for treatment elsewhere.

The reflection coefficients of plane waves parallel ($g_{\parallel}$) and perpendicular ($g_{\perp}$) are resolved from a trail incident plane wave of arbitrary polarisation and the solutions for the reflection coefficient magnitudes are displayed in Figure 5.9. In this formulation

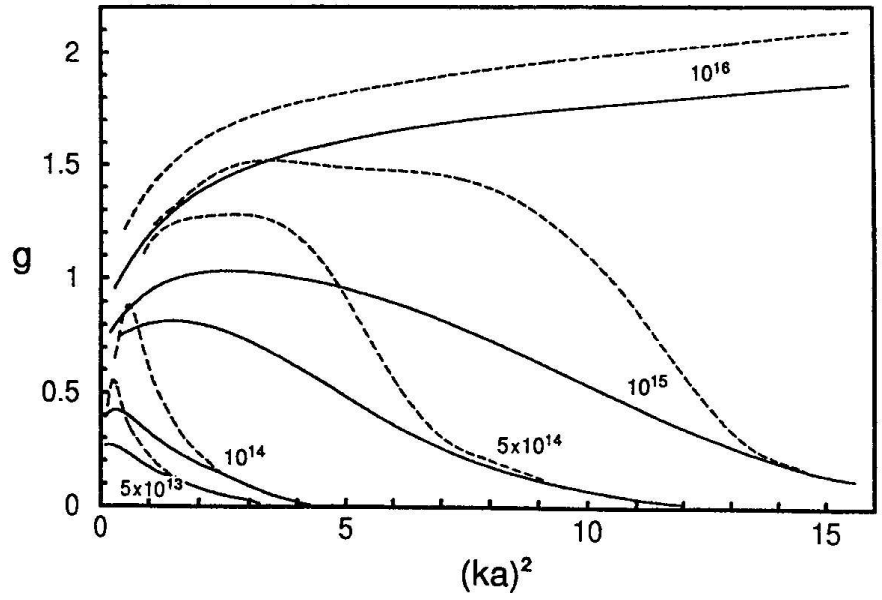

Figure 5.9: Reflection coefficients for parallel and transverse polarisations ($g_{\parallel}$ solid, $g_{\perp}$ dashed) (from *Ceplecha et al.* [1998] after *Poulter & Baggaley* [1977]).

$(ka)^2$ is proportional to time (or $ka \propto t^{1/2}$ in Figures 5.10 and 5.11).

Poulter & Baggaley note that the derived parallel reflection coefficient for cases where $\alpha \lesssim 10^{13}$ m^{-1} is also sufficiently defined [*Kaiser & Closs*, 1952] by

$$g_{\parallel} = \alpha \pi r_e e^{-(ka)^2} \tag{5.26}$$

where r_e is the classical electron radius. As electron densities take on values in the transition region it is apparent from Figure 5.9 that underdense and overdense behaviour is present while as $\alpha \gtrsim 10^{16}$, characteristic overdense behaviour dominates.

If the bimodal reflection coefficients are combined as a ratio ($\rho = g_{\perp}/g_{\parallel}$), Figure 5.10 results. The polarisation ratio attains a maximum relatively quickly for the underdense case, then tends to unity as the ionisation density gradient decreases due to diffusion. A contrast to this behaviour is that of the overdense case where the polarisation maximum is reached at a much later stage in the echo lifetime. For instances

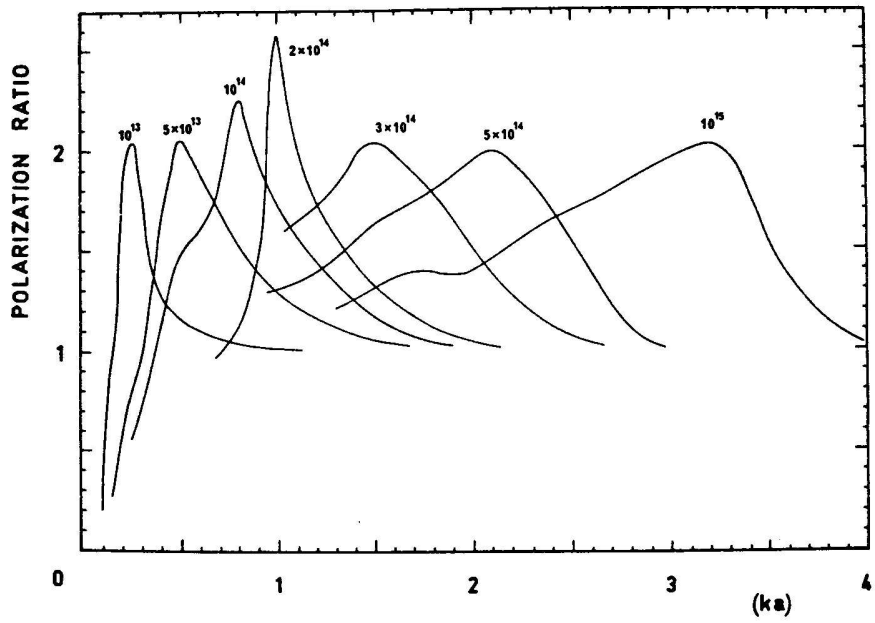

Figure 5.10: Polarisation ratio ($\rho = g_\perp/g_\parallel$) for selected electron line densities [*Poulter & Baggaley*, 1977].

where $\alpha \gtrsim 10^{16}$ m^{-1}, the trend of Figure 5.10 is continued such that ρ is near unity in the formative stages of the echo [*Poulter & Baggaley*, 1977].

The phase angle of the reflection coefficient represents the phase difference between incident and reflected waves [*Poulter & Baggaley*, 1978]. The constant phase behaviour at line densities $\alpha \lesssim 10^{13}$ m^{-1} is due to the incident wave remaining unchanged as it penetrates the plasma, while the transition region densities phase decreases early as the scattering cylinder undergoes expansion and starts to increase as diffusion decreases its volume density to a point where it collapses.

The Earth's magnetic field has an influence on the meteor trails, particularly at height >95 km, and the preceding theory has neglected this for the most part. Previous researchers have attempted to incorporate magnetic field effects on the formation of ionised trails (e.g. *Kaiser et al.* [1969]; *Pickering & Windle* [1970]; *Jones* [1991]; *Elford & Elford* [1999]), but it was not until recently that the magnetic field's influence on the dispersion of a meteor trail has been placed in the context of mainstream plasma physics [*Robson*, 2001]. This has allowed the influence of the geomagnetic field to be

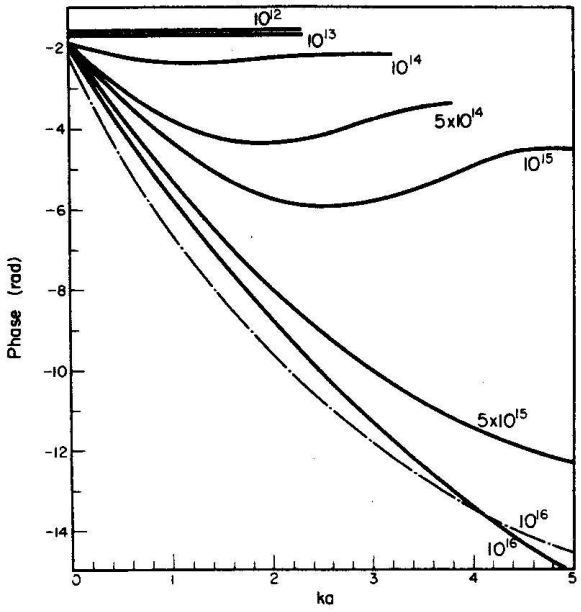

Figure 5.11: Phase angle in radians for the reflected wave, parallel polarisation. Full wave theory (solid line), Metallic cylinder (dashed), from *Poulter & Baggaley* [1978].

estimated at all heights.

The effective orientation-dependent diffusion coefficient is given [*Robson*, 2001] by

$$D_{eff} = D_{\parallel}\, sin^2\mu\, \sin^2\theta + D_{\perp}\,(1 - \sin^2\mu\, \sin^2\theta) \tag{5.27}$$

where μ is the angle between the wave vector and the normal to the plane of the trail and the field, θ is the angle the field makes with the trail and $D_{\parallel}$ and $D_{\perp}$ are the ambipolar diffusion coefficients parallel and perpendicular to the magnetic field.

The perpendicular ambipolar diffusion coefficient is related to the parallel component by

$$D_{\perp} = \frac{D_{\parallel}}{1+\rho} \tag{5.28}$$

and ρ is given [*Elford & Elford*, 2001] by

$$\rho = \frac{\omega_e \omega i}{\nu_e \nu_i} \tag{5.29}$$

where $\omega_{e,i}$ and $\nu_{e,i}$ are the gyro and collision frequencies of the electrons and ions.

At heights below approximately 95 km the atmospheric density is high enough to facilitate a high collision frequency of electrons with atmospheric atoms and molecules.

This results in the Earth's magnetic field having a negligible affect on the electrons trajectory. At heights above 95 km, this collision frequency decreases and the magnetic field has an increasing influence on electron behaviour, resulting in an anisotropic diffusion of the trail.

Subject to geometrical considerations, such as the orientation of the magnetic field and meteor trail, a significant effect of the Earth's magnetic field at heights above 95 km is to increase the lifetime of the echo in contrast to the expected rapid decay in the absence of the field.

Based on the theoretical work of *Robson* [2001], the effect of duration enhancement in a practical context has been investigated by *Elford & Elford* [2001] and re-examined by *Elford* [2003*d*]. *Elford* [2003*d*] recast the expression for D_{eff} (see Equation 5.27) in terms of the direction of the magnetic field and the direction of the radar beam. An illustration of the enhancement in echo duration is provided for the MU radar (34.85°N, 136.10°E, geomagnetic dip 51°) and Figure 5.12 displays the expected duration enhancement of an echo as a function of beam elevation angle for selected heights (95, 100, 105, 110 km). Here, an enhancement reaches a maximum value when beam elevation is 39°. The magnitude of these duration enhancements range from 2 at 95 km to 550 at 110 km and it is also apparent that significant enhancements occur away from the orthogonality condition. For other narrow beam radars similar results are obtained with the peak duration enhancement values always occurring at a beam angle that is the complement of the dip angle at the radar site [*Elford & Elford*, 2001].

As noted previously, the geomagnetic dip angle affecting the BP research facility is 67°. This requires a beam elevation of 23° to obtain a maximum duration enhancement of the meteor echo. This small elevation angle represents a larger off-zenith angle than for which the antenna array was designed, such that beam integrity is seriously compromised at this high off-zenith angle. In this study, no off-zenith angles greater than 40° were employed. This results in the beam angle residing approximately 30° from any maximum duration enhancement and thus a much reduced magnetic field effect is expected in the current utilisation of the equipment.

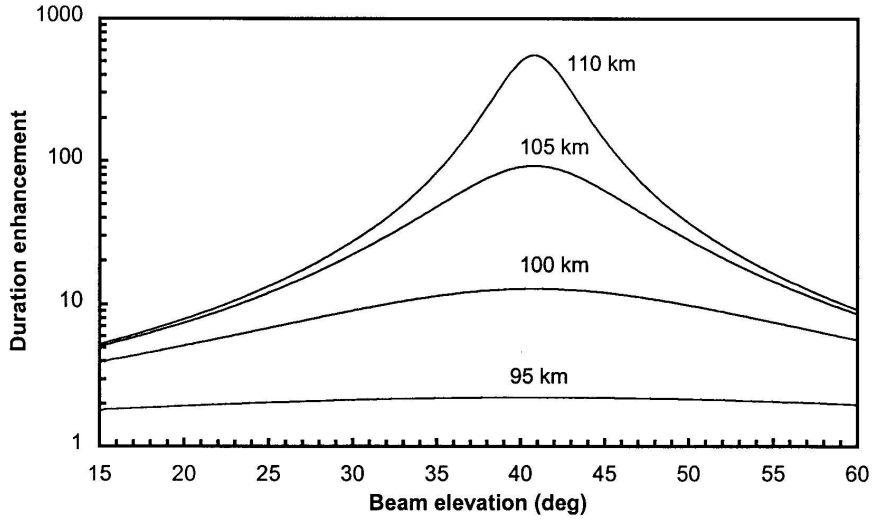

Figure 5.12: Expected duration enhancements of underdense meteor echoes from trails detected with the MU radar [*Elford*, 2003*d*].

5.3 Meteor parameters

A meteor ablating in the upper atmosphere as observed by radio techniques offers the dual opportunity of deriving parameters inherent in the meteoroid itself and of the environment through which it has travelled. The distinction is made here that, while MF-VHF radars observe the trail left by an ablating meteoroid and not the meteoroid itself, many parameters derived from the newly formed trail are an inherent property of the meteoroid. Parameters such as reflection point angle-of-arrival (and radiant), height and meteoroid speed are examples and these will be termed *intrinsic* meteor parameters. Alternatively, *atmospheric* parameters derived from the radio echo allow investigation of the environment surrounding the meteor by using the trail as a probe or tracer. Examples of such parameters that can be extracted from suitable meteor echoes are winds, diffusion coefficients, ozone concentration, pressure and temperature. Figure 5.13 summarises this classification scheme and provides references to some examples of particular techniques.

It is recognised that this classification scheme division is not absolute. Atmospheric processes often have an influence on meteor events (e.g. wind shear) while the converse is also true. For instance a large ablating meteoroid can create intense ion layers (like

sporadic E-layers [*Hughes*, 1978]) that may persist for some time after its passage, thus having a significant impact on the local atmospheric region. The temporal evolution of such layers is illustrated in Figure 5.14 as a possible outcome of meteoroid ablation.

While the importance of meteor intrinsic parameters has been touched upon previously, the parameters derived from the meteor tracer are also important in studies of the atmosphere. Often wind estimates derived from meteor echoes are the only viable technique to obtain information above an altitude of 100 km, with rocket probing techniques typically being prohibitively expensive and not offering the desired temporal coverage. A brief survey of the intrinsic parameters available from radio techniques is made with a focus on those applicable to the single station radar system used in this study.

5.3.1 Intrinsic meteor parameters

5.3.1.1 Meteor trail reflection point angle of arrival

The position of the reflection point of a trail in space above a radar site as measured by the direction of arrival of the reflected radiation is here termed the meteor angle-of-arrival (AoA). This parameter has also been termed the direction cosine of the trail. The determination of meteor AoA, coupled with knowledge of the trail scattering mechanism allows radiant information to be obtained. In addition to this, the AoA information can be subsequently used to determine other parameters such as meteor heights. The utility of this parameter establishes it as vital in the meteor studies described here.

A wide range of techniques to determine AoA have been developed and applied to middle and upper atmosphere targets but most can be divided into interferometric and non-interferometric classes.

Non-interferometric techniques typically only utilise the amplitude of the echo, due to the unavailability of phase information in non-coherent radar systems. This amplitude information is often coupled with known system hardware orientation information

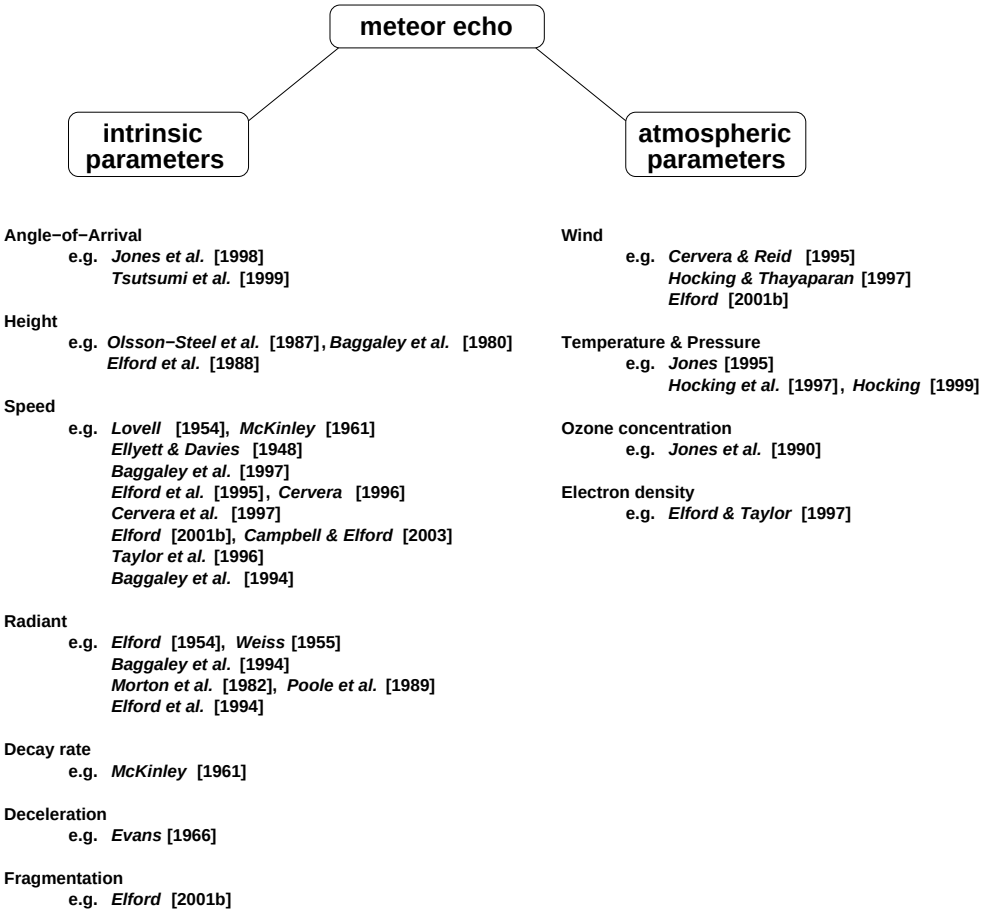

Figure 5.13: Possible parameters available from meteor echoes. Parameters are sub-divided into intrinsic and atmospheric with references noted for examples of a specific (horizontal listing) or alternate (vertical) technique to obtain the highlighted parameter. See text for discussion of selected (AoA, height, speed and radiant) techniques.

to reduce AoA. An example of this technique is where the zenith angle of the target is determined by the comparison of echo amplitudes excited on two antenna systems with different known antenna patterns in the vertical plane [*McKinley*, 1961]. A more commonly applied, non-interferometric technique involves the use of a narrow transmit beam directed at a known azimuth and zenith angle (e.g. *Elford & Olsson-Steel* [1988]; *Cervera* [1996]). If it is assumed that the only meteors detected are due to the formation of a trail perpendicular to the radar beam (i.e. the transverse case) the AoA is thus strictly defined. Also, if three receiving stations are available the position of the target can be reduced from triangulation of radar ranges [*McKinley*, 1961].

Interferometric techniques in various guises have been applied to targets in the

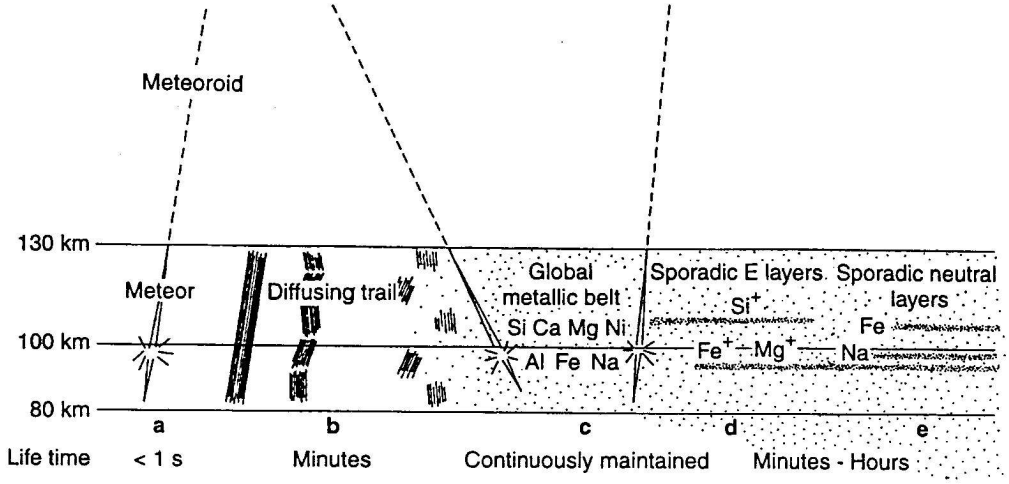

Figure 5.14: Layer formation from meteoric deposition in the atmosphere. The visible meteor (a) is instantaneous while its trail (b) can be observed for minutes. The deposition of meteoric matter continuously maintains the global metallic belt (c) while sporadic layers (d) can form occasionally and sporadic neutral layers (e) can form simultaneously, with both layers able to persist from minutes to hours (from *Pellinen-Wannberg et al.* [1998]).

Earth's atmosphere since investigations into the ionosphere began (see e.g. *Sherrill* [1971]). Current application of the technique to the middle and upper atmosphere typically involves the comparison of phase information from a pair or more of spaced receivers. Direction of arrival is able to be determined if the single plane wave source model is assumed [*Sherrill*, 1971]. In terms of the echo from a newly formed underdense meteor trail at lower thermospheric heights this assumption is valid. An early implementation of the basic interferometric technique still commonly applied today uses three receivers arranged at the corners of a triangle [*Robertson et al.*, 1953] and exploits the difference in phase detected at each receiver for AoA determination.

To enable an unambiguous determination of AoA using the interferometry technique (from any position in the full hemisphere centred on the radar site), the spacing of antennas should be not more than 0.5λ. However, at these close antenna spacings mutual coupling between each element is high and if expected AoAs are nearer to the zenith (as is the case in many atmospheric applications), increasing inter-element spacing reduces the mutual coupling for the expected targets. This, however, will introduce ambiguity into the AoA for significant off-zenith angles. A common method to

alleviate this ambiguity is to use additional elements at differing separations. This arrangement often required more receivers and increased the amount of data collected, resulting in a dramatic increase in post processing of the data in order to extract unambiguous AoA. It was not until the advent of faster microcomputers and their incorporation into radar systems that this level of data manipulation became manageable [*Jones et al.*, 1998] and has contributed to the wider implementation of this technique.

A typical implementation of the interferometer is by *Tsutsumi et al.* [1999]. In their arrangement using the BP MF antenna array five dipole elements were employed. The configuration consists of a small and large isosceles triangle with a common apex element. This configuration can also be viewed as a crossed baseline interferometer. The smallest element spacing is 0.60λ and thus ambiguities arise from zenith angles greater than $56.4°$. To address this situation the large triangle is used to determine more accurate AoA from the angle possibilities indicated by the smaller triangle.

An extension of this type of arrangement is that of *Jones et al.* [1998]. Five elements are employed in a crossed baseline interferometer utilising a common centre element. In this extension of the basic interferometric technique, the selection of unambiguous AoAs is based on estimates of the mutual coupling between antenna elements. This type of arrangement has been implemented on an increasingly wider basis due to its potential for full hemisphere AoA utilising a minimum of antenna receiving elements in a compact arrangement [*Brown et al.*, 1998; *Holdsworth & Reid*, 2002].

Hocking [1989] notes that interferometer methods enable high resolution studies provided the scatter originates from a preferred region of the sky and is of narrow angular extent. This condition is satisfied by most meteor trail events initially. However, due to the environment into which the trail is formed there may be other structures contributing to the trail echo or the trail echo itself may present a non-ideal target if adversely affected by atmospheric motions [*McKinley*, 1961]. This can lead to the assumptions used in the interferometric analysis to break down. This may account for a failure in angle-of-arrival determination via interferometry in particular cases.

A possible, but less likely cause, is the simultaneous reflections from different directions occurring in the lower E-region lasting several seconds as noted by *Jones* [1981]. However, this is a rare event for most meteor radars.

5.3.1.2 Meteor height

The height of formation of the meteor trail above the radar station is an important meteor parameter. As mentioned previously, the peak in meteor height distributions increases with decreasing radar frequency. This suggests that a significant component of the meteoroid population has not been adequately detected which has implications for the estimates of the total influx into the Earth's atmosphere. In the narrow beam systems, height is determined directly from the range gate of the meteor signal with highest SNR [*Elford & Olsson-Steel*, 1988; *Steel & Elford*, 1991], while interferometric systems typically use the cosine of the zenith angle to reduce meteor trail height [*Olsson-Steel & Elford*, 1987; *Baggaley & Webb*, 1980].

5.3.1.3 Meteoroid speed

The estimation of the scalar speed of meteoroids has importance at a number of different levels in the overall research into extra-terrestrial bodies impacting the Earth's atmosphere. Primarily, single station speed estimates allow stream membership identification, while many other meteors parameters have speed dependencies (e.g. ablation coefficients, initial trail radius, etc.) [*Baggaley et al.*, 1997]. Coupled with precision trajectory information, velocities can be also deduced. This generally requires the use of more complex multi-site radar systems but the resulting meteor orbit data is of value in isolating the sources or parent bodies.

Meteoroids that are members of the solar system will exhibit pre-atmospheric speeds in the range of 11.2 to 72.8 km s^{-1} [*Ceplecha et al.*, 1998][5]. Meteoroids in

[5]Parabolic velocity at Earth's perihelion (42.5 km s^{-1}) plus velocity of the Earth at perihelion (30.3 km s^{-1}).

heliocentric hyperbolic orbits have the potential to display speeds greater than this range and thus provide evidence of possible interstellar origins (e.g. *Taylor et al.* [1994]; *Ceplecha et al.* [1998]). Meteoroids suffering notable deceleration (or severe fragmentation, etc.) may result in speeds below this expected range, although non-meteor sources, such as space debris may also be responsible (see for instance *Cervera* [1996]).

A meteoroid colliding with the Earth's atmosphere is a dynamic process, with the final outcome dependent on the intrinsic properties of the meteoroid (e.g. its composition (stony, non-stony, etc.) as well as trajectory, mass, etc.) and that of the environment in which it ablates (e.g. wind shear, diffusion coefficient, etc.). If observed by radar techniques the resulting echo is also dependent on the radar's operational characteristics such as frequency, beam direction, beam width and transmitter power, for instance. This range of variables results in the accumulation of meteor echoes that, while readily identifiable as meteor events, can exhibit widely differing characteristics in their amplitude and phase series. For instance, with MF to VHF radar systems, a transmitted beam perpendicular to the ionised trail will often result in classic Fresnel behaviour, while a meteoroid moving down through the beam will produce a moving ball target behaviour. The former events are far more abundant than the latter. This variation in echo characteristics has seen the development of numerous techniques to ascertain meteoroid speeds.

Individual techniques can be classified according to the primary radar information that they utilise (e.g. amplitude, phase, range, time etc.) and often can be further sub-divided within these groups on the basis of pre- or post-t_0 signal utilisation. This type of classification has a bearing on the applicability of individual techniques at medium frequencies and this is apparent in the various speed determination techniques surveyed below. Such a survey is particularly appropriate considering the lack of meteor speed studies undertaken at these relatively low observation frequencies and because of the specific demands placed on such techniques more widely implemented at higher frequencies. Specific techniques evaluated are the a) range-time; b) Fresnel oscillation;

c) differential or rise speed; d) quadratic; e) Fresnel phase time; f) Fresnel holography; g) inter pulse phase time and h) time of flight methods. A brief description of the technique together with its applicability, advantages, disadvantages and considerations if applied to MF observations is provided.

The **range-time** method was the technique first applied to obtain meteoroid speed [*Hey et al.*, 1947; *Hey & Stewart*, 1947] and is extensively described in [*Lovell*, 1954; *McKinley*, 1961; *Millman*, 1968]. If a meteoroid is assumed to move in a straight line trajectory at a constant speed through the radar beam it will produce a hyperbolic profile on a range-time representation of the radar data where the scattering is assumed to come from the ionisation at the "head" of the trail. This is in contrast to the aspect sensitivity and hence constrained angle of incidence of the transmitted radiation of the transverse type scattering. The speed is given by $R^2 = R_0^2 + V^2(t - t_0)^2 = R_0^2 + s^2$ where s is the distance along the path relative to the point nearest the radar [*McKinley*, 1961]. Depending on the characteristics of a particular echo *McKinley & Millman* [1949*a*] described four approaches (curve-fitting, range × dR/dt, three-point or parabolic regression) that may by applied to determine speed based on this theory (see also *Lovell* [1954]). This technique was applied extensively in early meteor radar systems primarily due to the common presentation of the radar data of the period but exhibits a number of disadvantages in that it required bright meteor events extending over many kilometres in height for accurate speed reduction [*McKinley*, 1961], high power radars and that the radar range resolution be high. This limited the number of meteors suitable for processing. Reasons for excluding this technique for further evaluation at MF included, the lack of observed head echoes at MF during trial data collection, the limited height resolution of the current MF system and the greater scope for improvement offered by alternate methods.

The **Fresnel oscillation** or **diffraction** technique was first applied by *Ellyett & Davies* [1948] after *Herlofson* proposed the technique based on the diffraction theory of radio waves applied to a meteor trail given by *Lovell & Clegg* [1948]. The technique has been described by various authors (e.g. *McKinley* [1961]; *Taylor et al.* [1994];

Cervera [1996]) and is analogous to the case of optics diffraction at a straight edge. Essentially the post-t_0 amplitude oscillations of a meteor echo, assuming a trail orientated transverse to the beam bore sight are predicted by Fresnel diffraction theory (see section 5.2.2) and will give meteor speed if a sufficient number of oscillations are discernible from the echo record. The technique has been consistently applied to radio meteors since its inception and is still in use in current meteor analysis with various studies citing percentages of meteors to which this method can be applied as being in the range of 1-20%. An example of a modern implementation of this technique is displayed in Figure 5.15. This displays a speed determination from one of the three receiving sites of the Advanced Meteor Orbit Radar (AMOR) facility [*Baggaley et al.*, 1994].

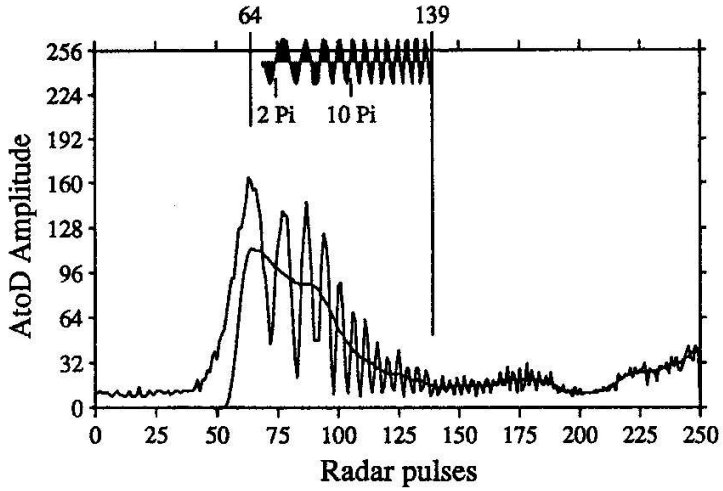

Figure 5.15: Speed determination using the Fresnel oscillation technique (from *Baggaley et al.* [1994]). The echo profile, mean amplitude level and extracted oscillatory function are displayed. A speed of 25.5 km s^{-1} was determined from this profile.

An advantage of this technique is that it is applicable to CW and pulsed radar systems. When applied to CW radar data, the amplitude fluctuations also appear preceding the t_0 point. This is of an advantage in two senses. First, the pre-t_0 oscillations are not significantly affected by diffusion and secondly they are less affected by wind shears or distortions such that initial and final meteor speeds may be deduced.

However CW radar systems are more complex and their use has declined in many

cases in the ensuing years. This results in the technique being applied for the most part to the post-t_0 oscillations and requires a high PRF to delineate the individual oscillations. Utilising a high PRF has the consequence that at higher transmission frequencies aliasing in range may be introduced, and at medium transmission frequencies ionospheric scatter effects may render the selected pulse repetition frequency unusable. *Baggaley et al.* [1994] and *Elford* [2001*a*] point out that fragmentation will also affect the integrity of the oscillations. In particular, the absence of these oscillations has been considered a hallmark of fragmentation [*Elford & Campbell*, 2001]. Also affecting these oscillations, if present, is the action of the background wind. These effects result in a decline in the technique's applicability brought about by the implementation of quality control criteria on the candidate echo. In addition to this is the consideration that the accuracy of the technique is dependent on the number of clear oscillations in the time series.

The 2 MHz trial data collected during various showers indicated the poor quality of the post-t_0 oscillations in most meteor events. Typical PRFs tested during this period ranged from 20 to 100 Hz. It was apparent that a PRF <60 Hz was too low to identify distinct oscillations in many cases. Similarly the significant effects of wind shears and other distortions were also apparent. Possible application at MF would require meteors near the lower speed limit and to occur in the presence of ideal atmospheric and ionospheric conditions.

In an effort to obtain speeds from significantly higher numbers of meteor echoes than the Fresnel oscillation technique offers, *Baggaley et al.* [1997] developed a technique that also exploits the Fresnel amplitude time series, here termed the **differential** or **rise speed** technique. This technique utilises the amplitude echo region up to and including the amplitude maximum. From the equation $s = \frac{(R\lambda)^{1/2}}{2}x$ (see page 252), the meteor speed can be given as

$$v = \frac{(R\lambda)^{1/2}}{2}\frac{dx}{dt} \tag{5.30}$$

Using the behaviour of the Fresnel integrals this reduces to [*Baggaley et al.*, 1997];

$$v = \frac{\rho_{max}(R\lambda)^{0.5}}{2\tau A_{max}} \left[\frac{\Delta A}{\Delta n}\right]_{max} \tag{5.31}$$

where ρ is the length of the resultant amplitude $(C^2 + S^2)^{1/2}$ and $\rho_{max} = 1.657$ when $x = 1.217$, A is the echo amplitude and τ is the pulse sampling interval. Thus peak amplitude echo measurements and maximum gradients of the amplitude series allow meteor speed to be determined. This is illustrated in Figure 5.16. *Baggaley et al.* [1997] also note that this relation should be modified on the basis that the trail will suffer from distortion effects and noise will contaminate the echo profile. While no specific comparisons have been made as yet, this technique is expected to be applicable to many more meteors than the Fresnel oscillation technique, primarily due to its use of the echo amplitude preceding the peak, which is consistently identified in most meteor echo data. An unfavourable aspect of this technique is that the seven point differentiation scheme implemented in the available study precluded the determination of speeds for fast meteors due to the selected sampling rate. Nominal accuracy is stated at better than 10%. In terms of this technique's application to MF meteor events the required number of samples preceding the amplitude maximum are not available in most cases for its implementation as described. This is a direct consequence of the relatively low sampling rate of the MF system in its practical application to meteor observations and the often low SNR of the meteors themselves which results in a limited number of noise free amplitude samples for analysis. Implementing this technique at MF would thus require a higher PRF in most cases, however it may be possible to apply it on low speed meteors at a PRF of 60 Hz. Alternatively, implementing a different differentiation scheme using fewer points may be worthwhile.

With the proliferation of coherent radar systems in recent decades, the meteor echo phase has been examined for its suitability for speed estimates. One technique that has been successfully applied using this component of the meteor signal is where a **quadratic** function is fitted to the pre-t_0 phase [*Elford et al.*, 1995; *Cervera*, 1996]. As described previously, the phase of the diffraction pattern is given by $\phi = \tan^{-1}(S/C)$

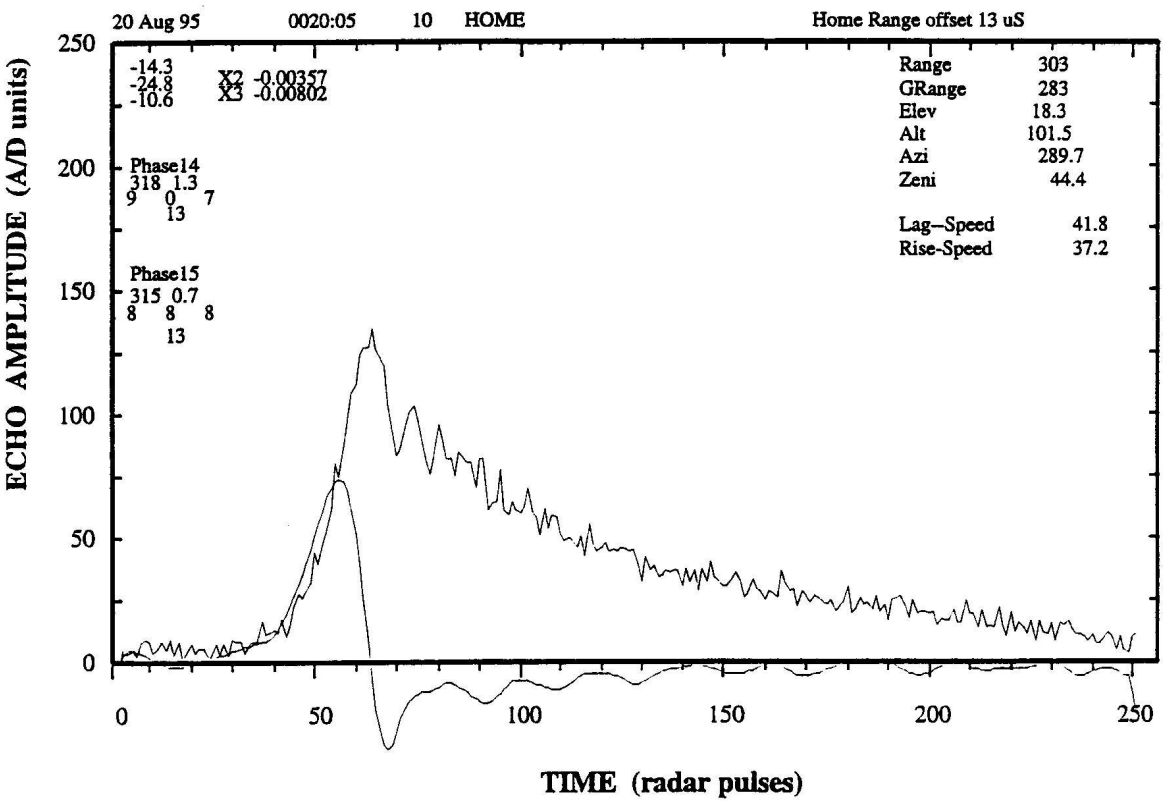

Figure 5.16: Speed determination using the rise speed technique (from *Baggaley et al.* [1997]). The signal amplitude and its first derivative are displayed. Calculated speed is 37.2 km s^{-1}. Also note the lag speed calculation of 41.8 km s^{-1} for this echo. This is obtained via the time interval technique as described in the text.

where S and C are the Fresnel integrals of Equation 5.2.2. The Cauchy approximations to the Fresnel integrals (excluding the region $-1 < x < 1$) are

$$C = \frac{1}{\pi x}\sin\left(\frac{\pi x^2}{2}\right) \qquad \& \qquad S = -\frac{1}{\pi x}\cos\left(\frac{\pi x^2}{2}\right) \qquad \text{for } x < -1$$

$$C = 1 + \frac{1}{\pi x}\sin\left(\frac{\pi x^2}{2}\right) \qquad \& \qquad S = 1 - \frac{1}{\pi x}\cos\left(\frac{\pi x^2}{2}\right) \qquad \text{for } x > 1$$

From this an expression for the phase can be obtained, assuming no deceleration, such that [*Cervera*, 1996]

$$\phi_{x<-1} = \frac{2V^2}{R_0\lambda}t^2 \tag{5.32}$$

Again, no specific data are available on the proportion of echoes that this technique is applicable to, but it is expected that a significantly larger population than the

Fresnel oscillation technique is a realistic estimate. This efficiency is primarily due to the utilisation of the phase portion of the echo which exhibits a high degree of coherence under limited SNRs and atmospheric distortion processes. The technique is also straightforward to apply in low sampled meteor time series where it requires only three or more data points for a meteor speed. Drawbacks of this technique are that it is only valid for $x<-1$ which can limit the number of samples available for inclusion in the fitting process. The accuracy achievable is dependent on the number of representative samples included in the analysis but typically ranges from 0.5% [*Elford et al.*, 1995] to ~10% [*Cervera*, 1996]. Applying this technique at MF is a distinct possibility given its requisite number of samples, however, the constraint of the Cauchy approximation's validity further reduces the available number of samples from any typical MF echo profile because the low SNR MF echoes have a limited number of pre-t_0 phase points.

Another technique that utilises the pre-t_0 phase information is the **Fresnel phase-time** method or **pre-t_0** technique [*Cervera*, 1996; *Cervera et al.*, 1997]. This technique uses the phase information of a meteor event from its emergence out of the background noise up to and including the phase minimum. This profile is then compared with a model phase profile to obtain a distance versus time plot representing the distance back along the trial. A least squares fit to this data will yield a meteor speed. Examples of this technique are displayed and discussed in section 6.3.3. In terms of applicability it has been suggested 70 to 75% of detected meteor events are suitable for implementation of this technique. As in the case of the quadratic fit technique the high SNR of this section of the phase profile facilitates this high applicability. Also, the technique is robust with regard to diffusion effects as it is apparent from the lower panel of Figure 5.8 that using the pre-t_0 phase region limits the effect of diffusion on the meteoroid speed determination. A further advantage of this technique is that as the speed is obtained by a linear fit to the data, only two data points are required for a result. This factor suggests the techniques suitability to data sampled at low frequencies, as is the case for high speed meteors or low PRFs used at MF frequencies. A disadvantage with this technique is that a speed is difficult to obtain for weak

signals (see *Campbell & Elford* [2003]), however this caveat applies for most alternate techniques. Technique accuracy ranges from 0.5 to 5%.

While best viewed as a more complete tool to investigate the often complex and varied structure of a meteor echo, the recently developed **Fresnel holography** technique of *Elford* [2001*b*] has a powerful capability in refining meteor speed determinations amongst other capabilites and is included here for evaluation as a possible speed determination technique to be implemented at medium frequencies.

The technique utilises a Fresnel Transform to examine the structure of the trail since the recorded variations in the amplitude and phase of radio signals scattered from a meteor trail can be viewed as a one-dimensional diffraction pattern produced by a moving source and thus lends itself to such a transform technique. Refering to Figure 5.17, if the complete trail is assumed to form within the radar beam (i.e. the MF radar's 10° beam width, at a minimum height of 80 km, covers approximately 15 km horizontally), the total scattered signal detected at the radar site (T) at an instant of time t is given by [*Elford*, 2001*b*]

$$E(t) \propto \int_{-\infty}^{x} G(z) \exp(j2kR)\, dz \tag{5.33}$$

where G(z) is the reflection coefficient of small element dz, and $t = x/v$, v is speed of the meteoroid, $k = 2\pi/\lambda$, and R is the range of P from the radar, which can be written as $R \cong R_0 + z^2/(2R_O)$, since $R_0 > 10z$. Using the established coordinate system where $z = x + y = vt + y$, the scattering function of the trail is given as

$$A(y) \propto \int_{-\infty}^{\infty} E(t) \exp(-jZ^2/2)\, dX \tag{5.34}$$

where the right hand side is the Fresnel Transform of the complex signal (E(t)) recorded at the radar station and $X = x/\sigma$, $Y = y/\sigma$, $Z = z/\sigma$ where $\sigma = [\lambda R_0/(4\pi)]^{1/2}$ [*Elford*, 2001*b*].

The intergration stated in Equation 5.34 necessitates the use of the complete radar echo time series and a meteoroid *seed* speed inherent in the relationship between X and t given by $X = (v/\sigma)t$. A technique to obtain this initial speed is the Fresnel

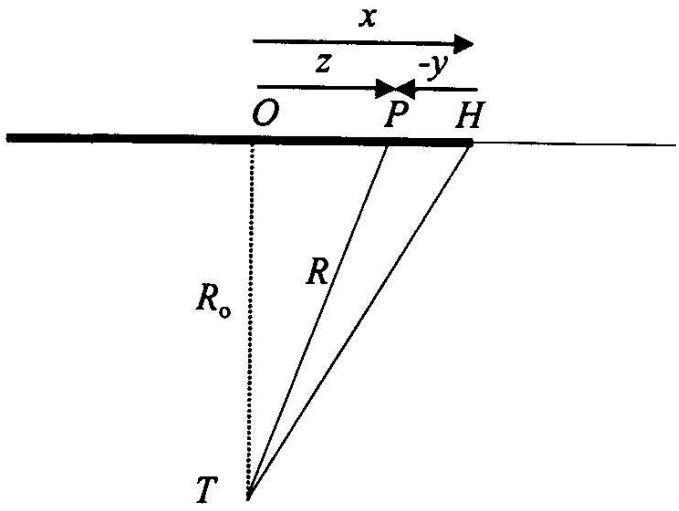

Figure 5.17: Geometry of the Fresnel holography technique (from *Elford* [2001*b*]).

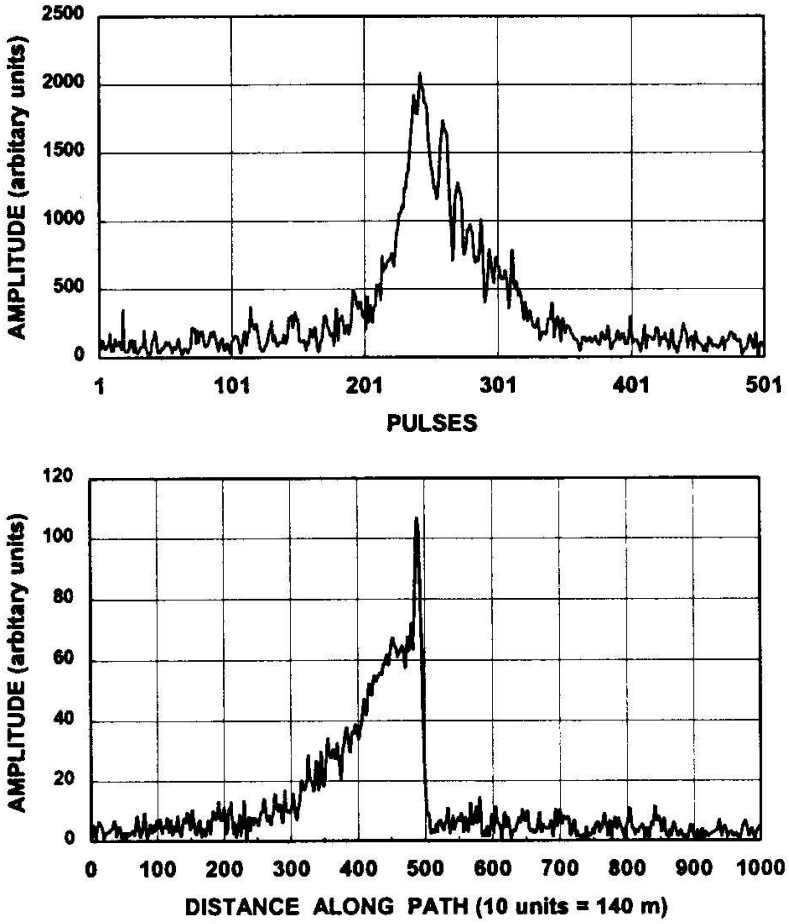

Figure 5.18: Speed determination using the Fresnel holography technique. Amplitude (upper panel) and reflectivity (lower panel) of a typical underdense echo observed at a height of 94 km. The meteoroid speed is 45.0 km s^{-1} and is determined from successive iterations of the scattering function to optimise the sharpness of the peak displayed in the lower panel (from *Elford* [2001*b*]).

phase time technique described previously [*Elford*, 2001*b*]. The amplitude of a typical underdense echo and the calculated scattering function is illustrated in Figure 5.18.

Succesive iterations at speeds above and below the initial seed speed affect the sharpness of the leading edge of the scattering function's main peak. This allows a precise meteoroid speed to be determined. A recent refinement of this process does not require a specific *seed* speed to be used but rather examines the outcome of the transform assuming various speeds and selects the speed that produces the most realistic image of the reflectivity (determined by the "sharpness" of the reflectivity) [*Campbell et al.*, 2002].

In terms of revealing previously unknown characteristics about a particular trail, this technique has been shown [*Elford*, 2001*b*] to have a broad applicability to many types of meteor echoes (such as underdense, overdense, head echo etc.) and this also translates to the determination of meteoroid speeds. The technique offers a high precision result in comparison to other techniques (see for example *Campbell & Elford* [2003]) as well as having the potential to identify multiple sources and thus confirm any fragmentation processes. Further advantages of the technique lie in a more accurate estimation of diffusion from the trailing edge of the scattering function amplitude as well as the potential for atmospheric wind estimation using the transform phase slope data. This information is inherent in the Fresnel transform processing and may provide a more convienient method to obtain these parameters in comparison to more traditional means.

In accessing the disadvantages of this technique, it is noted that more complex speed determination methods often require more computational resources. Here, each meteor echo requires multiple iterations to refine the initial meteor speed. In a modern VHF meteor radar system, trail echo rates can reach 8000 per day, which places strict demands on the amount of computational time available an algorithm has to ascertain near-real time speeds. However, data processed off-line or using significantly lower echo rate data (such as that described in this thesis) do not have this restriction. A further disadvantage is that the technique may be more suited to the higher sampling

rates of VHF meteor radar data. This is because the scattering function leading edge needs to be resolved sufficiently for the iteration process to be effective. In addition to this, a higher sampling rate reduces the occurence of aliasing. The much lower sampling rate of MF radar system is envisaged as the primary obstacle in applying this technique at 2 MHz.

A technique that is applicable to a smaller set of radar meteor echoes is the **inter-pulse phase time** method [*Taylor, Cervera, Elford & Steel*, 1996]. In this approach to speed determination, it is assumed that the echo originates from a meteor moving obliquely down through a narrow pencil beam leaving a range-time history of its travel. Thus all ranges are typically devoid of the Fresnel oscillations associated with the familiar underdense meteor that has a trajectory transverse to the beam bore sight. It is assumed that the reflection mechanism in effect here is that of the head echo type where a small segment of the meteor trail near the head is the radar target. An estimate of line-of-sight speed can be gained from the range-time history but further precision is obtained if the pulse to pulse phase changes are estimated for selected meteor speeds. The meteor angle of trajectory through the beam and deceleration characteristics can also be extracted. Due to the nature of the echo analysed in this technique it has limited application in dedicated meteor radars and less so at medium frequencies. Again the sampling rate of MF radars will preclude this technique from regular application at these lower frequencies.

While not applicable to single station radars, in a multi-receive station configuration, such as the AMOR system [*Baggaley et al.*, 1994], opportunities exist to utilise the timing of the appearance of the meteor echoes rather than the theoretical form of their amplitude or phase profiles to deduce meteor speed. In this technique, termed the **time interval** method, the timing of the maximum gradient of the echo amplitude at the three sites is determined to obtain the speed. It is assumed also that echo phase could be used equally well for event timing and may in fact offer some advantage over meteor amplitude due to its robust behaviour. With other information such as echo

height and trajectory, a meteor velocity can be further deduced. This method facilitates a dramatic increase in the number of detected meteor events that can provide a velocity compared to other techniques because the inherent quality of the echo (i.e. amplitude) is not as vital an issue as with other techniques. The technique also has the capability of determining speeds above the upper heliocentric closed orbit limit (72.8 km $^{-1}$) [*Taylor et al.*, 1994] where other techniques often fail. Accuracy for this technique is approximately 3%. A disadvantage of this technique is that, due to the geometry of the spaced receiver sites, each received echo profile is not from the exact same portion of the trail and this must be taken into account in the analysis. In addition to this, multi-station radar systems are inherently more complex and costly to construct than single station sites.

Velocity techniques applied using incoherent scatter UHF radar systems often use variations of the range-time technique. Typically, the line-of-sight (radial) speeds are determined as a meteor travels down the narrow beam and orbit information can be deduced from knowledge of the beam bore-sight position [*Mathews et al.*, 1997]. Later implementations determine the instantaneous line-of-sight speed from the pulse-to-pulse Doppler phase shift [*Janches*, 2000]

$$V = \frac{\Delta\phi\lambda}{4\pi\Delta t} \tag{5.35}$$

where $\Delta\phi$ is the pulse to pulse Doppler phase shift, λ is the radar wavelength and Δt is the pulse separation. The target is a head echo which more often than not displays a short lived plasma trail. Because of the inherent sensitivity of these high powered radar systems an advantage of this approach is that meteors of magnitude +14 can be observed.

This UHF technique, while not directly applicable to MF/HF/VHF meteor radars due to the increased sensitivity and height resolution capabilities that ultra high frequency radars possess coupled with the selection of non specular meteor head echo types, does illustrate the diversity of techniques employed to reduced meteoroid speeds. A most novel technique to determine meteor velocity at UHF is described by *Evans*

[1966], whereby the receiver is de-tuned from the transmitter frequency to bring the centre filter of the receiver to the expected Doppler shift frequency of an approaching shower meteor.

In terms of establishing the main criteria for speed technique selection at medium frequencies, preliminary meteor observations have highlighted the quality of the phase series of most meteor events. In many cases, the expected Fresnel phase series for meteor echoes is clearly discernible from the initial onset of the echo through to the beginning post-t_0 regions. This is in some contrast to the amplitude series which often are less tightly constrained to their theoretical form. This behaviour is particularly noticeable at low echo SNRs. As such, a technique utilising the signal phase is deemed more appropriate in terms of speed parameter yield from any particular set of data. Also, the lack of success in detecting down the beam or head echo meteors precluded the use of techniques developed specifically for these cases. A primary factor in the selection of an appropriate technique is the accommodation of the low sampling rate of the radar due to ionospheric and hardware limitations. Satisfying these conditions are the quadratic fit and Fresnel phase time methods. Trial evaluations indicated that the latter technique was effective in significantly more cases than the former and thus was implemented as the preferred technique for MF speed reductions.

A summary of selected techniques for determining meteor speed that were considered for application to medium frequency radars is displayed in Table 5.2. Each technique is accompanied by example references that originally described or later applied the process to meteor observations. This is followed by an indication of the type of radar data employed in the particular technique noting that traditional techniques often utilised amplitude information due to the limited availability of coherent radar systems. The specific region of this radar data employed in the algorithm is also identified where relevant. The technique's projected applicability to an ensemble of meteor observations is also tabulated. Where no data are available a percentage with respect to the well established 1-20% applicability of the Fresnel oscillation technique is given. This value varies for different radar systems and operating frequencies amongst other

variables, however major trends are nevertheless apparent. A small selection of technique advantages and disadvantages are pointed out with an emphasis on those aspects pertinent for evaluation at medium frequencies. Finally, accuracies are those quoted or where not available, an estimate of that expected to be achieved in general terms.

All techniques tabulated, except the time interval method, are single-station techniques. However, most single station techniques can be applied to, or incorporated in multi-station systems (e.g. *Baggaley et al.* [1994]) in some form.

Technique	References	Type	Applicability
Range-time	[*Hey et al.*, 1947] [*Hey & Stewart*, 1947]	Amplitude	Head echoes only
Fresnel oscillation or Fresnel amplitude-time or Diffraction	[*Ellyett & Davies*, 1948] [*Lovell*, 1954] [*McKinley*, 1961]	Amplitude (post-t_0)	$1 \rightarrow 20\%$
Differential or Rise speed	[*Baggaley et al.*, 1997]	Amplitude (pre-amp peak)	No data, but $\gg$20%
Quadratic fit	[*Elford et al.*, 1995] [*Cervera*, 1996]	Phase (pre-t_0)	No data, but >20%
Fresnel phase-time	[*Cervera*, 1996] [*Cervera et al.*, 1997]	Phase (pre-t_0)	75%
Fresnel holography	[*Elford*, 2001*b*]	Amplitude & phase (total signal)	No data but $\gg$20%
Inter-pulse phase change	[*Taylor et. al.*, 1996]	Phase, range & time	Down-the-beam echoes
Time interval	[*Baggaley et al.*, 1994]	Amplitude (pre-amp peak)	>90%

Table 5.2: A comparison of selected techniques for determining meteor speed.

Advantages	**Disadvantages**	**Accuracy**
Straightforward	Requires overdense meteors extending over large height range Requires high radar range resolution	Not known
Widely implemented	Distortions affect oscillations (e.g. diffusion, decay rate, wind, fragmentation etc.) Speed accuracy increases with more oscillations Minimum number of oscillations required	$2 \rightarrow 5\%$
Straightforward	Upper speed limit due to PRF and 7 point differential scheme	$<10\%$
Pre-t_0 phase less affected by distortions Requires ≥ 3 samples Straightforward	Valid only for $x<1$	$0.5 \rightarrow 10\%$
Phase less affected by trail distortions Requires ≥ 2 samples Applicable to low & high speed meteors	Less accurate with weak echoes	$0.5 \rightarrow 5\%$
High precision Provides additional information (e.g. fragmentation, wind, diffusion)	Requires high sample rate	$<1\%$
High precision Gives terminal deceleration Gives meteor angle to beam	Requires high sample rate	$<1\%$
Determines velocity	Multi-station technique	3%

5.3.1.4 Meteor radiant

Intimately coupled with meteor speed or velocity study is meteor radiant investigation. This is because the orbits of interplanetary particles can be ascertained from the determination of meteor radiant and velocity [*Morton & Jones*, 1982; *Poole & Roux*, 1989]. The establishment of the orbits of meteor streams is a key component in tracing the overall evolution of the Solar system through the ages. While this is the primary motivation for radiant studies in general, in the current study, if the radiant of a shower is well established, it can be utilised to select or filter meteor events of interest. We will briefly discuss the radiant determination methods applicable to radar meteor observations in general with a view to substantiate those most appropriate for implementation in this case.

The first two methods utilise narrow and omnidirectional beams respectively and do not require the direct location of the meteor reflection point. A coordinate transform technique based on reflection point geometry is then described utilising the individually obtained echo point characteristics which allows two methods of data display. More complex methods, applicable to multi-station systems, are then briefly touched upon.

The majority of techniques described are directly applicable to single station radar systems and rely primarily on the detection of significant numbers of meteors to statistically isolate the shower radiant from the sporadic background. The later described techniques are capable of determining individual meteor orbits but require the more complex multi-station arrangements. Most techniques described utilise the specular reflection condition that provides radar echoes when the beam bore sight is directed at right angles to the meteor trail and thus are not appropriate for down-the-beam or head echoes.

An extensively used method to determine radiants is that of *Clegg* [1948] (also described in [*Lovell*, 1954] and [*McKinley*, 1961]). A narrow beam is directed at a selected azimuth and elevation. Due to the specular reflection condition, meteors with a radiant contained in a great circle orthogonal to the beam direction will be detected.

An increase in echo rate will be observed as the radiant satisfies this configuration and the time of maximum echo rate enables the determination of the right ascension of the radiant. The declination is determined by rotating the beam in azimuth and again observing the increase in echo rate indicative of the shower under investigation. An improvement to this method was attained by restricting the height range of echoes [*Keay*, 1957] and later the speeds [*Cervera*, 1996]. A more general method includes the radar's response function and is described by [*Elford et al.*, 1994]. An advantage of using a narrow beam in this technique is that it restricts return from additional nearby active radiants which can assist in isolating the radiant of interest. Unfortunately this requires prior knowledge of the approximate position of the radiant in order to direct the beam effectively and thus limits the technique's applicability in the detection of unknown or unexpected showers. Also, the detection of weak or simultaneous showers without application of the further filtering techniques described is difficult. It should also be noted that high levels of echo filtering require higher initial echo count rates, as in the case of *Keay* [1957], to allow firm conclusions to be drawn from the data.

A technique that utilises an omnidirectional beam is that of *McKinley & Millman* [1949*b*] and *McKinley* [1954]. In this method the angle of elevation of the radiant is derived from the meteor echo range distribution over the period the radiant is visible to the radar. The maximum elevation and time will yield the radiant coordinates. This technique requires a considerable, sustained echo rate of a distinct shower.

Interferometric radar systems are capable of a direct determination of the meteor echo reflection point and this information can be used to ascertain a radiant. In a coordinate transform method developed by *Elford* [1954] (appearing in *Weiss* [1955]) and *Jones & Morton* [1977], the reflection point information in terms of the celestial sphere is translated into polar coordinates whereby a shower radiant appears when meteor echo events lie along a straight line against the widely distributed sporadic background.

Elford [1954] applied the method to observations of the Geminid shower of 1952 and was able to determine a radiant from an average of about 36 meteors in total

(averaging about 20 shower meteors) per night over 4 nights. The simulated data example of *Jones & Morton* [1977] clearly shows three showers, comprising 100, 200 and 300 meteor trains, from a total of one thousand events using a similar method.

In terms of identifying the radiants of weaker showers using this method, only 10% of the total meteors generated in the simulated data facilitated an isolation of a radiant. While this is tempered against the near 50% requirement of the specific real data case of *Elford* it may be suggested that this technique has some application in isolating less distinct shower radiants. Similarly, the success of determining the Geminid radiant from a relatively small total sample indicates possible application to medium frequency meteor data. One disadvantage of this technique is that it is not usually possible to obtain any associated radiant structure information [*Poole & Roux*, 1989].

An extension of this coordinate transform technique results in the production of radiant *image* or *contour* maps [*Morton & Jones*, 1982; *Jones & Morton*, 1982; *Jones*, 1983; *Poole & Roux*, 1989] that may define the radiants and their associated local structure. Here a single meteor reflection point translates to a source radiant contained anywhere on a great circle perpendicular to this point. Each radiant on this great circle is interpreted as equally likely to be responsible for an individual reflection point and only when an ensemble of reflection points are translated to great circles, thus producing the *image*, does radiant structure form.

A concern with this technique noted by most researchers is the astigmatism in the resulting images caused by an antenna system covering only a limited region of the sky. *Poole & Roux* [1989] demonstrated an improvement in the radiant images formed using the Grahamstown all-sky meteor radar system [*Poole*, 1988]. However, the astigmatism was not completely eradicated. Recent research [*Hocking et al.*, 2001], using a different all-sky system, illustrates typical sporadic and shower maps without noticeable astigmatism. As these distortions are eliminated via improvements in the transmission and reception hardware, in concert with improvements in meteor echo processing algorithms (and hence increase in usable echoes), it is surmised that greater

validity will be attributed to the structure accompanying the distinct shower radiants revealed by this technique.

A concern that affects both implementations of the coordinate transform method is the selection of valid radiants from the background structure. At present this is often achieved by "eye". This may prove unsatisfactory as more complex structure is revealed in the radiant plots or images, and a more rigorous method may need to be trialled (e.g. *Jones* [1977]).

Aside from locating unknown radiants or confirming radiants, the above transform methods can be used in reverse to identify likely meteors originating from a particular radiant of interest. If the coordinates of a shower have been established previously they may be applied to data collected over the projected appearance of the shower in order to separate shower from non-shower meteors. Such an process has been described by *Hocking* [2000] where meteors were rejected if their great circle did not pass close to the known Geminids radiant. He notes that this technique does not of course remove sporadic meteors that have a great circle that passes close to the Geminids great circle. A similar approach is possible using the technique of *Elford* [1954].

While single-station techniques facilitate the extraction of mean meteor radiants from an ensemble of meteor observations, multi-station techniques allow orbits of individual particles to be calculated due to the trajectory information available. Historically, the first radiant determination was made using a three station system in 1945 [*Hey & Stewart*, 1946; *Hey & Stewart*, 1947]. The antenna patterns of each station were directed at a common region and the echo rates obtained from each station were used to deduce the radiant. Later work by *McKinley & Millman* [1949*a*] deduced meteor radiant via triangulation of ranges of head echoes (using three stations) with velocity also being calculated.

A more widely implemented multi-station technique is that of *Gill & Davies* [1956]. This approach uses the difference in t_0 of an echo observed by three stations to obtain the direction cosines of the meteor path. Initially the velocity was deduced from the Fresnel oscillations present in any of the echoes although other techniques are equally

applicable.

A recent example of a multi-station system designed to obtain meteoroid orbits is the Advanced Meteor Orbit Radar described by *Baggaley et al.* [1994]. Here the timing differences in the diffraction echo time series reveal the meteoroid trajectory and the velocity is determined by the time interval method, as described in section 5.3.1.3. A major disadvantage in the multi-station systems are their inherent complexity including the necessary duplication of equipment at the spaced receiving sites and the communication systems required between them.

The availability of the meteor reflection point information due to the application of the interferometry technique described in section 6.3.2 and the relatively wide beam width of the MF radar in comparison to narrow beam VHF meteor systems indicated that the echo coordinate transform technique was most suited to the data collected in this study. A more detailed review of the technique of *Elford* [1954] and *Weiss* [1955] is given in section 6.3.4 and its application to data obtained using the MF radar is discussed in Chapter 7.

Chapter 6

Experimental techniques

The data presented and discussed in the next chapter were collected and processed utilising various techniques. This chapter discusses the techniques employed and illustrates their use via selected examples. First, the experimental configuration of the radar system for the current meteor work is discussed in the context of other radar systems used for meteor observations. Secondly, suitable software was required to analyse the data, and the development and implementation of this software is outlined. A specific problem encountered during this development was the limited processing memory available for meteor data. This was resolved and the solution is detailed here with a view to future applications elsewhere. Finally, a variety of techniques to determine intrinsic meteor parameters (e.g. echo angle-of-arrival, meteoroid speed and meteor radiant) were summarised in section 5.3.1, and the specific implementation of the most appropriate technique in each case is detailed below.

6.1 Equipment configuration

The Buckland Park MF radar, originally designed for ionospheric studies, requires specific configuration for meteor studies. In this secondary role, the radar requires hardware and software to be tailored to meet the particular meteor research goals. This process is described in the following section.

6.1.1 Radars for meteoroid detection

The Buckland Park MF radar while not specifically designed for meteor studies has significant capabilities in this area of research. This capability is best explained by placing this atmospheric radar system in the context of those radars used for meteoroid detection in general.

Radar systems are best described in terms of their primary design purpose. In this context, radar systems used for meteoroid detection can be classified into three groups; dedicated meteor radars, atmospheric sensing radars and surveillance radars. Meteor radars are those systems focusing on the detection and interpretation of meteor echoes for intrinsic meteoroid or meteor parameters, winds or astronomical properties (e.g. orbit etc.). This most often incorporates the exploitation of the Fresnel oscillations of a meteor echo transverse to the radar beam. Atmospheric sensing radars on the other hand are designed to study a wide range of atmospheric phenomena as their primary focus, including atmospheric/ionospheric dynamics, winds and the ionospheric environment. However, since their height coverage overlaps the radar meteor region (70-160 km) in whole or part, it is often possible to apply these radars to meteor study. Radars in this atmospheric sensing group comprise MST/ST radars, atmospheric radars, Incoherent Scatter Radar (ISR)/Thermal scatter radars and digital ionosondes. Radars in this group can also be distinguished by their frequency of operation as MST/ST (VHF), atmospheric (MF/HF), Thermal/ISR (UHF) and digital ionosondes (HF). Surveillance radars are designed to detect particular air, land, sea or space targets. In the process of accomplishing this task, their electromagnetic radiation sometimes traverses the meteor region and offers another approach to meteoroid study. A major radar type in this group is the Over-the-Horizon Radar (OTHR) operating in the HF region. This classification scheme is illustrated in Table 6.1.

Radar System	**Type**	**Band**	**Purpose**	**Mode**	**Examples**
Meteor					
	General	VHF	intrinsic meteor meteor winds meteoroid orbit	CW, pulsed mono-, bi-static	*Robertson et al.* [1953] *McKinley* [1961] *Roper* [1984]
	Modern orbit	HF	meteoroid orbit intrinsic meteor	pulsed	*Baggaley et al.* [1994]
	Current generation	HF/VHF	intrinsic meteor meteor winds	pulsed	*Hocking et al.* [2001] *Holdsworth & Reid* [2002]
Atmospheric Sensing					
	MST/ST	VHF	atmospheric dynamics winds	pulsed	*Nakamura et al.* [1991] *Valentic et. al.* [1996]
	Atmospheric	MF/HF	atmospheric dynamics winds	pulsed	*Tsutsumi et al.* [1999] *Meek & Manson* [1990]
		HF	ionospheric dynamics	pulsed	*Hall et. al.* [1997]
	ISR	UHF	ionospheric dynamics		*Zhou et al.* [1995]
	Digital ionosondes	MF/HF	ionospheric environment	pulsed	*MacDougall & Li* [2001]
Surveillance					
	OTHR	HF	air, land, sea targets	CW, FMCW, pulsed, bi-static	*Thomas & Netherway* [1989]

Table 6.1: Radar systems for meteor detection. Radars are divided into three groups according to their primary design purpose; dedicated meteor, atmospheric sensing or surveillance radars. Atmospheric sensing and surveillance radars can be adapted from their primary design purpose for meteor observation. General examples are given for the main types of radars.

Conventional meteor radar systems typically operate in the 30 to 60 MHz range in order to avoid ionospheric back-scatter yet optimise the signal to noise ratio of the meteor echo. Radar beam power is optimised in the 30 to 60° altitude angle range using a variety of different polar patterns (e.g. narrow, fan-shaped etc.). Different configurations have been employed through the years of observation. During the 1950's a CW/pulse system was operated at Adelaide [*Robertson et al.*, 1953], although it suffered the disadvantage of a large spacing between transmitter and receiver sites. Pulsed radars have been used since the 1950's for collecting meteor rates and for determining radiants of showers using narrow beams of low elevation. With the addition of a simple interferometer the angle-of-arrival of the signal and hence the height of the meteor trail can be determined. With the addition of phase coherent transmission and detection the motion of the trail due to winds can be determined. These and other early radar systems are summarised by *McKinley* [1961]. The requirements of meteor wind radars are similar and are discussed by *Roper* [1984].

More recently, an example of a sophisticated meteor orbit radar, the Advanced Meteor Orbit Radar (AMOR) [*Baggaley et al.*, 1994] was developed in the 1990's at Birdlings Flat, New Zealand and provides routine measurements of the heliocentric orbits of Earth-intersecting meteoroids and also a small contribution of interstellar meteoroids. In contrast to this complex, distributed radar system, latest generation meteor radar systems have evolved into compact mono-static pulsed interferometric systems (e.g. SKiYMET (all SKY interferometric METeor radar) [*Hocking et al.*, 2001] and MDR (Meteor Detection Radar) [*Holdsworth & Reid*, 2002]), although they currently have not been used to determine meteoroid orbits.

The increasing use of atmospheric sensing radars for meteor work over the past 25 years is a result of a desire to gain maximum scientific benefit from established radar systems. This has been aided by the increases in computational power for algorithm automation and the flexibility of operation included in many standard atmospheric sensing radar designs.

A significant difference between dedicated meteor radar systems and atmospheric sensing radars is that the latter often projects radiation vertically, which is less desirable for meteor detection. In this case, *Nakamura et al.* [1991] showed the importance of beam side-lobes in meteor studies. This less effective approach is alleviated to some degree in some cases by the provision of beam steering facilities, to more closely duplicate the off-zenith beam configuration of a dedicated meteor system.

The proliferation of MST/ST radars (pulsed Doppler radars operating in the VHF-UHF frequency range) through the 1980's and beyond has facilitated considerable meteor research as these radars have been adapted for a meteor observation role (see e.g. *Avery et al.* [1983]; *Avery* [1985], *Elford* [2001*a*]). In this context *Elford* [2001*a*] has noted that response functions of these radars imply the smallest collecting area and highest sensitivity of any VHF meteor radar built.

MST radars may be used for meteor detection in their original form or with some level of adaption. Various approaches to adapting the MST radar for meteor work have been implemented. This has included reconfiguring existing hardware (e.g. antennas) or adding additional hardware (e.g. interferometer arrays or supplementary meteor receiving systems). As an example, the Middle and Upper atmosphere (MU) radar [*Nakamura et al.*, 1991] provided for the configuration of an interferometer for meteor work from existing antenna array elements. Later, an interferometer external to the MU array was used with meteor detection hardware attached to existing receiver components [*Nakamura et al.*, 1997]. Alternatively, a common method of obtaining meteor observations from existing MST radars is through an addition to the radar receiving hardware, comprising a single purpose meteor detection computer that operates in parallel to the normal MST radar duties (a configuration termed "piggy-back" by *Hocking* [1997*a*]). Examples of such systems are the Adelaide meteor system attached to the VHF ST radar (e.g. *Badger* [2002]) or the Meteor Echo Detection And Collection (MEDAC) system (e.g. *Wang et al.* [1988]; *Avery et al.* [1990]; *Valentic, Avery & Avery* [1996]; *Valentic, Avery, Avery, Cervera, Elford, Vincent & Reid* [1996]). These systems do not require additional receiving arrays and can be easily

retro-fitted to many ST/MST radars.

Atmospheric radars operate in the MF and HF regions and primarily focus on atmospheric dynamics and wind measurement, often using the Spaced Antenna (SA) measurement technique. Such radar systems may be compact [*Lesicar*, 1993] or large and distributed, such as the Buckland Park MF radar used in this study. A wider beam width than MST systems, often directed vertically, is a characteristic of these systems. To alleviate some system deficiencies in Angle-of-Arrival (AoA) measurements deduced from the compact spaced antenna arrangement often used, external interferometers have been co-located with existing equipment [*Meek & Manson*, 1990]. As with the MST radar systems, the potential exists for additional hardware to be added to atmospheric radars in the fashion of the Adelaide VHF ST or MEDAC systems for meteor observations.

Another class of atmospheric radar capable of meteor observations are the HF radars of the Super Dual Auroral Radar Network (SuperDARN) (e.g. *Hall et al.* [1997]; *Jenkins & Jarvis* [1999]). The radars comprising this network were designed to study the convective patterns in the high-latitude ionosphere but consistently observe meteor echoes at shorter ranges than their primary target.

Thermal or incoherent scatter radars (see section 5.1.1) have also been utilised for meteor research (e.g. *Pellinen-Wannberg & Wannberg* [1994]; *Zhou et al.* [1995]; *Mathews et al.* [1997]). This type of radar operates in the UHF region of the electromagnetic spectrum and primarily examines ionospheric phenomena and dynamics. Re-configuration of this type of radar for meteor observations is less demanding and often only involves a modification of data collection parameters.

Ionosondes, used mostly for ionospheric environment investigation (including radio propagation studies) and operating in the HF region, have also been considered for adaption for meteor observations [*Poole*, 1988]. Modern, digital ionosondes are particularly suited to this task with their interferometric capabilities (e.g. *Berkey & Fish* [2000]; *MacDougall & Li* [2001]).

Surveillance radars have been less frequently applied to meteor observations due to

their human-made target focus of ships, aircraft land or space vehicles. However the OTHR type has demanded significant research on ionospheric dynamics to accomplish this task and it is this aspect of its operation that has encompassed meteor studies (e.g. *Thomas & Netherway* [1989]). Another type of surveillance radar that has been employed for meteor observations is the VHF/UHF Advanced Research Projects Agency Long-Range Tracking and Instrumentation Radar (ALTAIR) [*Close et al.*, 2002], which is designed primarily for space surveillance but can be used as a highly capable meteor radar. In terms of configuring these types of radar for meteor research, due to their dedicated design purpose, generally no hardware modifications are implemented but rather data collection parameters are re-configured for meteor observation.

One reason for highlighting the position of the Buckland Park MF radar in the context of radars used for meteoroid study is that in the research described here the radar's meteor capabilities are exploited for meteor shower observations while its atmospheric sensing capabilities are used for system calibration. This calibration process is described in detail in section 6.3.1. This dual use capability of the radar has some limitations also, and these are described below.

6.1.2 Radar configuration for meteor shower detection

The Buckland Park MF radar used in this study can be configured in a variety of ways for meteor detection purposes. This is due to the flexibility of the system manifest as accessability to the large number of individual elements in the array, options for a single transmitter or multiple transmitters operated in parallel, an adaptable receiving system and capability to steer the transmitted beam. The configuration of this radar system for a specific meteor study is now described.

The intention of this project was to examine how a meteor shower could be detected at medium frequency and to determine meteoroid speeds using the Fresnel diffraction behaviour inherent in the amplitude and phase time series of the radar data. As touched upon in section 5.3.1.4, there are numerous techniques to isolate a meteor

shower in radar data, such as using two fixed beam directions to detect the shower at different times, or tracking the radiant through its motion using beam-steering capable radars. The radar's beam steering capability was restored as a result of the work described in Chapter 2 and in order to enhance the meteor echo rate from weak meteor showers using the BP radar, tracking the shower radiant was determined to be the most effective observational technique.

The primary requirement to achieve intense Fresnel scattering from a meteor trail is to illuminate it with radio waves perpendicular to its path. For meteor showers this requires the radar beam to be steered at an angle orthogonal to the radiant direction. In order to effectively track the meteor shower radiant its position was calculated every 30 minutes over a period of seven hours while the radiant was above the horizon. During each of these thirty minute periods changes in radiant azimuth typically ranged from 4.4 to 9.1°, while changes in the zenith angle ranged from 5.5 to 1.3°. Because the beam width is approximately 10°, the radiant position could be effectively tracked by incrementing the beam direction to the new position at the end of this period. This would ensure significant power contained within the main lobe was being utilised for shower meteor detection.

A concern with this configuration for meteor observations was the effect a finite beam width has on the Fresnel diffraction of the meteor echo. This was investigated further. Because the echo signal at any instant is the summation of the scattering from all the elements of the trail, modified by the response of the radar antenna, it is possible the array polar diagram will significantly modify the echo amplitude and phase from that expected. This has a direct implication for the determination of meteoroid speeds via the Fresnel phase time technique described in section 5.3.1.3 and applied to the data collected. Recent modelling of the antenna aperture's effect on echo Fresnel diffraction by *Elford* [2003*a*] indicates that the polar diagram used in this study has essentially no effect on the amplitude or phase series. Thus standard meteor echo Fresnel diffraction models may be applied to the data where necessary.

As an example of shower tracking, the radiant position for the Orionids shower

is right ascension (RA or α) = 95° and declination (δ) = +16° (see Table 7.1 on page 352). These coordinates have been used to calculate the beam directions required to detect the Orionids shower on 22 October 2000, which are displayed in Table 6.2. Note that the directions have been corrected for the array alignment for true north.

CST [hrs:min]	**Radiant Azimuth** [deg:min]	**Radiant Altitude** [deg:min]	**Radar Azimuth** [°]	**Radar Zenith** [°]	**Start Range** [km]	**End Range** [km]
23:00	73:19	-3.12	0.0	0.0	80	212
23:30	69:04	2:08	252.8	2.1	80	212
00:00	64:36	7:38	248.4	7.6	80	212
00:30	59:47	13:03	243.6	13.1	82	214
01:00	54:35	18:14	238.4	18.2	84	218
01:30	48:51	23:05	232.7	23.1	86	220
02:00	42:32	27:31	226.3	27.5	90	222
02:30	35:33	31:24	219.4	31.4	92	224
03:00	27:50	34:39	211.6	34.7	96	228
03:30	19:28	37:08	203.2	37.1	100	232
04:00	10:31	38:45	194.3	38.8	102	234
04:30	1:15	39:23	185.0	39.4	102	234
05:00	351:56	39:00	175.7	39.0	102	234
05:30	342:52	37:39	166.6	37.7	100	232

Table 6.2: Radar beam directions for transverse detection of meteors from the Orionids 2000 shower event. Note that radar azimuth has been corrected for array alignment.

The antenna groups used for transmission and the resulting polar diagram have been illustrated previously in section 2.2.1.

Increasing the power transmitted has a positive effect on the number of meteors detected, so it is preferable to transmit using all available power modules. As described in section 2.2.2, the transmitting system consists of three independent transmitter chassis that can be operated singly for lower power applications or in parallel for higher power applications. Theoretically, any combination of the three transmitters could be configured for a particular experiment. However due to the significant fault isolated in transmitter three (see section 2.3.3) at the time of the observable meteor showers, this transmitter chassis was excluded from the system for meteor data collection. This allowed maintenance work and solution evaluation to continue while the two, fault

free, transmitters were employed for the Orionids observations.

For reception, a five element interferometer was configured from available dipoles of the complete array. Due to limited element availability, dipoles orthogonal (east-west aligned) to those used for transmission (north-south aligned) were employed for these reception duties. Such an arrangement is generally not preferred but was unavoidable in this situation. In ideal atmospheric conditions, such that there are no path altering effects influencing the signal transmitted, reception of the transmitted signal on like polarised antennas is preferred in order to maximise the signal recorded. However, in the experimental configuration employed here, the use of orthogonally aligned antennas for reception has the potential to substantially reduce the signal recorded and this situation is discussed briefly.

2 MHz signals scattered from meteor trails are significantly affected by the ionisation in the D and E regions through which the radar signals propagate. In general linearly polarised signals will become decomposed into ordinary and extraordinary waves that will suffer differing amounts of retardation and absorption. In extreme cases, such as in day-time, the transmitted pulse will be returned as two elliptically polarised pulses separated in time. Further, one pulse is usually much weaker than the other. Even at night, the ordinary wave dominates so that the received signal will be elliptically polarized (see *Steel & Elford* [1991]). In addition, 2 MHz radar signals from meteor trails will travel through varying amounts of ionisation depending on the position of the trail, and the polarisations of the received signals will be essentially random. Thus it is unnecessary for the receiving antennas to have the same polarisation as the transmitted signal. This fortuitous feature is exploited in the layout of the receiving antenna interferometer. This interferometer configuration is more thoroughly discussed in section 6.3.2.

Alternate radar configurations for meteor detection using this and other MF/HF radars were investigated and these are discussed in Appendix J. However, the configuration described above offers the advantage that most beam power is used for detection of meteoroids having the expected shower trajectories. This is in contrast to the less

effective, vertically directed radiation of many atmospheric spaced antenna, ISR and ionosonde systems. Limitations of the interferometer configuration used for reception are discussed in section 6.3.2.

6.1.3 Meteor data collection parameters

Data collection time

Since a meteor shower was the focus of this study, observations were conducted over the period the shower radiant was visible above the horizon. A further constraint that limited shower observation time is the rapid build-up of ionisation in the upper atmosphere that occurs as the Sun's radiation impacts at heights of ∼100 km. This ionisation build-up begins approximately thirty minutes before the time of ground sunrise and tapers off after sunset. Medium frequency radiation is refracted from this ionisation and thus limits meteor observations to the night-time. Data were collected over the nominal time of 23:00 to 06:00. This total collection time encompasses a small period initially where the radiant was not visible above the horizon and approximately twenty minutes at the end where the effects of ionospheric layering between 100 and 120 km begin to influence signal propagation. Of those possible meteor events still visible within this period, not all were confirmed as meteoric in origin due to their significant merging with, or contamination from, this layering phenomenon. Specific layering events occurring during these periods often exhibited characteristics closely related to the expected meteor event. An example of this is where transmitted radiation is retarded by a layer of ionisation. This and other phenomena have been observed by other reseachers [*Olsson-Steel & Elford*, 1987; *Elford & Olsson-Steel*, 1988]. This affected data was later excluded from analysis and is further discussed in Chapter 7.

Choice of PRF

Prior to this work, meteor research at the Buckland Park site conducted during 1997 had employed non-optimum data collection parameters [*Tsutsumi et al.*, 1999]. These

researchers suggested improvements to a number of data collection parameters in order to achieve better experimental results in the future. This earlier work suggested that a significant number of meteor events existed at ranges greater than 148 km. In this current study the maximum sampling range was thus extended to over 200 km. More important was the selection of a suitable sampling frequency. This earlier night time study had used a PRF of 16 Hz and coherently integrated the data four times, resulting in a sampling frequency of 4 Hz. This PRF choice limited the maximum height of detected echoes because short lived echoes at greater heights were undersampled (due to the large ambipolar diffusion coefficient and thus rapid expansion of the trail). A further disadvantage brought about by the low sampling frequency was the inability to determine meteoroid speed due to an inadequate sampling of the variation with time of phase prior to the meteoroid crossing the orthogonal point.

An increase in sampling frequency was sought to address these concerns. Theoretical equipment capabilities [*Reid et al.*, 1995] suggest PRFs up to 200 Hz are available for individual experiments, however as noted earlier (see section 2.3.1.2), practical hardware considerations limit this to an upper bound of about 100 Hz. While an estimate of an optimum PRF can be attained from simple modelling of the meteor phase for a range of radar PRFs it was discovered that the upper atmospheric environment significantly influenced the final choice of PRF, which is less easily modelled at the outset. This demanded extensive data collection with preliminary observational parameters in order to select an appropriate PRF. Data was collected with a PRF of 100, 60 and 20 Hz. Significant range aliasing of data was apparent in the 100 Hz data, while data collected at a PRF of 20 Hz did not have sufficient samples of a meteor echo for a speed determination. Because it is surmised that significant structure existing at more distant range gates is responsible for the range aliased signal, PRFs higher than 60 Hz may only be appropriate on ionospherically "quiet" nights.

The total number of samples of the meteor event was still quite low in most cases and offered no opportunity for coherent integration to improve signal-to-noise ratio

(without averaging over necessary detail). In addition to this consideration, *Olsson-Steel & Elford* [1987] point out that coherent averaging of the data in a similar situation was not possible at meteor heights because the drift velocities are of the order of 100 ms^{-1} which lead to phase changes of about 10° between samples.

Parameter	**Specification**
Campaign name	Orionids 2000
Date	20^{th} to 24^{th} October
Time active	23:00 to 6:00
RMS PEP	46 kW
Power aperture product	1.5×10^8 W m^{-2}
Pulse width (3 dB)	20 μs
Average power	55.2 W
PRF	60 Hz
Number of points	3500
Coherent integration	None
Start range	Beam angle dependent (80 to 102 km)
Sampling interval	2 km
Number of heights	66
Coding	Not active
Polarization	Linear
Pulse width	∼20 μs
Receivers	5
Beam sequence	see Table 6.2
Gain control	Not active
Data set size	4622368 bytes

Table 6.3: Experimental parameters for the Orionids 2000 campaign.

Number of samples

Ideally, the more samples that describe each individual meteor series, the more successful the application of subsequent data reduction techniques. To this end a near maximum number of total samples was specified per data set in the context of other important considerations. As discussed previously (see section 2.3.6), hardware and software limits, together with data transfer issues, limited the maximum number of samples specified per data set. In the case of the Orionids 2000 data this resulted

in 58.3 second time series (termed an "acquisition"), initiated every 160 seconds (resulting in 101.7 seconds down-time/data transfer). Because of the long duration of some meteor events at this radar frequency, it is therefore expected that a notable number of events will be truncated (cut-off) in the time series. Practically this is not a significant concern as meteoroid speed can regularly be determined from the phase preceding this cut-off point. While the primary aim of having a suitable number of samples per meteor event for speed reduction was achieved, the eradication of the highlighted system hardware and software concerns will enable time series length to be increased in the future.

6.2 Software development & application to meteor events

The development of appropriate software for the analysis of 2 MHz echoes formed a significant part of this research and the major issues encountered during this development are discussed in the following section. It was found that existing software for meteor analysis did not fulfil the perceived requirements for MF meteor observations, and other meteor analysis software now being implemented with meteor radar systems differed from the traditional types used. This led to the development of a prototype software for meteor and other analyses. The design of the software and solutions to specific problems encountered in the development process are detailed. An overview of data processing is also made.

6.2.1 Software overview

The data archived on CD-ROM contained multiple acquisitions, comprising five channels of times-series (in-phase and quadrature components) sampled every 0.0167 seconds. To enable the archived data to be analysed for meteor events, and meaningful

parameters deduced, suitable software was required. At the outset, two software packages were available for application to the data; a commercial time series Analysis and Display Suite (ADS) and an in-house Meteor Analysis Suite (MAS) developed by the Atmospheric Research Group. Both software packages were developed for specific and differing requirements. The ADS package was primarily designed for the analysis and display of routine observational data. To effect this, the software was optimised for moderate sized data sets from a limited number of receivers. When applied to the collected meteor data a number of deficiencies were highlighted. Primarily, the software suite was unable to process the large size single meteor acquisitions at sufficient speed for rudimentary display on a personal computer or workstation. This severely hampered the manual meteor detection process described later. Secondly, the Graphical User Interface (GUI) was not optimised for viewing meteor events. This inability to view effectively the meteor data combined with the processing speed issues precluded further development of this software for specialised meteor data processing. In contrast to this, the MAS offered excellent display and analysis of meteor events but did not have an integrated detection component and required manual manipulation for data reduction of each meteor event (i.e. intensive manual off-line analysis). Also, this software was optimised for VHF radar meteor events in an uncluttered environment, while the ionospheric environment characteristic of MF meteor events was less than ideal in this respect. Although this software package could incorporate new analysis modules there were no plans to automate it in the near future. With neither of the existing software packages catering specifically for the current meteor processing needs, an alternate approach was sought.

A survey of current analysis procedures for meteor data revealed a transition from traditional manual off-line analysis [*Cervera & Reid*, 1995; *Tsutsumi et al.*, 1999; *Reddi et al.*, 2002] to that of a fully automated near real-time approach [*Hocking*, 2000; *Hocking et al.*, 2001; *Holdsworth & Reid*, 2002]. In fact a general trend in radar data processing is toward near real-time on-line analysis [*Hocking*, 1997*a*; *Hocking*, 1997*b*]. This transition to automated analysis is a direct consequence of the increase

in computational power afforded by the current generation of personal computers and the algorithmic nature of many types of analyses, particularly meteor analysis. It is in this climate that the requirements for the prototype analysis software for the MF meteor data were developed. Paramount among these requirements was the aim that full automation of all meteor analysis would be implemented at some future date.

Fully automated analysis was primarily motivated from the perspective that an experiment dataset could be quickly and easily automatically re-processed at any stage with alternate analysis algorithms. For instance, alternate velocity algorithms could be implemented in parallel or specific algorithms could be modified or refined based on new research. It was felt that the time consuming manual analysis previously implemented did not incorporate this flexability.

Specific software requirements encompassed a number of areas and these are summarised below.

- Applicablility for near real-time meteor analysis.
- Desire to interact with data at various points in the processing/analysis.
- Data display to cater specifically for meteor research (i.e. time series of amplitude, phase, unwrapped phase, power, signal-to-noise level, receiver phase differences, etc. (e.g. *Nakamura et al.* [1991]; *Tsutsumi et al.* [1999]).
- Ability to later automate aspects of meteor analysis that is initially implemented manually (e.g. meteor detection).
- Options to calculate meteor parameters (e.g. AoA, velocity) manually or automatically.
- Easily expanded or updated (e.g. algorithms, display etc.).
- Basic structure applicable to other analyses in module form.
- Ability to run on moderately specified workstations and personal computers.

In order to best fulfil the requirements of the proposed software outlined above, two primary design approaches were evaluated [*Sommerville*, 1996; *Pressman*, 1997]. The first, "structured or functional" design, is often appropriate for systems where a number of functions are performed on data in a sequential fashion and is thus appropriate for instances where the functionality is more likely to change than the data itself. In contrast to this, the "object orientated" design approach is appropriate for combinations of routines and data and is particularly appropriate for situations in which the data is more likely to change than the functionality. Models of the required system were outlined using both of these approaches and it was apparent that the structured approach would best suit the current needs of the project. A determining factor was that this particular design approach would also best suit other proposed analyses for atmospheric research such as winds via Full Correlation Analysis (FCA) or Time Domain Interferometry (TDI) analyses which may be required for comparison to meteor derived winds at a later time, as well as the calculation of system phase errors described in section 6.3.1.

To further facilitate the software requirements at a lower level, extensive use of modules and routines were included in the design process. The benefits of using modular approach in these terms enables individual analysis algorithms and processes to be conveniently packaged for use and re-use throughout the programme.

An example of the direct benefits of using software modules concerned the meteor detection process. Manual meteor detection was preferred at this juncture for a number of reasons. Firstly, the complex ionospheric environment in which the meteors are detected at a radar frequency of 2 MHz often requires a different approach to that of VHF detection algorithms. Secondly, the meteor count rate was expected to be relatively low and hence managable as a manual process and thirdly, initial extensive manual interaction with the data would assist in the design of an automated detection algorithm at a future time. The meteor detection process was thus separated into a module within the overall programme design. It was envisaged that the output of this module would contain a log of all detected meteors within the acquisition and their

individual characteristics relevant to later processing. In this way the meteor detection could be manually undertaken and detection module output generated in the form of a small file for subsequent processing.

Another instance of the strength of modular type software design was that of being able to be incrementally upgraded various software modules. Specific requirements for radar data processing are often difficult to establish at the outset in some applications. The very process of examining the data collected narrows the most appropriate approach to be taken at particular data processing stages. The design must therefore be able to incorporate these procedures in concert with highly specified algorithms such as that for angle-of-arrival or meteoroid speed. The use of software modules allows for a more seemless upgrading process as internal module design may vary while the module interface remains static. Established coding standards were adhered to where possible throughout software construction [*McConnell*, 1993].

The prototype software suite produced was called *develop* and was implemented in Interactive Data Language (IDL) in a Linux environment. IDL is ideal for prototyping software because of its inherent high level of abstraction, extensive choice of library modules and its strong data visualization capabilities. It should be noted however that a meteor detection system implemented on a fully optimised meteor radar system is likely to be subject to a high rate of meteor events. Thus the speed and efficiency of the software is of primary importance. This may be achieved in an optimised IDL code but is more likely to be achieved using *C* or a similar low to medium level language, once the programme design and content has been stabilised.

A particular problem encountered with existing software, as indicated previously, concerned the extensive time required to process and display data on personal computers. The use of significant virtual memory to form large data arrays was traced as the cause of the unacceptable processing time increases. This situation needed to be addressed as the size of the data set collected for the observations described in Chapter 7 was artifically low, due primarily to equipment limitations causing slow data transfer times and limited number of samples per acquisition. Once these issues were

resolved, meteor data set sizes were likely to increase significantly in order to optimise meteor detection and analysis. Another potential source of large sized data sets, distinct from the meteor observations described here, is a demand for winds deduced from atmospheric observations via spaced antenna analysis. These observations would take place at the same time as meteor observations and would utilise extra receivers (and thus more data streams) from the total of sixteen receivers available.

To cope with the current large size of the meteor data sets, PC RAM sizes could be increased, however this approach enters a cycle (more RAM for larger data arrays) best avoided. To address the analysis of large data sets, it was decided to limit the use of physical RAM to a level commensurate with current computer capacity for the immediate display functions, and utilise hard disk storage (virtual memory) for most large array storage. The decrease in speed due to utilising disk storage as programme memory was deemed acceptable in this instance, as vital, smaller sized, data arrays for display were still retained in RAM.

The procedure by which this approach was implemented was via a modified version of a *data channel* system [*Woithe*, 1999, private communication]. In this system all data within the software is arranged in so-called *data channels*. Each data channel is a general structure and may contain any type of data within it. It also contains additional information that describes the data in that channel. Thus one data channel is a repository for one type of data such as a receiver time series or amplitude series, with range, byte size, sampling frequency etc. information appended. Crucially, the data channels may reside in physical memory or on hard disk, and can thus be manipulated to minimise the physical memory taken at any one time and so the software is ultimately limited by disk space and not necessarily the available physical RAM. Also, data channels may be created or deleted at various stages within the application to further minimise physical RAM useage. The interface to the data contained in these channels is via the flexable routine *get_data_by_description()*. This retrieves the specific data requested (i.e maybe a partial section of an amplitude series) from wherever it may reside. This arrangement separates the data storage from the *use* of

the data and thus allows the data storage to be managed independently of how one manipulates the data. Minor performance penalties incurred by utilising significant hard disk storage instead of physical RAM storage are offset by the ability to *conduct* the required analysis on a moderately specified computer. Thus a solution to processing large sized data sets on moderately specified PCs was developed and implemented that can be applied in other similar situations. The salient points of this system are summarised in the following list.

- Data channels may reside in physical memory RAM or on hard disk.
- Data channels are generic or general structures.
- Data channels contain only one type of data and its associated information.
- Data channels may be created or deleted at various stages to optimise available resources.
- The interface to data in channels is via a routine named *get_data_by_description()*.

The programme was designed to be used with a graphical user interface but only a text based interface is currently implemented. Programme output is in the form of a small sized file containing individual meteor event parameters. These files were used as input to post analysis software to form the distributions presented in the following chapter.

6.2.2 Data processing overview

To accurately ascertain trends in the data collected requires the subsequent processing to be free from any introduced artifacts. It is from this perspective that the data manipulation applied in this study is briefly outlined below. Specific stages of this manipulation cover the detection and quality control of selected meteor events.

The various steps in the data processing are outlined as follows: a) remove mean; b) manual detection; c) combine receiver time series; d) display amplitude, phase,

unwrapped phase, in-phase and quadrature; power and noise level and receiver phase differences to aid detection; e) obtain meteor event characteristics (start times, unaliased phase series etc.) and f) calculate required parameters (AoA, height, speed etc.).

The detection of meteor events in the data was undertaken manually by scrutinising each acquisition sequentially over the period encompassed by the data collected. Core parameters of the meteor events chosen for display were amplitude, phase and unwrapped phase for each available receiver and the combination of data from all receivers. The "combination of receiver data" is described in what follows.

Combination of data

Essentially, the technique used to combine individual receiver output to form one complex time series mirrors that of the post-set beam steering technique [*Woodman & Guillen*, 1974; *Röttger & Ierkic*, 1985]. After the system phase errors corrections had been applied to the data (as described in section 6.3.1) the data from all five receivers was combined. The combination of receiver time series has been applied to meteor data here to provide alternate amplitude and phase series in an effort to identify meteor events otherwise contaminated in their individual receiver series. Various approaches have been utilised to this end such as the incoherent addition of receive antennas in order to improve the ability to make an initial identification of a meteor [*Hocking et al.*, 1997]. In contrast to this, receiver combination has also been used to aid in data storage [*Nakamura et al.*, 1991].

However, as implemented, the combining of the receiver time series offered no significant benefit to meteor detection or later analysis in this data. No additional meteors were detected via the combined receiver time-series that had not been identified in individual receiver time series and the unwrapped phase of the combined receivers displayed better phase records than the individual receivers in very few instances. This result may not be that surprising when one considers that each spaced receiver is effectively "sampling" a different aspect of the meteor trail and any combination

of receiver information must account for this. Such a process is often non-trivial and may indicate that combining receiver data should be avoided, unless this and other considerations can be dealt with adequately.

In the future it may be of advantage to combine only those receivers with a meteor SNR exceeding a certain threshold and omitting low SNR receiver signals. In this study, only those receivers with the same range gate were combined. Due to the range oversampling of the meteor echo that occurs with this equipment the combination of high SNR receivers at non-coincident ranges may also be of value.

Recent meteor studies (e.g. *Holdsworth & Reid* [2002]) indicate an alternative processsing method. The phase differences between receiver pairs is estimated by the application of a cross correlation function and all available receivers are combined after removing these phase differences. This may offer better results and is earmarked for future implementation.

An extensive number of **meteor detection algorithms** have been developed over the span of meteor studies (for recent algorithims see e.g. *Valentic, Avery, Avery, Cervera, Elford, Vincent & Reid* [1996]; *Hocking & Thayaparan* [1997]; *Tsutsumi et al.* [1999]; *Hocking et al.* [2001]; *Holdsworth & Reid* [2002]). Primarily these algorithms focus on the amplitude or power signal exceeding a threshold SNR or noise level for a pre-determined duration followed by an exponential decay to signify the presence of a meteor-like event. These distinctive characteristics are typical of the underdense meteor type echo detected in the "orthogonal mode", and are the primary echo type of most meteor radars. However, in the current MF project, overdense meteors which do not exhibit this classic exponential decay were targeted as well. Thus more flexability in the search algorithm was needed. Also the underdense detection algorthim is less effective in the ionospheric environment as time series are often affected by varying ionospheric ionisation. This can obscure the initial stages of a meteor echo event or superimpose the meteor event on top of an existing ionospheric echo.

The manual detection process was divided into two parts or passes through the

data. The first part identified all *possible* meteor-like events, while the second, more detailed process, confirmed or denied the initial classification as a meteor by more stringent tests.

Because of the variability in meteor echo characteristics the manual detection requirements were less stringent in the first pass detection so as to encompass all possible meteor echoes including any overdense or possible down-the-beam meteor events.

Typically all receivers and combined amplitudes were scanned for fast rise time and longer fall time events. If potential events were identified, the raw phase was examined around the amplitude peak for characteristic meteor behaviour. The unwrapped phase was also examined for possible un-aliased phase behaviour typical of a meteor event although this was not a strict criterion for detection. Adjacent receivers were viewed and if the echo was present a meteor-like event was declared.

Following the accumulation of all meteor-like events in the acquisition block a second pass of the data was initiated to first confirm a meteor-like event as an actual meteor and secondly to determine its suitability for further AoA and speed analysis.

This second pass process involved establishing all relevant characteristics of the meteor-like event for comparison with expected meteor echo behaviour and then determining whether the specific characteristics of the the echo would be suitable for the AoA calculation (and hence height etc.) and the speed via the chosen technique. First, the range gates adjacent to the original detection range were searched for oversampling of the echo. Likewise all receivers were examined. This established the overall strength of the echo and also assisted in the search for down-the-beam echoes which are expected to have an extensive range gate span. Characteristics typical of meteor echoes were reduced from the echo event such as the time of event start, end, peak amplitude, start of unaliased unwrapped phase and the beginning and end of the linear phase section past the peak amplitude point. Failure to adequately establish these characteristics indicated the event could not be confirmed as a meteor. Additionally the beginning and end of the phase section attributed to upper atmospheric wind action on the trail was also noted.

The noise level in each receiver/height amplitude series was estimated by a modified version of the technique described by *Hildebrand & Sekhon* [1974]. This allowed an estimate of the SNR of the peak amplitude of the meteor event and thus establish the relative quality of each receiver/height record. Receivers containing the highest SNR range gate were then scrutinised for meteor like amplitude and phase behaviour. Failure to exhibit these fundamental theoretical characteristics precluded the event from classification as a meteor and from further processing.

As highlighted above, a meteor event could not be confirmed for a variety of reasons. Often an event was suspected to be a meteor but due to a poor SNR, important aspects of the amplitude or phase series were ill-defined. A low SNR also contributed to the inability to locate the start of a meteor amplitude series. This factor, coupled with the often low number of samples of the total event provided insufficient information from which to confirm expected meteor phase behaviour and other characteristics. Other reasons for the non-confirmation of a possible meteor event were due to the abnormal behaviour of one aspect of a meteor amplitude or phase series. For instance, the unwrapped phase or the raw phase may have exhibited no discernable phase minimum or a phase minimum significantly distorted by wind action.

The presence of ground clutter in the time series also masked regions of meteor echoes that precluded them for further analysis. This clutter typically extended over many range gates, maintaining a similar form in each. It may be possible to limit the effect of this type of clutter by further analysis in the frequency domain. Its removal via notching at its characteristic frequency may be an option. Time series that exhibit significant E-region ionisation, that serve to obscure meteor echoes, offer a much greater processing challenge.

To achieve the aims of the study it was necessary to impose further quality measures on the detected meteor event. To obtain meteor AoA, height and speed it was neccesary to require a linear phase region be present in the post amplitude peak region of the echo and for the pre-t_0 phase region to be suitable for speed calclulation via the Fresnel phase-time method (described in section 6.3.3).

Previous studies (e.g. *Cervera* [1996]) have noted that the most suitable region for stable phase in a meteor echo is the region post phase minimum where Fresnel oscillations have reduced. Receiver phase differences from this region were selected for input into the AoA algorithm described in section 6.3.2. If a meteor did not exhibit a suitable linear phase region, AoA and height could not be determined from the event, so it was rejected.

Also, if the requisite number of points were not present in the phase series or it departed significantly from expected theoretical characteristics the event was rejected as not suitable for speed analysis.

It should be noted in passing that the acceptance criteria is relatively strict. This was required to limit false meteor detections and to ensure all appropriate parameters could be determined from each event. It may arise that a single meteor event will provide AoA but not speed due to its varying phase series quality. This type of echo was detected infrequently, but may be included in a future implementation of the detection algorithm. Typically, if the pre-t_0 phase or the phase for AoA calculation was not available, the meteor event could not be confidently identified because of its overall borderline or poor quality in any case.

6.3 Specific techniques applied to data

From the various techniques described in Chapter 5 for meteor parameter reduction, specific methods were selected to be applied to the data collected. This section describes the application of some techniques to the data and illustrates typical examples. In the application of some techniques, such as the calculation of meteor AoA, additional data manipulation procedures were required to ensure the veracity of the derived angles. For instance the phase calibration of the receiving system is described as it relates to the AoA calculation.

6.3.1 System phase errors via atmospheric partial reflection

Whilst every effort has been made in establishing the radar equipment to ensure that the signal excited at each antenna at the same instant is recorded in its original form (see Chapters 2 and 3), inherent equipment variations between antenna and signal processor introduce unavoidable systematic errors into this recorded signal. It is important for these errors to be estimated and removed from the data before further data reduction is initiated, particularly if parameters derived are to be representative of the atmospheric phenomena under study. A vital parameter in this study is the angle-of-arrival derived from the phase information of spatially separated antennas and this section describes techniques applied to remove the error component of the phase. Due to the fact that AGC was not active during data collection and that the inherent gain of each receiver did not vary markedly over the observation periods, the amplitude of the signal is assumed to be representative of the atmospheric phenomenon probed and thus did not harbour significant systematic error.

Theoretically, the path from each antenna to the digitiser is identical. In this case, the phase of a signal excited at the antennas will incorporate no differential retardation of the signal in like signal paths. In practice there are in fact a number of sources of phase discrepancies that introduced errors into nominally identical systems that feed the signal processor. In order from antenna to receiver, the sources may be a) variation in antenna impedance, b) unequal electrical cable lengths and c) unequal receiver propagation delays. As discussed in Chapter 2 and 3, antenna impedances for fully functioning antennas display a variation of $\pm 15\ \Omega$ and $\angle \pm 15^\circ$ which will have some effect on the voltage (and hence phase) induced on the dipole. Table 3.9 on page 141 shows a variation of electrical length of approximately this magnitude and this is interpreted in part to be an indication of the level of cable length mismatch existing at any one time in the CBA sub-system. The delay of the signal through receivers not dissimilar to those used in this study has been examined by *Vandepeer* [1993] and indicates that there can be a measurable source of phase error introduced

to the system via this system component.

An estimate of the total system phase errors can be obtained by utilising one primary approach. Essentially a target or phase source, from which initial phase behaviour can be determined, is compared to that recorded by the digitisers. Deviations from the expected phase behaviour indicate the presence of systematic bias. Variations in this technique arise in the placement of this phase source within the radar system.

To further expand on possible individual techniques to achieve this aim the complete receiving system is viewed as successively more complex. In its simplest form, the primary receiving component is the receiver itself. To estimate the phase variations within this component, the MF radar has the facility for a receiver *phase check* incorporated into its design. If scheduled, a test signal is injected into each receiver before an acquisition and the receiver output is recorded whereby an estimate of the relative receiver phase differences can be obtained [*Berkefeld*, 1994]. A primary disadvantage of this particular technique is that only the receiver's phase behaviour is determined while other system components that may influence phase behaviour are excluded. A similar approach was taken in previous MF studies at the site except a voltage source external to the radar equipment was used for injection into the receivers [*Olsson-Steel & Elford*, 1987].

Briggs [1977] investigated the phase errors introduced to the original CBA sub-system of the MF antenna array (*excluding* the receivers and short patching cables for antenna selection) via calculating the cable lengths from the behaviour of frequencies causing nulls in cable impedance. From the measurements made on 32 cables, the projected phase error was $\pm 10.8^\circ$ at 2 MHz and $\pm 32.4^\circ$ at 6 MHz. In comparison, Table 3.9 displays relative cable length variations of the *upgraded* CBA sub-system using TDR techniques. If this data set is combined and a nominal velocity factor of 0.79 is assumed then the phase error is found to be $\pm 9^\circ$ at 2 MHz. Thus values derived from the two techniques compare well and the most recent cable system upgrade has

not markedly affected the nominal cable phasing characteristics[1].

A technique that aims to include all relevant phase error sources in pre-signal processor feed systems is that of feeding an attenuated transmit pulse into the system at the antenna feed point (e.g. *Holdsworth & Reid* [2002]). The primary concern with this technique is the omission of the antenna from the signal feed system, which may have a significant effect on phase behaviour. This phase calibration technique is more difficult to apply to the current MF radar due to the extensive 70 km of cable, than it is to the significantly more compact HF/VHF meteor radars systems to which it is more commonly applied, but a satisfactory resolution of the concern mentioned above may warrant the implementation at MF as a comparison to the primary technique chosen.

Phase calibration techniques that include the effect of antennas are achieved by utilising returns from a remotely positioned source. This source or target is optimally positioned in the direction of the main beam of the radar but may also be positioned at the surface depending on the radiation pattern of the antennas. Typical sources used are transponders [*Baggaley & Webb*, 1980], adjacent antennas [*Meek & Manson*, 1990][2], aircraft [*Brown*, 1992] or meteor trails themselves [*Solomon et al.*, 1998]. However a commonly used source or target at MF & HF are the partial reflections from the upper mesosphere and lower thermosphere (e.g. *Meek et al.* [1989]; *Brown* [1992]; *Vandepeer* [1993]; *Vandepeer & Reid* [1995]; *Holdsworth* [1995]; *Thorsen et al.* [1997]) and an approach using this source as a phase reference is outlined and applied here in order to correct for system errors in meteor AoA.

Using partial reflections incident radiation is scattered from the zenith at these altitudes and impinges on the receiving array as a plane wavefront. This provides a equiphase source at each antenna. Any phase irregularities between individual receiving systems will appear as a constant offset $\Delta\psi_{ij}$ to the phase offsets ψ_{ij} [*Holdsworth*,

[1]It should be noted that as both techniques exclude the receiver and short patching cable phase delays, which are present during normal radar observations, it is expected that the total system errors will be slightly higher than these values.

[2]Found to be unsuccessful, possibly due to ground reflections.

1995]. Once quantified these relative system phase errors can be used to retrospectively or prospectively correct the phase of the time series, thus achieving a phase calibrated receiving array. Critical assumptions made in the application of this technique are that all returns in the data are atmospheric in nature and emanate from the zenith.

Appropriate relative phase offsets can be derived using time or frequency domain methods via cross correlation and cross spectral functions respectively. The former method was used for these data presented here and is described briefly, while the techniques applicable to the latter method are treated elsewhere (e.g. *Van Baelen & Richmond* [1991]; *Holdsworth* [1995]). The complex correlation function $\rho_{ij}(\tau)$ is calculated for receiver combinations i, j ($i, j = 6, 10$, see Figure 6.5 on page 325) and the cross correlation phase is calculated from

$$\psi_{ij}(\tau) = arctan\Big(\frac{\mathcal{IMAG}(\rho_{ij}(\tau))}{\mathcal{REAL}(\rho_{ij}(\tau))}\Big) \tag{6.1}$$

The cross correlation phase value at zero lag ($\psi_{ij}(0)$) is taken from each height and receiver combination to form distributions of $\psi_{ij}(0)$. Due to the variations in AoAs about the zenith and thus the resulting distribution, a Gaussian peak selection process is applied to obtain the relative phase offset $\Delta\psi_{ij}$ [*Vandepeer*, 1993; *Thorsen et al.*, 1997]. This technique is summarised in Figure 6.1.

To ensure a significant level of partial reflection return from the zenith only day-time data is used to form the distributions. As meteor observation periods concluded near dawn each morning, routine atmospheric observations using a vertically directed beam were initiated until the meteor radiant next appeared above the horizon. This facilitated the collection of approximately four hours of data (concluding around noon) immediately following meteor data collection that could be used for phase offset calculation. This day-time data set is assumed to be a more appropriate choice for phase offset reduction than the night-time data for two primary reasons. *Thorsen et al.* [1997] show that the number of acceptable estimates increases significantly during the day-time hours, which translates to a reduced variability of derived mean phase offset for a receiver pair and, the night time data is often susceptible to errors due to

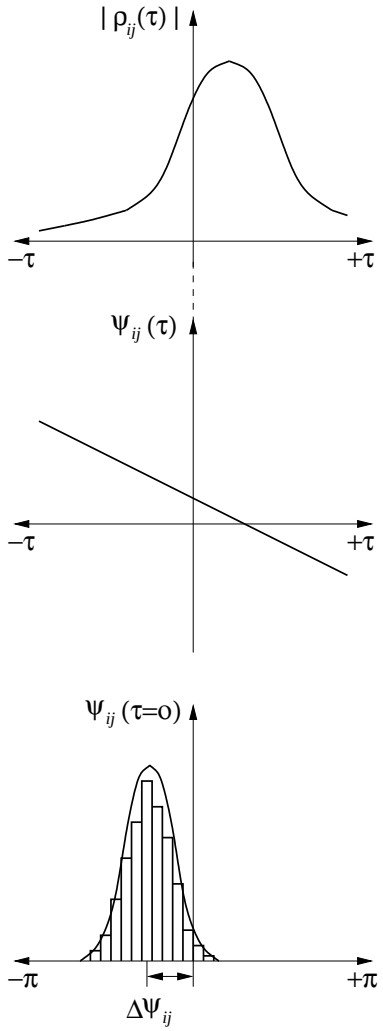

Figure 6.1: Technique to calculate the phase offsets, $\Delta\psi_{ij}$. This is completed for each appropriate receiver combination for heights in the range 70 to 100 km. Selection occurs for heights that exhibit Gaussian distributions and SNR $\geq$10 dB. These heights are then combined for each receiver combination to form an estimate of $\Delta\psi_{ij}$.

increased interference and low SNR levels. The reason for not including *all* daytime data is that as the day progresses past noon the ambient temperature of the ground increases and may induce additional phase variations in the buried cable feed system at the site (see cable phase stability discussion on page 322). A small increase in variation of the phase offsets in daytime hours post noon appears to be present in the results of *Thorsen et al.* [1997] which may be a result of a similar effect on buried or exposed cables or due to some other effect. However, during the night time meteor data collected, any ambient temperature effects are thought to be minimised and thus

an early morning day time data set which minimises any possible variation due to temperature effects is thought to be more representative of the conditions occurring during the meteor observations.

Distributions were formed for all receiver combinations for heights in the 70 to 100 km range. It was apparent that many distributions did not exhibit Gaussian behaviour and some degree of height selection was required. A possible reason for this observed behaviour is a breakdown in the assumption that the atmospheric return emanates from the zenith on average at all altitudes within this height range. Transient, atypically oriented reflecting structures at particular altitudes may provide a non-zenith scattering direction (e.g. *Brown* [1992] in reference to the work of *Murphy* [1984]). Previous authors have also implemented height selection processes. *Meek et al.* [1989] selected height ranges from 64 to 73 km at the Saskatoon site (52°N, 107°W); *Brown* [1992] at the Birdlings flat site (43°S, 172°E) used 79 to 103 km; At the Buckland Park site (35°S, 138°E) *Vandepeer* [1993] selected 76 to 86 km, while *Holdsworth* [1995] selected three height decades, 70-78, 80-88 and 90-98 km and *Thorsen et al.* [1997] at the Urbana site (40°N, 88°W) used 69 to 96 km. The varying height ranges that produce Gaussian distributions is perhaps a manifestation of the local site dependence of on-zenith scattering processes in the upper mesosphere and lower thermosphere. This suggests that the optimum approach is to evaluate the distributions for Gaussian characteristics depending on site location and the particular atmospheric structure or conditions present at specific times. In this study it was found that distinctly Gaussian behaviour was only exhibited in the height ranges 80 to 86 km. This height range encompasses that found by *Vandepeer* [1993]. Additional evidence of this height range exhibiting a predominance of echoes from the zenith at the Adelaide site is mentioned by *Lesicar et al.* [1994], noting that previous studies have found that the variability in the aspect sensitivity is at a minimum around 86 km and systematically larger above and below this height.

To further select for on-zenith atmospheric targets, noise level of the Doppler spectrum was calculated for these heights and estimates of SNR made via an implementation of the algorithm described by *Hildebrand & Sekhon* [1974]. All spectra exhibiting SNR <10 dB were rejected [*Holdsworth*, 1995]. Alternate selection criteria has been applied by other researchers such as the rejection of low zero correlation phase lag values [*Meek et al.*, 1989] and phase data not satisfying the Normalized Phase Discrepancy (NPD) condition [*Berkefeld*, 1994].

Typical distributions formed using this process are illustrated in Figure 6.2. These were formed from 110 two-minute time series acquired from 7:30 to 11:08 on 22.11.00 (Leonids 2000 Campaign).

It is apparent from the distributions displayed that some exhibit a better Gaussian fit than others. In fact two of the distributions display a good fit (combinations 6,7 and 6,9) while the other two (6,8 and 6,10) exhibit a less ideal fit. This is to be expected if the geometry of the receivers is considered. The two distributions exhibiting a less ideal fit are those most distant from the reference receiver (Rx6) (see Figure 6.5 on page 325) and is assumed to be a manifestation of the spatial non-uniformity of the atmospheric return.

If attempts to satisfactorily fit a Gaussian function to the distribution of these outer antenna combinations fails, it is possible to obtain a more representative estimate of the mean phase offset by the summation of means of more closely spaced receiver combinations. For instance, Figure 6.3 displays the distributions for receiver combinations 7,8 and 9,10 (spaced 1.8λ). These exhibit a significantly reduced standard deviation compared to the previous combinations 6,8 and 6,10 (spaced 3.0λ) primarily due to the reduced antenna spacing between these antenna pairs. If the previously determined antenna combinations of 6,7 and 6,9 are assumed to be correct then the mean phase offset $\Delta\psi_{6,8} = \Delta\psi_{6,7} + \Delta\psi_{7,8}$ (43.8°) and $\Delta\psi_{6,10} = \Delta\psi_{6,9} + \Delta\psi_{9,10}$ (19.9°). This compares favourably with the previous result of $\Delta\psi_{6,8} = 44.2$ and $\Delta\psi_{6,10} = 19.1$. If the Gaussian fit to the original receiver combination was unacceptable then the mean phase offsets were recalculated using the technique described above.

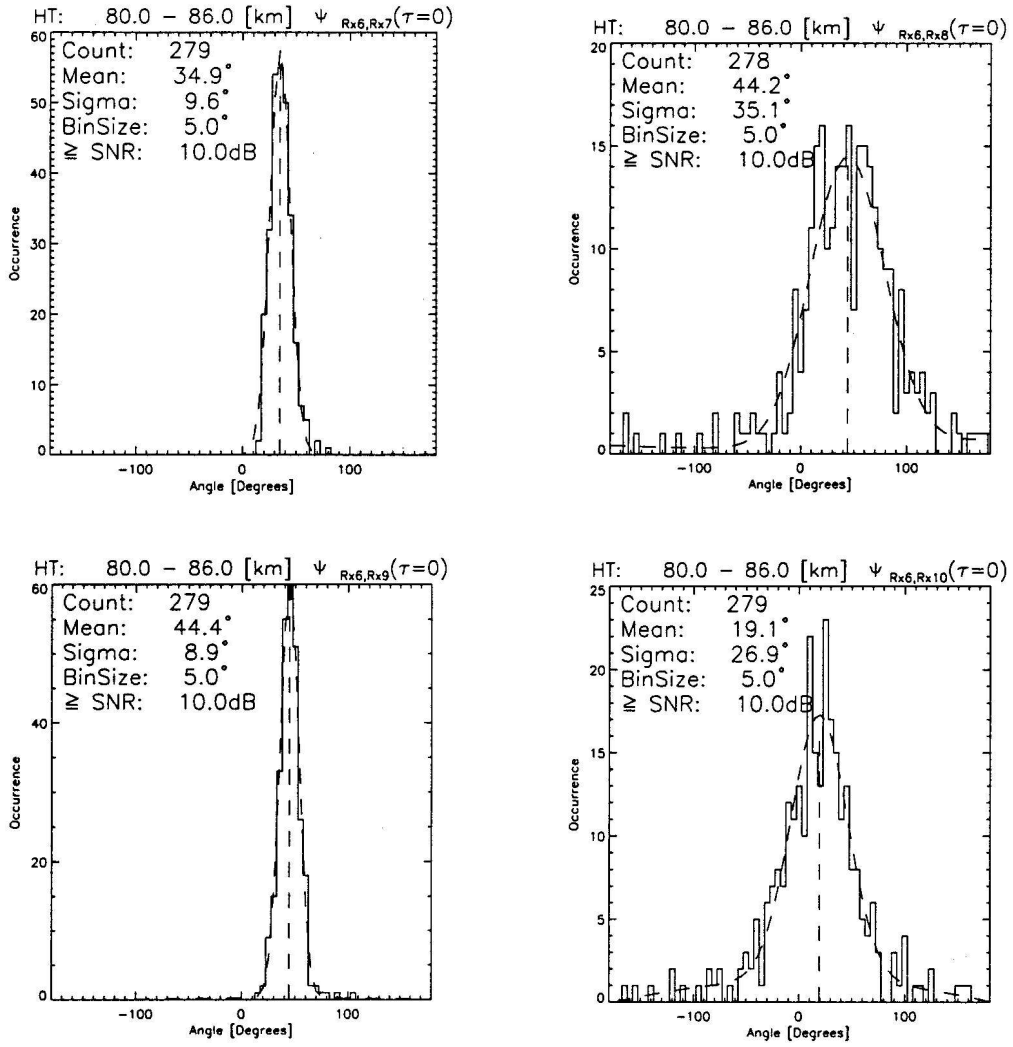

Figure 6.2: Distributions formed to determine mean phase offset $\Delta\psi_{ij}$ for each meteor receiver combination. Data set used was 110 acquisitions from 0730 to 1108 on 22.11.00. All $\psi_{ij}(\tau = 0)$ satisfying the acceptance criteria of SNR $\geq$10 dB within the height ranges 80 to 86 km contribute to these distributions.

As a number of annual shower events were examined for suitability for speed reduction, daily mean phase estimates were available for the extent of each trial campaign. An example of this is displayed in Figure 6.4. The upper panel displays the uncorrected mean phase offsets determined for the Leonids 2000 campaign (14th to 22nd November). The lower panel displays the mean phase offsets with the corrected receiver combinations 6,8 and 6,10 inserted. Both panels show a significant day-to-day

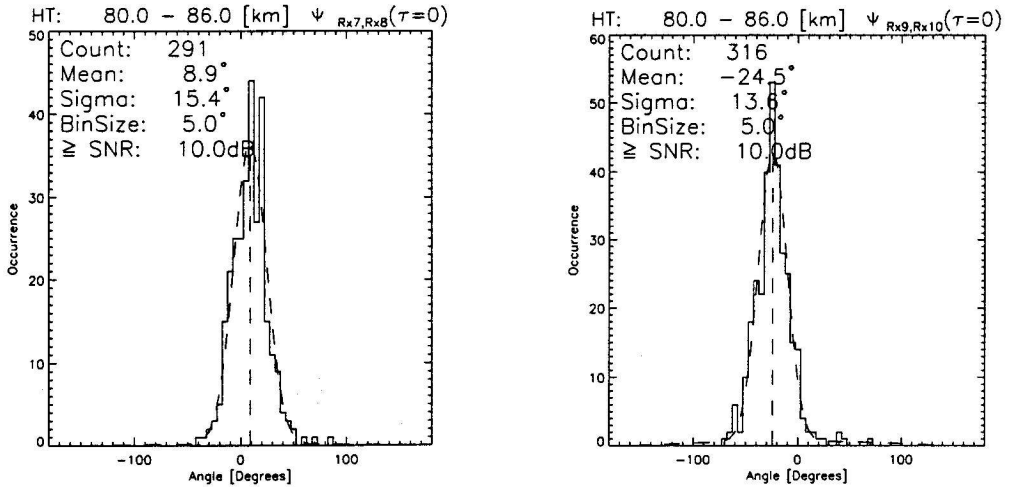

Figure 6.3: Additional mean phase offsets ($\Delta\psi_{ij}$) formed from 110 acquisition 0730 to 1108 on 22.11.00.

variation in the calculated mean phase offsets using the partial reflections phase calibration technique, with the lower panel displaying a reduced variation in the daily estimates. It is apparent from both upper and lower panels that mean phase estimates formed from more closely spaced receiver combinations exhibit less variation.

Similar daily variation has been observed at this site and because of this mean phase estimates for routinely collected data are re-calculated on a regular basis. However, the isolation of the source of this variation is important in terms of the frequency with which this task is undertaken and ultimately in whether the chosen technique is appropriate in the circumstances. *Meek & Manson* [1990] also point out the variation in mean phase values using this calibration technique over different days. However their suggested accuracy of this method of 5 to 10° (3° in zenith) is less than that indicated here and may be attributed to the differing hardware configuration. It is worthwhile to note that the lower panel of Figure 6.4 does suggest that fluctuations about a representative mean value may be revealed with a long term study. This may facilitate a more representative estimate of the mean offset and its variance for particular receiver systems.

Possible sources of this diurnal variation have been touched upon previously and

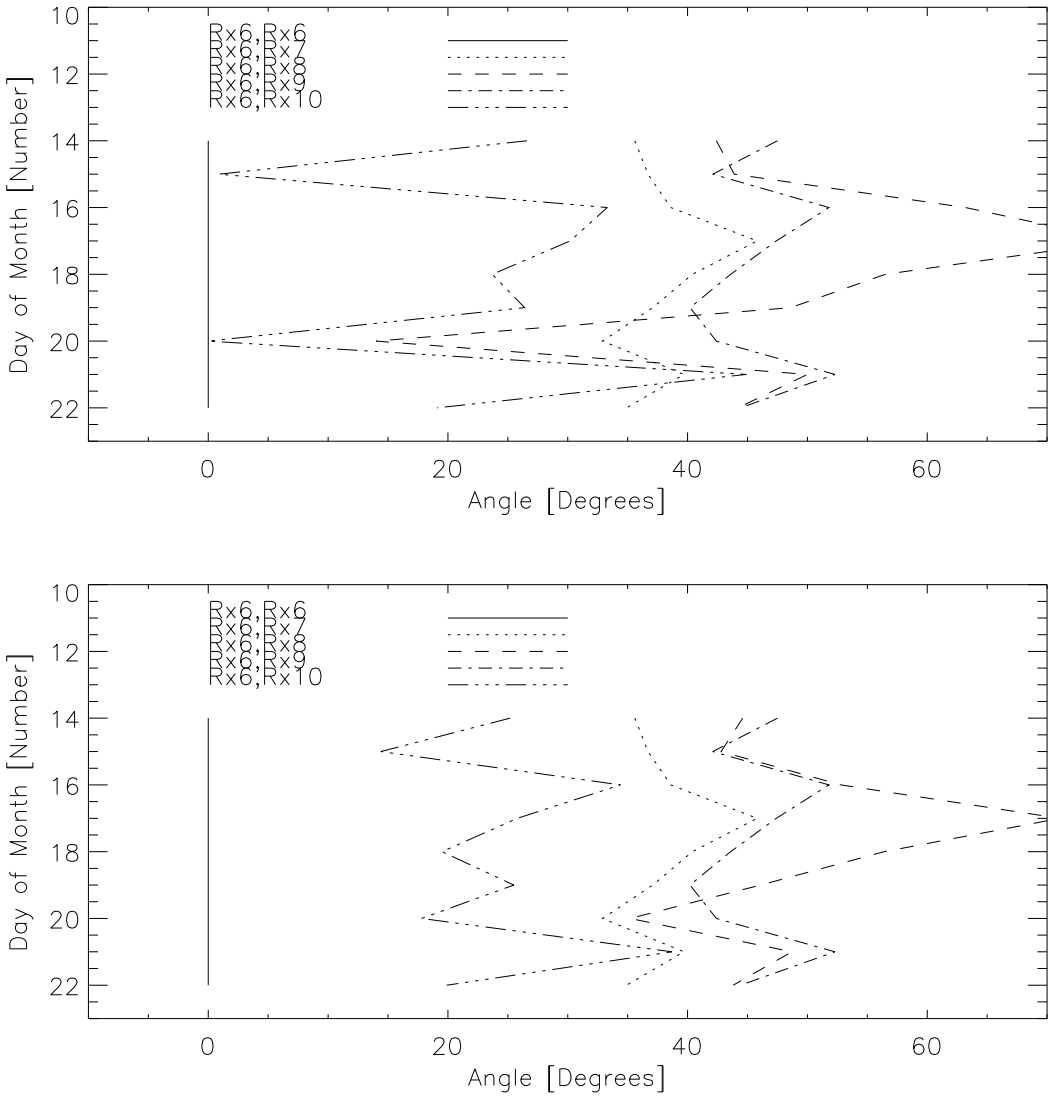

Figure 6.4: Leonids 2000 campaign: daily mean phase offset variation. The upper panel displays the uncorrected phase offsets obtained using the first approach described in the text and the lower panel displays the phase offsets with the corrected receiver combinations ((6,8) and (6,10)) inserted.

the relative influence of these are discussed further in the following paragraphs. An estimate of the variation induced by the separate components of the feed system preceding the signal processor may go some way to isolating the main source of variation and determine the limits of this phase calibration technique.

The phase offset variations were plotted (not shown) against the averaged environment temperatures for the same period from the Automatic Weather Station (AWS)

located adjacent to the MF antenna array. This analysis displayed no discernible correlation between temperature and phase offset. A lack of apparent correlation is perhaps attributed to the small change in phase behaviour of the cables with ambient temperature. The change in electrical length or phase stability ($\Delta\psi$) of a cable (in degrees) is determined primarily by the dielectric and jacketing materials and can be approximated [*Times Microwave Systems*, 2002] by

$$\Delta\psi = \frac{A\psi\Delta T}{1 \times 10^6} \tag{6.2}$$

where A is the phase temperature coefficient (ppm/°C), ψ is the electrical length (°) and ΔT is the change in temperature (t_1 to t_2) (°C). In applying this equation to the main type of cable in the MF antenna array (buried air-cored, polyethene jacketed Aeraxial cable), we assume a phase temperature coefficient (A) of -175 ppm/°C and note that this type of sheath/jacket material commonly has a temperature range of -65°C to +80°C. If a change in ambient temperature of 15°C is experienced by the cable then $\Delta\psi$ is -0.945° for a wavelength cable. For the multiple half wavelength cables contained in the array (0.5 to 4.5λ), this gives a phase stability range of -0.47 to -4.25°. The change in temperature (ΔT) assumes that the cable temperature is the same as the air which is probably appropriate for night time temperatures (winter and summer) but it should be noted that radiant heating can produce summer daytime cable temperatures of >60°C when fully exposed [*Clements*, 1972]. Although most antenna cable is not fully exposed in this case, it is expected that summer daytime temperatures result in a larger ambient temperature differential than used in this example. Overall however the ambient temperature component of the relative phase offset variation is thought to be less significant in determining day-to-day variations in comparison to other sources. It should be noted in passing that faulty cable connections or movement can contribute phase jumps of about 17° and so should be eliminated from cable systems before use or detailed study.

A component of the phase offset variation may be due to the propagation delay

experienced by the receivers. *Vandepeer* studied the behaviour of the prototype receiving system extensively and found the propagation delay to vary with IF gain changes and be modulated by a diurnal oscillation driven by laboratory ambient temperature [*Vandepeer*, 1993]. The current receiving system has not been studied in this way as yet but it is expected that it exhibits a better phase stability than the 5° peak-to-peak reported for the previous receiver system due to the regulation of air temperature by laboratory air conditioning and due to a more recent RF design.

While cable phase instabilities and receiver propagation delays contribute to some of the variation displayed in the phase offsets it is expected that primarily the off-zenith partial reflections account for a significant component of phase offset contamination, while varying antenna characteristics provide a secondary contribution. Mechanisms causing off-zenith returns may include atmospheric gravity wave activity modulating the existing scatterers responsible for partial reflection (e.g. *Hines & Rao* [1968]; *Hines* [1993], although *Hocking et al.* [1989] discuss the validity of this suggestion) and the tilting of existing or forming stratified layers. Further analysis may identify these effects and thus allow omission from data sets or require the implementation of signal processing algorithms to limit their effect. Techniques to isolate the antenna's effect on phase over a relevant temporal interval are less straightforward. It is suspected that this component may induce significant phase variations [*Holdsworth & Reid*, 2002], possibly via the mechanism of varying antenna impedance, mutual coupling effects or ground reflections [*Meek & Manson*, 1990] previously mentioned or a combination of these.

As indicated previously, an alternate approach to calculating the mean phase offsets for the receiving system utilises cross spectral techniques. It has been noted that off-zenith returns can contaminate the resulting phase offset distributions and cross spectral methods offer the ability to more simply eliminate contamination before distributions are formed. Specifically, *Briggs & Vincent* [1992] note that large off-vertical angle return can contaminate the data as high-frequency components while fixed frequency components (e.g. sea-scatter) may exist across the Doppler spectrum.

Frequency domain methods have been shown to give comparable results and if a high degree of identifiable contamination is present, may offer a more accurate solution.

From this outline of the problems inherent in this phase calibration technique it is apparent that further refinement of the technique is possible to better characterise system phase errors, however the contribution of the atmospheric component to the variation of the mean phase offsets is the limiting factor in the accuracy of this technique as currently implemented. A technique whereby this atmospheric component is excluded from the estimation, such as a test signal being injected at the antenna, is vital for precise phase (and thus AoA) estimates. Such a technique, conducted at regular intervals over twelve months, will better isolate the true levels of systematic phase error present in the hardware.

6.3.2 Angle-of-arrival via orthogonal baseline interferometry

Of the interferometry techniques described previously, the orthogonal baseline method of *Jones et al.* [1998] was implemented to obtain estimates of meteor trail reflection point Angle-of-Arrival (AoA). This particular technique is ideally implemented using a receiving array with individual element positions scaled as multiples of $\lambda/2$. Such an arrangement reduces ambiguities in AoA estimates and the mutual coupling effects of closely spaced antenna elements. The MF antenna array has a 0.60λ spacing of antenna elements and as such does not offer the full range of advantages of those arrays spaced at half the radar wavelength. However, certain implementations of this technique offer comparable results for most situations using non-ideal antenna element spacings.

Essentially, the orthogonal baselines of the ideal interferometer were re-positioned so as not to have a common centre element, but retain a common corner element (see Figure 6.5). This particular arrangement was primarily dictated by the location and availability of specific fully functional receiving dipole elements. However it serves to highlight one strength of this interferometry technique in that, as long as orthogonality of the baselines for incident plane wave radiation is retained, many different (crossing

& non-crossing) combinations of receiving antenna baselines can be arranged. Specifically, none of these combinations must have a common element, this serving only to minimise the number of dipole antennas used at one time. This technique thus facilitates significant configuration flexibility on a multiple element and multi-use array such as that employed here. Aside from the hardware considerations this technique is also well suited to software automation.

Specifically, the two orthogonal interferometer baselines (labelled 1 & 2) were configured from five east-west aligned dipoles as shown in Figure 6.5. Each antenna (9N2, 9N4, 9N7, 7N2 and 4N2) was connected to its own receiver (Rx 6, 7, 8, 9 and 10) respectively. Note the reference axes are in terms of the array symmetry which is oriented approximately 4° west from true north at the site. The case for each inter-

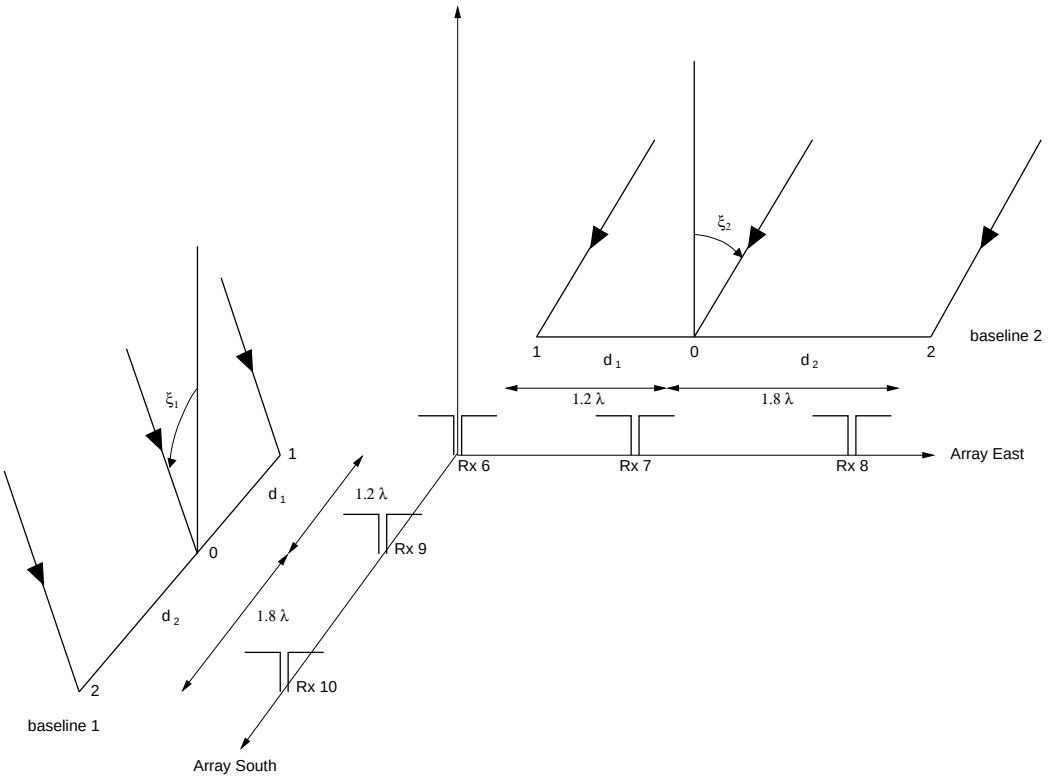

Figure 6.5: Illustrates an implementation of the meteor interferometry technique [*Jones et al.*, 1998] employed for MF meteor observations.

ferometer baseline is similar and the resulting angles ($\xi_{1,2}$) from each analysis can be used to obtain an overall AoA.

Examining the case for baseline 1 in the Figure 6.5, three linearly aligned receivers

$(1, 0, 2)$ are spaced at d_1 and d_2. A component of the radiation scattered from the meteor trail will induce a phase difference (ϕ_{10}) at antenna 1 with respect to antenna 0 along this baseline. This phase difference in general ($\Delta\phi$) is related to the path difference (PD) at the wavelength (λ) used by

$$\Delta\phi = 2\pi \, \frac{PD}{\lambda} \tag{6.3}$$

thus

$$\phi_{10} = -\frac{2\pi \, d_1 \, \sin\xi_1}{\lambda} \tag{6.4}$$

where ξ_1 is the angle as measured relative to the array normal. It can be seen that if the antenna $(1, 0)$ spacing $d_1 \leq 0.5\lambda$, then ξ_1 can be measured unambiguously. A similar case can be made for the antenna combination $(2, 0)$ such that

$$\phi_{20} = +\frac{2\pi \, d_2 \, \sin\xi_1}{\lambda} \tag{6.5}$$

Unfortunately, antenna elements in close proximity to each other are subject to mutual coupling effects which serve to increase the error in any phase estimate derived from this combination. As this is an undesirable feature of this interferometer its effect can be reduced via increasing the distance between antenna elements. However, increasing the distance between antenna elements serves to increase the level of ambiguity in angle measured. An optimisation of these competing factors can be obtained by recognizing that particular combinations of antenna elements in this baseline are able to provide a minimum and maximum element spacing that would allow a less ambiguous and more accurate angle respectively. In terms of the baseline 1 of the Figure 6.5, the angle ξ_1 from

$$\sin\xi_1 = -\frac{\lambda}{2\pi}\frac{\phi_{10} - \phi_{20}}{d_1 + d_2} \tag{6.6}$$

will provide an ambiguous but accurate estimate of ξ_1 due to the maximised effective element spacing of $(d_1 + d_2)$ $(1.2 + 1.8 = 3.0\lambda)$ while

$$\sin\xi_1 = -\frac{\lambda}{2\pi}\frac{\phi_{10} + \phi_{20}}{d_1 - d_2} \tag{6.7}$$

will provide an increasingly mutual coupled affected angle estimate with less ambiguity due to the minimised antenna element spacing of $(d_1 - d_2)$ $(1.2 - 1.8 = -0.61\lambda)$.

Once a range of estimates of ξ are obtained from these two equations, the true angle estimate must be selected. In previous angle of arrival techniques (e.g. *Tsutsumi et al.* [1999]), angle selection amongst ambiguous angle possibilities would occur via locating the most likely repeated angle of the widely and narrowly spaced interferometers. The current method achieves this true angle selection by formally estimating the mutual coupling error for each possible angle and deems the true angle that which occurs in both antenna element combinations within these errors. The error in angle $(\Delta\xi)$ is given by

$$\Delta\xi \approx -\frac{\lambda\,\Delta\phi_{10}}{2\pi\,d\,\cos\xi} \tag{6.8}$$

where $\Delta\phi_{10}$ is the finite phase error [*Jones et al.*, 1998].

This process is illustrated for a meteor detected at 02:10:58 on the 22.10.00 during the Orionids campaign. Values of ξ_1 and ξ_2 need to be determined for each baseline combination. The Figures 6.6 and 6.7 display the case for baseline 1 and 2 respectively. In each figure there are three plots with the upper two illustrating the implementation as described by *Jones et al.* [1998] and outlined in the previous paragraphs while the lower plot illustrates an extension to this technique. In each figure the top diagram illustrates the ambiguous but accurate estimate of ξ described by Equation 6.6 (for a phase difference $(\phi_{10} - \phi_{20})$ determined from a section of phase information post amplitude peak). The middle diagram illustrates the less ambiguous but inaccurate estimate of ξ that allows the isolation of the true ξ from the upper diagram. $\xi_{1,2}$ are +27.6 and -15.5° respectively.

To further reduce the error in the resulting ξ, the combination ϕ_{YZ} can be employed (e.g $\phi_{1,2}$: $\phi_{6,10}$ (baseline 1) and $\phi_{6,8}$ (baseline 2)). The subscripts YZ are used here to highlight the fact that it is possible to select antennas other than those in the existing five element interferometer, if available, provided they maintain the correct alignment. These combinations will have a reduced error in ϕ_{YZ} (difference) compared to the

$\phi_{10} - \phi_{20}$ and $\phi_{10} + \phi_{20}$ (difference of a difference) and low mutual coupling error ($\Delta\xi$) because of the significant antenna element spacing. This facilitates a ξ value with a reduced error. The utilisation of other baseline combinations to extend the technique of *Jones et al.* [1998] has also been employed by other researchers (e.g. *Holdsworth & Reid* [2002]). The azimuth and zenith can be deduced from these two angles via geometrical arguments based on Figure 6.5. The angle-of-arrival for the reflection point of this meteor was calculated to be 204.2° (azimuth) and 30.6° (zenith).

For the successful implementation of this technique the errors associated with the input quantities must be finite and within certain constraints. If this is not the case failure in the selection of an unambiguous angle will result. The error in the phase difference was estimated using a cyclic average of the ensemble of values in the linear portion of each receiver's phase series. These estimates however were found to be less than those obtained via system phase calibration described earlier and thus the latter results were employed as more representative of the contributing error. Provided a range of this error was contained over 5 to 20°, effective AoA determination via this technique was routinely possible.

Also contributing to the effective selection of the unambiguous angle is the error attributed to mutual coupling, but the limited combinations of (non half wavelength) element spacings meant that this had to be tolerated to a large extent. A consequence of this situation is that as ξ approaches the array axis, the uncertainty in the phase may become too large to allow a selection. An example of this situation is also discussed in *Jones et al.* [1998]. In the current implementation an AoA was not available when component (ξ) estimates exceeded 70°.

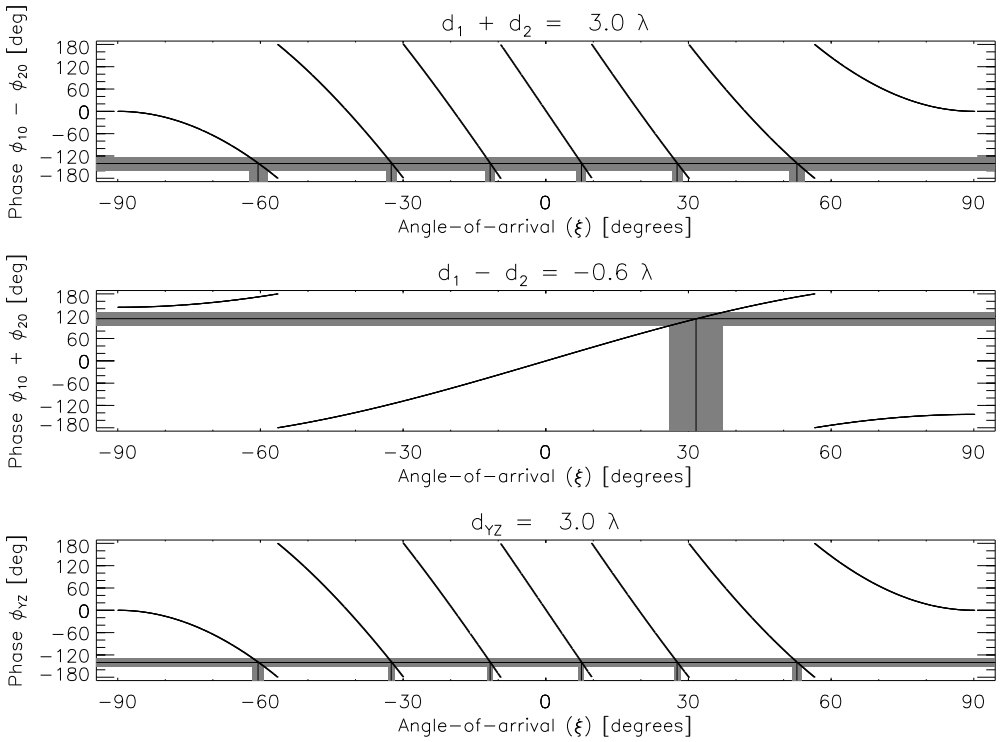

Figure 6.6: Resulting plots for baseline 1 case. $\xi_1 = 27.6°$.

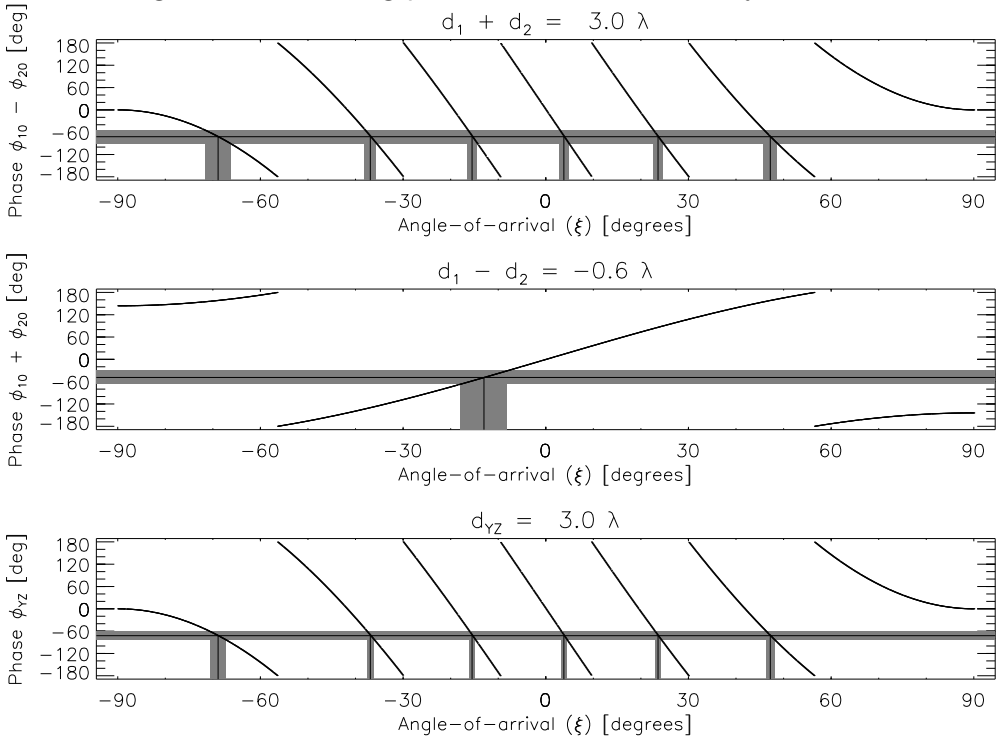

Figure 6.7: Resulting plots for baseline 2 case. $\xi_2 = -15.5°$.

This limitation had a negligible impact on results as no meteors were found to have components exceeding this angle. In fact the angle of arrival determined via this technique was successful in the majority of cases. Also the quality of the result was found to be consistent over adjacent range gates of a meteor event, with no significant variations, aside from the extreme upper and lower range gates which typically exhibited the lowest SNRs. However it was noted that limitations in the quality of the phase information across the five receivers did limit the determination of AoA for numerous meteor events and these were rejected from further analysis.

Provided an increase in the precision of the phase calibration is attained it may be worthwhile to employ additional antenna elements significantly spaced from existing elements (e.g. *Jones et al.* [1998] suggest 30λ). The practical application of this extension to the technique must consider the extent of correlation of the meteor signal over the closely spaced elements to that of the extreme elements. It may be found that there is insufficient echo for phase analysis to proceed, due not only to different scattering geometry at these spaced receivers but the level of attenuation introduced in cable feeders to the widely spaced elements and the inherent variable dynamic range of meteor events. *Jones et al.* [1998] note that the distance cannot be increased indefinitely because the separation of the multiple estimates in the echo direction for the wide spacing must be greater than the uncertainty in the estimate from the close spacing.

The two concerns touched upon previously, namely that of the errors introduced due to the array phase calibration and the mutual coupling of the receiving array, suggest areas for future investigation. Provided an optimum element spacing is obtained, the overall accuracy of the AoA is significantly dependent on effectiveness of the phase calibration of the system. The partial reflection phase calibration technique implemented here (see section 6.3.1) currently limits the precision of phase values used in the interferometry technique. Also, as described previously the estimated errors in phase attributed to mutual coupling effects have a significant impact on AoA derived and in this current arrangement impose limits at $\xi = 70°$. Investigating the actual

influence of mutual coupling may go some way to extending this range or clearly identifying particular limits. Mutual coupling between antenna elements has been extensively investigated [*Weeks*, 1968; *Gupta & Ksienski*, 1983; *Krauss*, 1988; *Galati*, 1993; *Balanis*, 1997]. Two primary areas that influence the behaviour of mutual coupling are element spacing and element orientation. As the elements are spaced at 0.6λ phase information is influenced more significantly by mutual coupling than at multiples of half wavelength. Similarly each antenna baseline contains antenna elements orientated either side-by-side or co-linearly. The effect of mutual coupling due to orientation differs and this will lead to significantly different estimates of this effect for each baseline. Further analysis may also require an estimate of the interaction between the different baseline orientations as well as including the influence of any adjacent antennas employed for non-interferometric applications. This illustrates that the effects of mutual coupling for an interferometer implementation of this type is more complex and could be better quantified.

Previous studies at this site conducted by *Rossiter* [1970] suggested little coupling exists between antenna pairs although the technique utilised atmospheric partial reflections which may have introduced some variability to the data collected. Researchers using equipment at other sites have also found negligible coupling. *Morton & Jones* [1982] found that the mutual impedances of the antennas were low enough not to introduce significant non-linearities into the phase measurements on a system with element spacings of 0.9, 1.0 and 2.5λ, while *Baggaley & Webb* [1980] also measured interferometer coupling (antenna spacing 1.6 and 20λ) and found no significant coupling was present. However no recent studies have been completed on the extensive BP array system. These possible effects may be modelled using software packages such as NEC-2 [*Burke & Poggio*, 1981] and measured on site using current technologies. Thus theoretical estimations could be compared with experimentally derived values and the results included in subsequent interferometry calculations. In contrast to isolating the mutual coupling influence within the confines of the technique of *Jones et al*, alternate approaches may be warranted such as the eigenstructure-based method of *Friedlander*

& Weiss [1991].

Aside from the specific concerns of this implementation of the technique there are some issues regarding the standard implementation as described by *Jones et al.* [1998]. The technique claims theoretical accuracies of 0.3° for echoes of 20 dB and demonstrated accuracies of ±1.5°. The discrepancy in accuracies being attributed to the effects of uneven terrain and trees that may be alleviated by a carefully constructed ground plane or the use of antennas with polar diagrams that minimise ground reflections. However in most implementations it seems realistic to suggest that phase accuracies within the system hardware need to be strictly established and eradicated to achieve this level of accuracy before attention is directed at limiting the influence of the ground plane or surrounding environment. As discussed, the phase calibration of the system needs to be firmly established including the significance of all diurnal variations over extended periods. This may or may not include errors due to master oscillator, receiver or feeder cable phase drift. Similarly, the SNR of the echo is an important factor in limiting phase errors. Low SNR introduces more uncertainty in the recorded echo phase and echoes exhibiting low SNR are relatively common at MF frequencies (due in some part to the increase in noise sources at this frequency in comparison to VHF). Coherent integration of the signal is not an option, as discussed previously. This situation is compounded by the spacing of the receiving antenna elements which provide a source of variation in the SNR of the recorded echo phase. To attain precise AoA estimates the SNR of typical echoes at MF would need to be improved on average.

A strength of this interferometry technique is the simplicity of the angle selection process via estimation of the mutual coupling error. While it is readily apparent that mutual coupling effects are a significant cause of errors in the phase measured at grouped antenna elements, this is not the only error source. Inclusion of other error sources may provide a more realistic picture. The AoA estimates are used extensively in subsequent processing, being vital to the calculation of meteor height, so there is strong motivation to improve the AoA estimates produced from any interferometer

system.

6.3.3 Meteoroid speed via the Fresnel phase-time technique

Of the range of techniques to deduce meteor speed outlined in section 5.3.1.3, the Fresnel phase time method [*Cervera*, 1996; *Cervera et al.*, 1997] was most applicable to the MF data collected as indicated previously and a more detailed description of this technique, as applied to specific examples, is illustrated in the following section.

Figure 6.8 displays a typical meteor echo. The amplitude and raw phase derived from the in-phase and quadrature components of the recorded signal are illustrated in the upper and middle panels. The raw phase information is cyclic over 2π radians as determined directly from the in-phase and quadrature signals and while substantial characteristic meteor phase behaviour occurs within this range, significant information ranges outside and is thus aliased. A simple method for unfolding or unwrapping this type of information was used by *Adams et al.* [1985] in application to real scattering points and this approach has been subsequently applied to meteor echoes [*Cervera*, 1996]. Essentially 2π radians are added to or subtracted from the phase of all subsequent points based on whether the difference between a chosen point and the subsequent point is greater than $+\pi$ or less than $-\pi$ respectively. An alternate implementation of this basic concept has been developed by *Campbell et al.* [2000] using differential techniques to ensure optimal phase unfolding, however similar results are obtained using either approach. It should be noted that artificial signals may be created in certain circumstances [*Cervera*, 1996; *Campbell*, 2000], particularly if the original phase (and amplitude) data contain significant noise. However, all instances of this have been identified in this study and only verified un-aliased phase unwrapped series have been used in subsequent data reduction.

In relation to this particular example the characteristic sharp risetime in amplitude of the meteor event appears at about 15 seconds into the acquisition and falls below the background noise approximately 14 seconds later. This initial sharp risetime and the characteristic minimising of phase at about 15.3 seconds identifies this signal as a

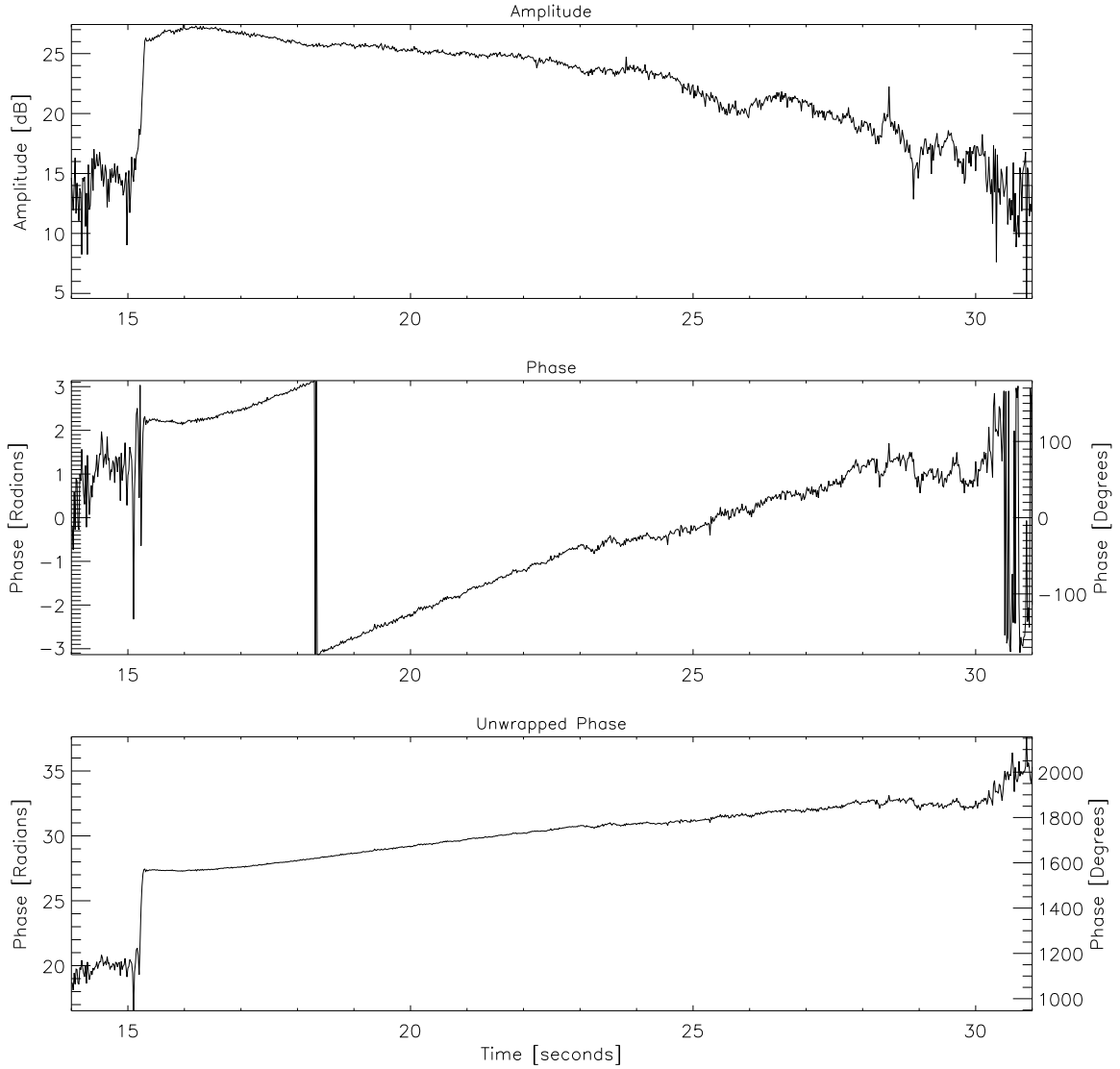

Figure 6.8: Meteor event observed in acquisition 01:48:40 CST on the 22nd of October 2000. The top panel displays amplitude, middle panel raw phase and lower panel unwrapped phase. The abscissa is time offset from the acquisition commencement time. This echo was observed in the 116 km range gate (height 104 km) and is typical of the an overdense type meteor.

meteor event. Unlike the classic underdense echo that exhibits a distinctive exponential decay following a maximum in amplitude, this echo displays an initial local maximum at 15.3 seconds followed by an amplitude maximum at about 16.2 seconds. Subsequent to this a restricted decay is apparent until around 23 seconds, where it is assumed the trail's initial structure becomes degraded likely due to a more complex reflection process taking place from multiple reflection centres. Similarly, the phase exhibits behaviour similar to theory with minor Fresnel oscillation occurring after the initial peak, then a linear phase increase until around the 23 second mark. Within this region the phase is slightly affected by the apparent overdense nature of the the echo. A further distinct linear trend of the phase between 23 and 28 seconds is probably due to the "true" wind effect. Phase coherence is lost subsequent to 28 seconds. The general behaviour of the amplitude and phase of this echo can be examined using the reflection coefficients and phase behaviour of models described in *Ceplecha et al.* [1998]. This indicates that the echo of Figure 6.8 is due to an overdense trail formation within the radar beam. Due to the extensive pre-t_0 phase profile available in this example, it is possible to deduce a meteor speed using the Fresnel phase time method.

The reduction of meteor speed using the Fresnel phase time/pre-t_0 technique from this phase profile requires four main steps; a) detrending the echo of background wind effects, b) applying an appropriate model to establish theoretical phase behaviour, c) relating observed echo to distance along the trail and d) determining the the meteor speed from a linear fit to this data.

The trail is formed in the dynamic environment of the upper atmosphere. A dominant phenomenon that modulates trail behaviour is that of the atmospheric wind, whereby the trail drifts with the neutral wind. In the following analysis it is assumed that only the influence of the neutral wind has a significant effect on trail behaviour and that other phenomenon, such as when the trail is closely aligned with the Earth's magnetic field or its motions vary in the presence of very strong electric fields that may occur during high geomagnetic activity [*Avery et al.*, 1983], are not significant. Assuming the primary distortion of the trail is due to the background wind, this effect

is apparent in the meteor phase profile as the linear phase section after the phase minimum. If the Doppler shift (Δf) is

$$\Delta f = \frac{d\phi}{dt} \tag{6.9}$$

where ϕ is the phase and t is time, then Δf may be estimated by fitting a straight line to the linear phase profile. Assuming that this Doppler shift is constant over trail formation the trail complex time series (E') can be de-trended (E) using [*Cervera*, 1996]

$$E = E' e^{i\xi} \tag{6.10}$$

where $\xi = t\Delta f$.

After the deleterious effects of the atmospheric neutral wind has been removed the meteor speed determination utilises the pre-phase minimum information and this region of the meteor event is more clearly illustrated in Figure 6.9. Once a verified unwrapped and non-aliased phase series has been extracted it is then related to a model phase series.

The model used has been developed by *Elford* and is described in *Cervera* [1996] and *Cervera et al.* [1997]. Model phase series were determined for trail line densities ranging from 10^{13} to 10^{16} electrons per metre, for height ranges of 75 to 100 km in 5 km increments and speeds of 20 to 60 km s^{-1} in 10 km increments. A model series was selected based on the previously determined height and on the expected shower or sporadic most likely speed. Figure 6.10 illustrates how this model phase is utilised to deduce meteor speed.

The uppermost panel of Figure 6.10 displays an example model phase profile in terms of x value (labelled as *relative* x). It should be noted that the model phase displayed here extends for many cycles back over the pre-t_0 region. This is useful for application in VHF situations but less so for the typical MF meteor echo, which has a limited pre-t_0 extent and thus only requires the modelling of a limited number of cycles preceding the point of closest approach to the radar.

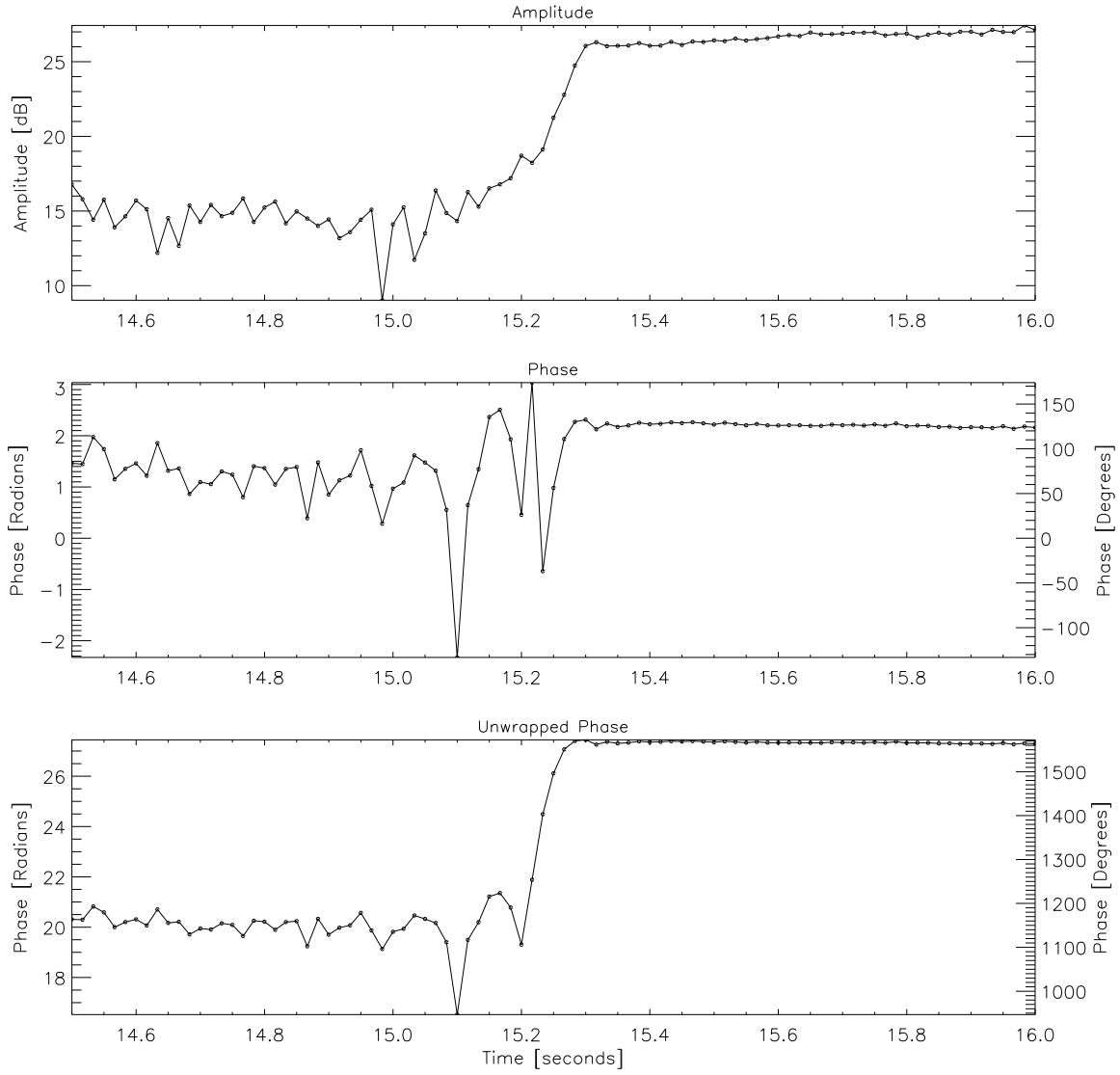

Figure 6.9: Meteor event observed in acquisition 01:48:40 CST on the 22nd October 2000: focusing on the pre-t_0 behaviour. A similar format to the previous figure with the additional highlighting of the individual samples contributing to the echo.

The second panel in Figure 6.10 displays the selected region of the unwrapped phase of the detected meteor event. A total of five pulses were available from this unwrapped phase profile beginning as the signal becomes coherent from the background noise (pulse number zero in bottom panel) to the estimated phase minimum position (pulse number four in bottom panel). This unwrapped phase has been re-scaled to be consistent with the format of the chosen model phase profile. Depending on the sampling interval of the data there maybe more than one possible location of minimising phase. This facilitates the additional iterations of the process to select the most

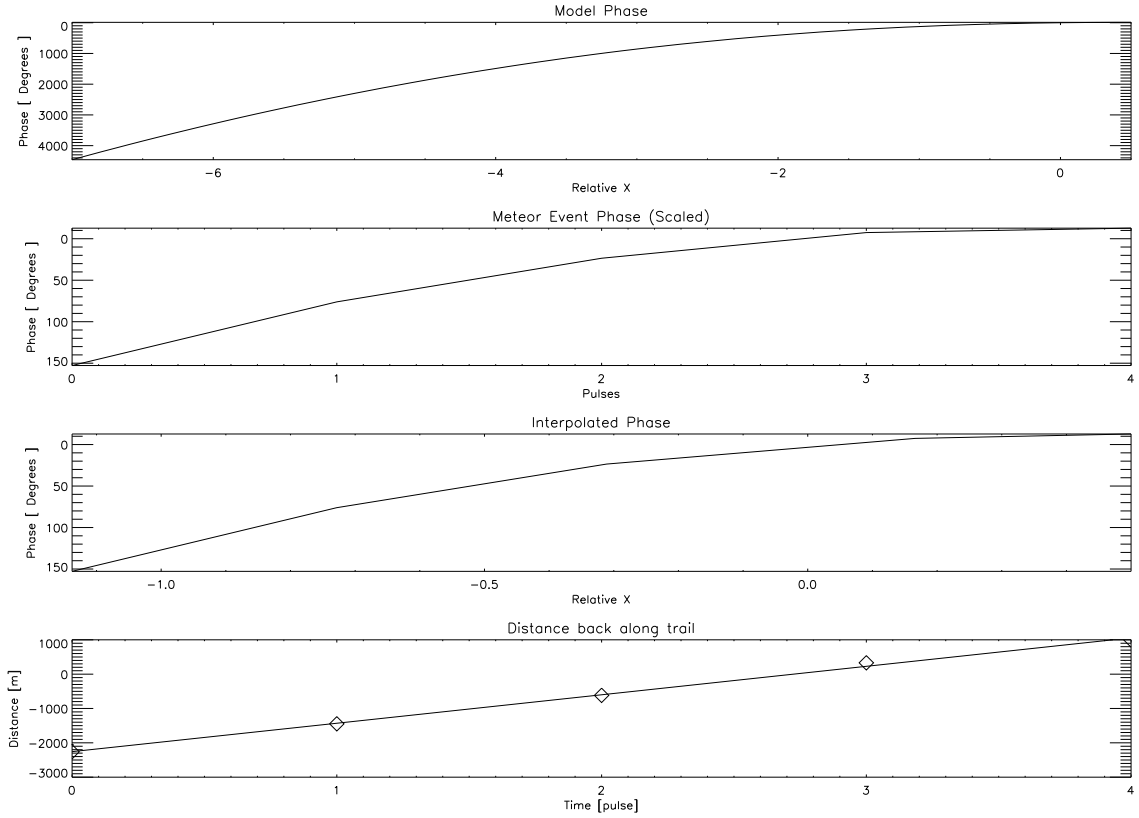

Figure 6.10: Meteor event observed in acquisition 01:48:40 CST on the 22nd October 2000: speed calculation. The top panel illustrates the model phase profile and the second panel displays the (re-scaled) unwrapped meteor phase. The third panel illustrates interpolated phase, while the lower panel shows the calculated meteor distance back along the trail. Meteor speed is 65.0±1.8 km s^{-1}.

suitable based on the later described χ^2 statistic.

This observed meteor phase profile is then interpolated with the aid of the model phase profile to obtain a phase profile in terms of *relative* x (see the third panel of Figure 6.10). The distance back along the trail versus time can then be retrieved using the relation $s = x\sqrt{R_o\lambda}/2$ (panel four in Figure 6.10). Meteor speed is determined from a linear least squares fit to these data points.

At the higher sampling rate that often accompanies VHF meteor radar data, there may be some ambiguity in the location of the phase minimum point (P_{min}) of the unwrapped phase profile. As mentioned above this will affect the interpolated phase profile obtained and hence the derivation of meteor speed. Due to the significantly lower sampling rate used at MF, in many instances there is less ambiguity in the

location of this minimum. However, multiple possible occurrences do allow the implementation of a selection technique to ensure the most representative meteor speed is retained. This was achieved by utilising the χ^2 statistic as a measure of the *goodness of fit*

$$\chi^2 = \frac{1}{N-2}\sum_{i=0}^{N}(f_i - s_i)^2 \tag{6.11}$$

where f_i are the linear least fit values and s_i are the respective distances. Minimising this statistic over the set of possible phase minimum positions facilitated selection of the most appropriate meteor speed. The error in the speed is that obtained from the least squares fit [*Cervera et al.*, 1997].

Figure 6.11 displays the amplitude, raw phase and unwrapped phase of a meteor echo recorded at 02:24:00 on 22 October 2000. This echo shows a distinct linear trend in the unwrapped phase from 19 to 44 seconds, characteristic of wind action on a meteor trail.

Figure 6.12 focuses on the pre-t_0 series of the echo and highlights the number of samples available for a speed determination. Following a similar process as described in the previous case, Figure 6.13 displays the speed determination for this echo, using eleven samples from the phase series. A speed is 24.0±0.9 was determined.

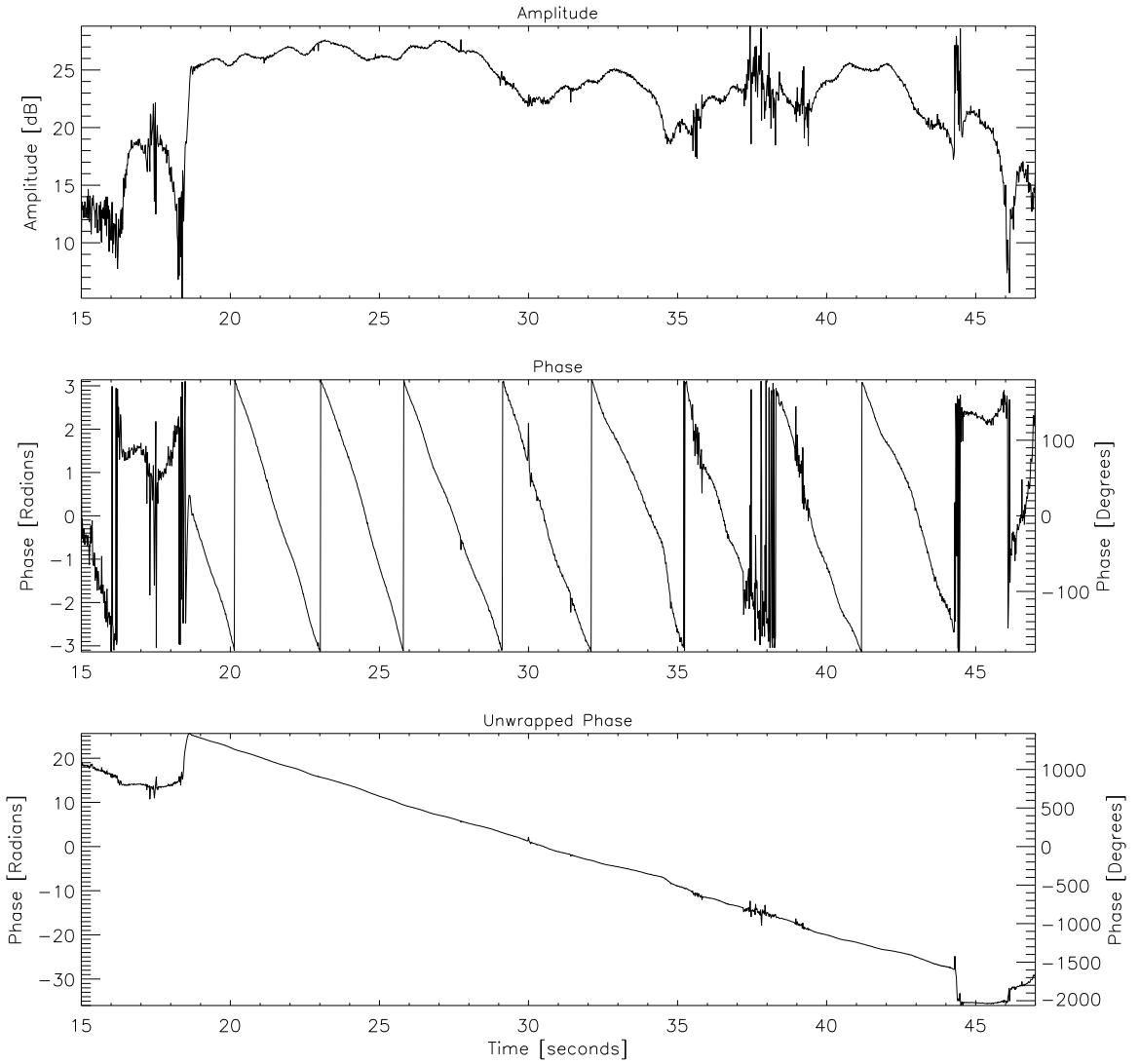

Figure 6.11: Meteor event observed in acquisition 02:24:00 CST on the 22nd of October 2000. Top panel displays amplitude, middle panel raw phase and lower panel unwrapped phase. The echo was observed in the 96 km range gate (height 87 km).

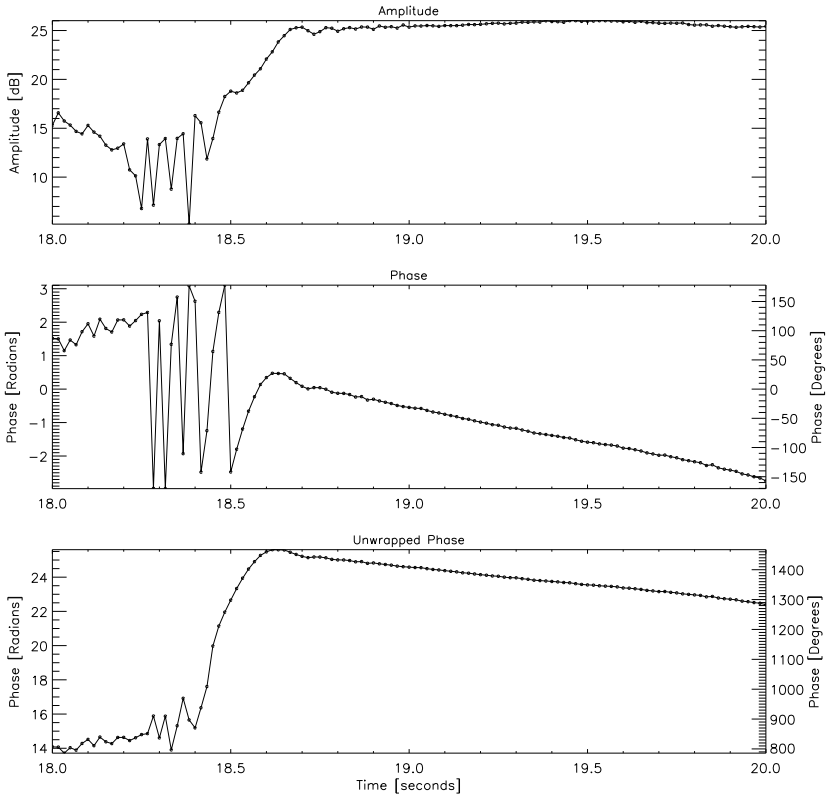

Figure 6.12: Meteor event observed in acquisition 02:24:00 CST on the 22nd of October 2000: focusing on the pre-t_0 behaviour. Individual samples are indicated.

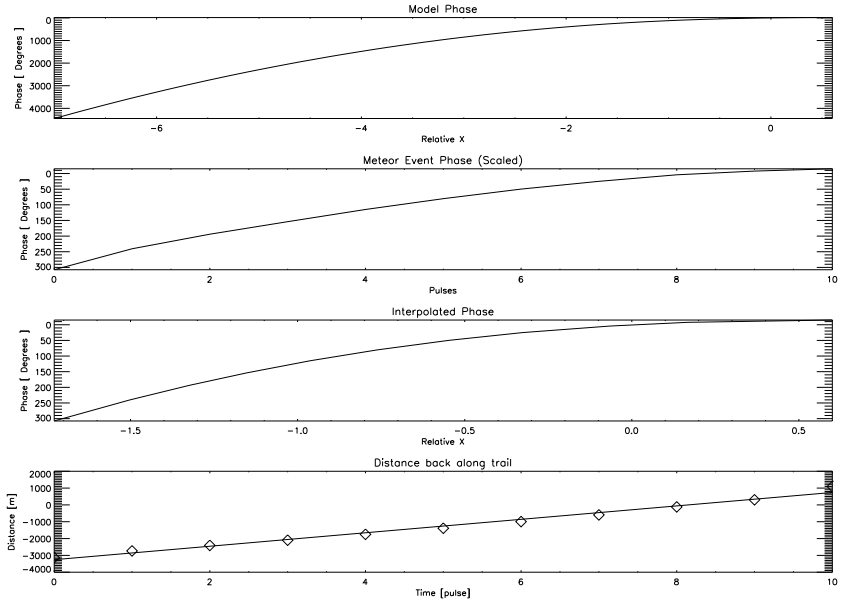

Figure 6.13: Meteor event observed in acquisition 02:24:00 CST on the 22nd of October 2000. Panels show model phase (top), unwrapped meteor phase, interpolated phase and meteor distance back along trail. Speed is 24.0±0.9, height 87 km.

6.3.4 Selection of shower meteors via geometry

In order to select the shower echoes from the background the radiant location method developed by *Elford* [1954] was adapted and applied to the data. This particular technique is outlined below.

The source of established meteor shower activity is conveniently recorded as shower right ascension (RA) and declination (δ) (see e.g. *Ceplecha et al.* [1998] or IMO publications). This celestially based system thus provides a fixed pair of coordinates to describe a shower's source of activity which may extend over a period of hours or weeks. The radar determined reflection point of a meteor trail, formed from a meteoroid originating from such a stream or elsewhere, is initially more conveniently expressed in terms of the local terrestrial-based coordinate system. To reconcile a meteor echo reflection point obtained in the observer's frame in terms of a possible source radiant's right ascension and declination a translation can be formulated between these established coordinate systems. This is essentially the technique of *Elford*.

Consider Figure 6.14. An observer O or radar is located at the origin of a left-handed coordinate system[3] defined by ON, $(+x)$, $OE(+y)$ and OZ $(+z)$ in accordance with the local cardinal points ($NESW$) and observer's zenith (Z). A second coordinate system is defined by the axes OP $(+x)$, OE $(+y)$ and OT $(+z)$. This system represents the celestial sphere where P is the north celestial pole (NCP), P' (not shown) is the south celestial pole (SCP) and thus POP' defines the celestial polar plane and TO lies along the celestial equatorial plane (defined by ETW). Thus the second system is essentially a rotation of the first system about the EW axis. Let us define a radiant position R, which is located just above the celestial equatorial plane for clarity in the diagram. This radiant can also be viewed here as rising in the north-east of the observer's frame. The radiant can also be defined in terms of an hour angle $(+H)$, which is measured westwards from transit (T) and declination (δ) measured positively from the celestial equator toward the north celestial pole.

[3]A left-handed coordinate system is chosen as it more naturally suits the radar azimuth and zenith coordinates defined with respect to true north.

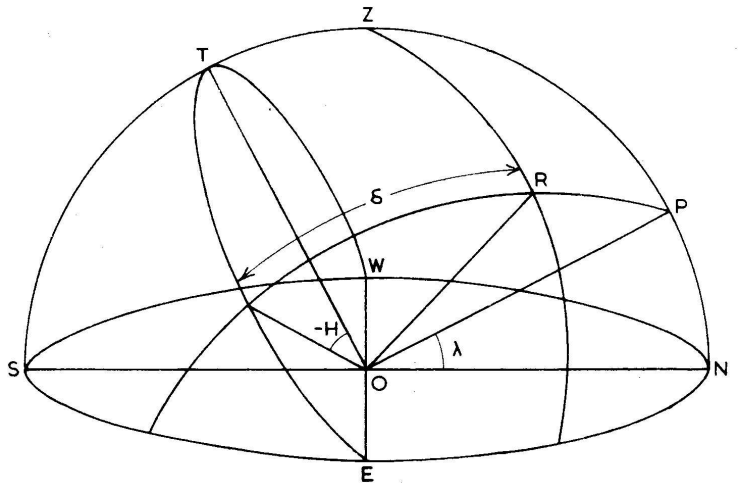

Figure 6.14: Orientation of the radiant with respect to the local observing frame ($NESW$) and the celestial frame ($PEP'W$) (from *Elford* [1954]).

For a defined radiant vector OR, the reflection point of any shower meteor will be constrained to lie on a plane that includes the origin and is orientated perpendicular to this vector. This is illustrated in Figure 6.15 where a possible reflection point is designated (1). It should be noted that only the shower reflection points constrained on this plane and located above the observer's horizon ($NESW$) are physically observable for a single radar station.

To more compactly find the equation of this plane in the celestial frame we can define both the position of the reflection point (1) and the radiant (R) in terms of their direction cosines.

The direction cosines of the radiant (L, M, N) can be formulated in terms of the radiant hour angle (H) and declination (δ) such that

$$L = \sin\delta \tag{6.12}$$

$$M = -\cos\delta\sin H \tag{6.13}$$

$$N = \cos\delta\cos H \tag{6.14}$$

In a similar fashion, if we define ϕ to be the angle measured eastwards from transit (T) to the projection of the reflection point vector $O1$ on the celestial equatorial plane and α is the angle this vector makes with the OP axis, then the direction cosines of

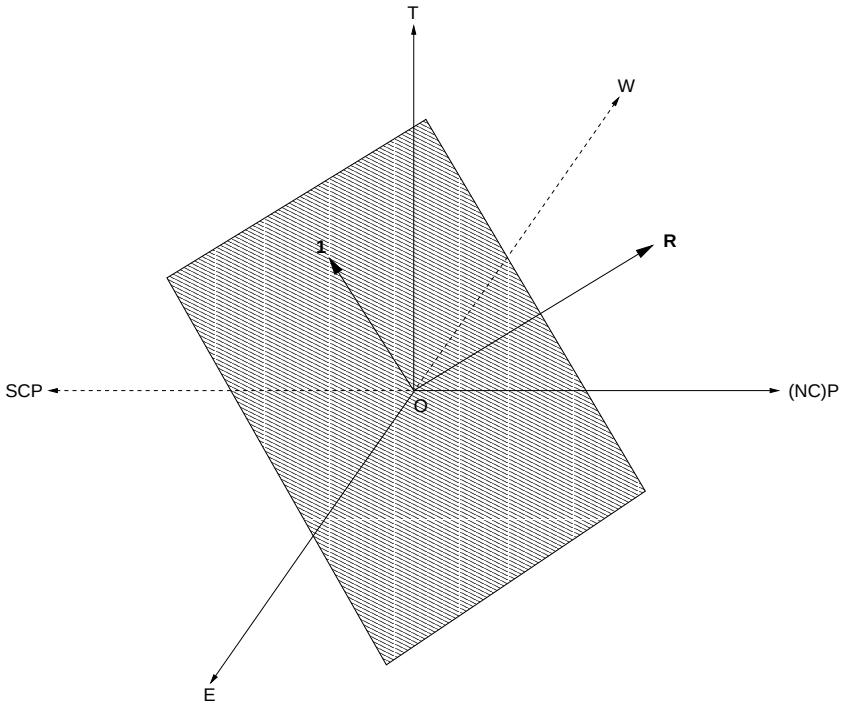

Figure 6.15: Orientation of the reflection point plane with respect to the celestial coordinate system. The shower radiant (R) gives rise to reflection points (e.g. labelled point 1 in figure) that are constrained to lie on a plane perpendicular to R. A reflection point from this radiant may lie anywhere on this plane.

the reflection point (l_1, m_1, n_1), also in the celestial frame, are given as

$$l_1 = \cos\alpha \tag{6.15}$$

$$m_1 = \sin\alpha \sin\phi \tag{6.16}$$

$$n_1 = \sin\alpha \cos\phi \tag{6.17}$$

These relations can be used in the equation of the reflection point plane due to the radiant which is given as

$$l_1 L + m_1 M + n_1 N = 0 \tag{6.18}$$

Substituting equations 6.12 to 6.14 in equation 6.18 and re-arranging for $\tan\delta$ gives

$$\tan\delta = \frac{m_1 \sin H - n_1 \cos H}{l_1} \tag{6.19}$$

Using equations 6.15 to 6.17 this reduces to

$$\tan\delta = \tan\alpha \cos(\phi + H) \tag{6.20}$$

The hour angle of the radiant can be reformulated as $H = H_0 + t/4$ where H_0 is the hour angle of the radiant at midnight and t is the number of minutes after midnight the echo appears. Thus we can write

$$tan\,\delta = tan\,\alpha\,\cos\,[H_0 + (\phi + \frac{t}{4})] \tag{6.21}$$

This is the polar equation of a line in variables $tan\,\alpha = (1 - l_1^2)^{1/2}/l_1$ and $T = \phi + \frac{t}{4} = \arctan\left(\frac{m_1}{n_1}\right) + \frac{t}{4}$ [*Elford*, 1954]. If $|\tan\alpha|$ vs T is plotted as shown in Figure 6.16, the reflection point of meteoroids that coincide with a specified radiant (H_0, δ) will appear to lie along a line.

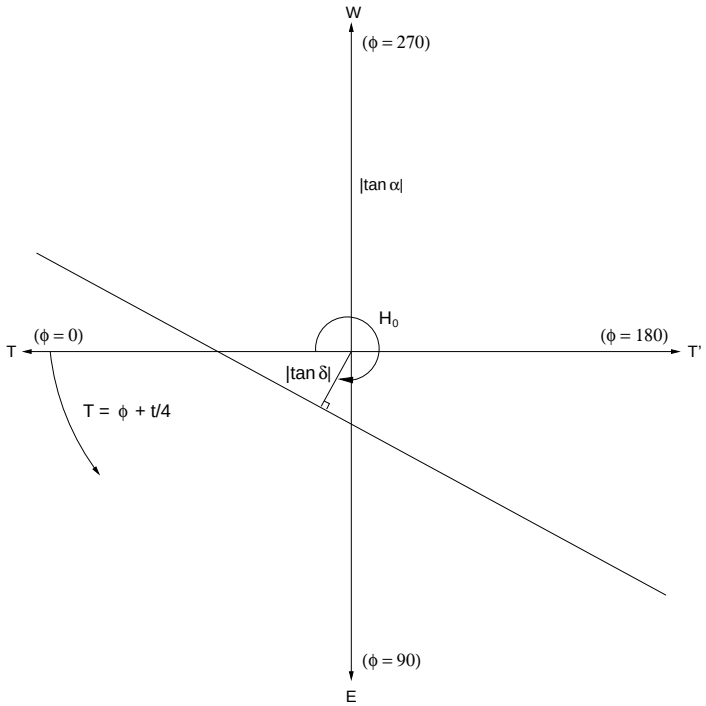

Figure 6.16: Orientation of the $(|\tan\alpha|, \phi + \frac{t}{4})$ plot. The radiant hour angle at midnight (H_0) is measured westwards from transit and $|\tan\delta|$ is the perpendicular distance from the origin to the radiant line. In this particular example $H_0 \sim 291^\circ$ and $\delta \sim 16^\circ$ for the case of the Orionids radiant on 22 October 2000.

Note that the polar equation of a line (Equation 6.21), is defined in terms of direction cosines of the reflection point (l_1, m_1, n_1) in the celestial frame. In practice the orientation of the reflection point is measured in the observer's frame as azimuth and zenith parameters defined with respect to the radar site true north and thus must be

translated to the celestial frame for plotting. To facilitate this we first define the direction cosines of the reflection point (l_A, m_A, n_A) via angles $(\alpha_A, \beta_A, \gamma_A)$ in the observer's frame in terms of the radar derived azimuth (ϕ_A) and zenith (θ_A) angles. This is illustrated in Figure 6.17. Note that for diagrammatic clarity this arbitrary reflection

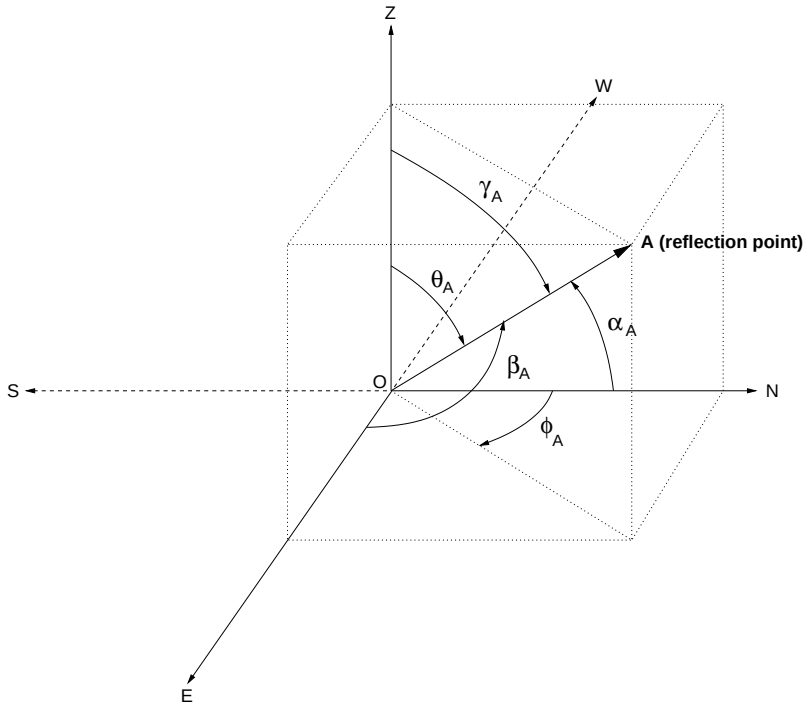

Figure 6.17: Defining radar angles (ϕ_A, θ_A) and direction cosines $(\alpha_A, \beta_A, \gamma_A)$ for a reflection point (A). The reflection point is drawn to reside in the NEZ octant for clarity, however it should be noted that this is a non-physical orientation as the radiant vector occupies this octant in previous figures. See main text for details.

point is placed in the same octant as the radiant in Figure 6.14. Physically this is not possible as the radiant and reflection point cannot occupy the same octant since the equation of the plane of reflection points will not pass through this octant. However this does not affect the generality of the result. Through geometrical arguments we obtain the direction cosines with respect to axes ON, OE, and OZ.

$$l_A = \sin\theta_A \cos\phi_A \tag{6.22}$$

$$m_A = \sin\theta_A \sin\phi_A \tag{6.23}$$

$$n_A = \cos\theta_A \tag{6.24}$$

As mentioned previously the translation of these observer reflection point direction

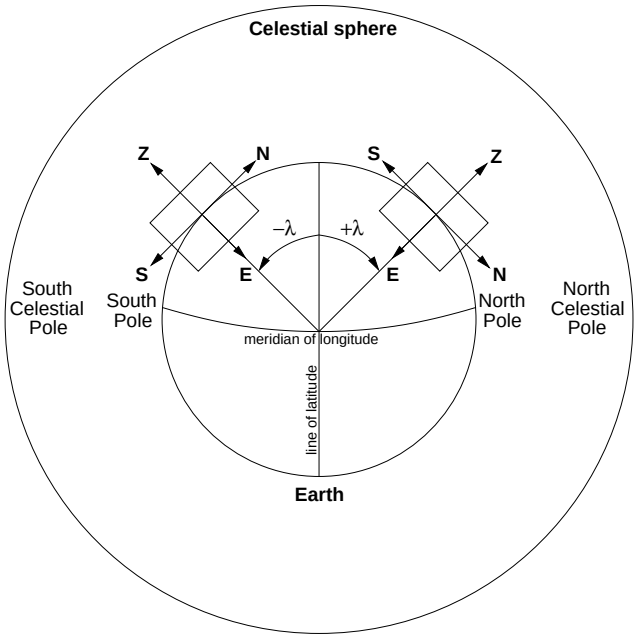

Figure 6.18: Orientation of observations made at latitudes south ($-\lambda$) and north ($+\lambda$) of the equator.

cosines (l_A, m_A, n_A) to their equivalent celestial directions cosines (l_1, m_1, n_1) can be obtained via a rotation of the ON, OE, OZ frame around the EW axis to align with the OP, OE, OT frame. To effect this translation we define the latitude (λ) of the observer's site as positive northward from the terrestrial equator, see Figure 6.18.

Thus the direction cosines of the reflection point in the celestial frame in terms of the direction cosines in the observer's frame are given as [*Elford*, 1954]

$$l_1 = l_A \cos\lambda - n_A \sin\lambda \tag{6.25}$$

$$m_1 = m_A \tag{6.26}$$

$$n_1 = l_A \sin\lambda + n_A \cos\lambda \tag{6.27}$$

Once the radar reflection points have been translated to the celestial frame, a possible radiant may be identified by the fitting of a straight line. Alternatively, if a particular shower is known to be active during data collection, its RA and δ can be plotted. Thus reflection points lying along the line represented by this active shower can be selected as shower meteors. An example of this is detailed in the next chapter.